PHD THESIS

First principles simulations of magnetic nanostructures

László BALOGH

Supervisor: László UDVARDI

Budapest University of Technology and Economics

2015

List of abbrev.

L composite index: $L \equiv (\ell, m)$

Q composite index: $Q \equiv (\kappa, \mu)$

$\sigma_x, \sigma_y, \sigma_z$ Pauli matrices

$\boldsymbol{\sigma}$ vector, composed of the Pauli matrices; $\mathbf{S} = \frac{\hbar}{2}\boldsymbol{\sigma}$ is the spin operator

$\boldsymbol{\sigma}_i$ unit vector parallel to the magnetization of site i

$\hat{\mathbf{v}}$ unit vector: $\hat{\mathbf{v}} = \mathbf{v}/v$

z^* conjugate of the complex number, z

$\mathbf{Z}^{\mathrm{T}}$ transpose of the matrix, $\mathbf{Z}$

$\mathbf{Z}^{\dagger}$ conjugate transpose (adjoint) of the complex matrix, $\mathbf{Z}$

<div align="center">∗   ∗   ∗</div>

AFM   antiferromagnet, antiferromagnetic, see p. 3

ASA   atomic sphere approximation, see eq. (4.26)

CW   cycloidal (domain) wall, see p. 35

DFT   density functional theory

DM   Dzyaloshinsky–Moriya

EC   embedded cluster

FM   ferromagnet, ferromagnetic, see p. 3

HW   helical (domain) wall, see p. 35

KKR   Korringa–Kohn–Rostoker (method)

MC   Monte Carlo (algorithm, simulation, simulated annealing)

MR   magneto-resistance, see p. 34

MST   multiple scattering theory, see p. 19

SBZ   surface Brillouin zone , see p. 22

SKKR   screened KKR

SOC   spin-orbit coupling

SP-STM   spin-polarized scanning tunneling microscopy

SP-STS   spin-polarized scanning tunneling spectroscopy

SPO   scattering path operator, see eq. (4.30)

Contents

Chapter 1

Introduction

Magnetic data storage technology used in hard disk drives has already undergone several milestones from inductive read heads through magnetoresistive, giant magnetoresistive, and tunneling magnetoresistive read heads. Bit cell dimension is around 100 nm (width) $\times$ 18 nm (length) meaning an areal density of about $400 \ \mathrm{Gbit/in^2}$ in 2009. [1] Using longitudinal magnetic recording the superparamagnetic limit has been reached in 2006 at about $200 \ \mathrm{Gbit/in^2}$ areal density and could be overcome by the introduction of the perpendicular magnetic recording extending the superparamagnetic limit up to about $1 \ \mathrm{Tbit/in^2}$ areal density. A promising candidate of new technologies is the heat-assisted magnetic recording (HAMR) which 1 terabit per square inch has been already achieved with. [2]

In 2012 the first spin-torque magnetoresistive RAM (ST-MRAM) has been commercialized. [3] It is able to provide enhancement and to complement flash memory technology together with protection of data in the event of power loss. In magnetoresistive RAMs data is stored as a magnetic state versus an electronic charge. "The ST-MRAM employs a one transistor, one magnetic tunnel junction (MTJ) memory cell for the storage element." [4] Writing is accomplished by driving a spin-polarized current through the MTJ to change the direction of polarization and the data is read by sensing the MTJ resistance.

These technological importances have been motivating the stressed attention to magnetism in reduced symmetry systems. In low-dimensional magnetic systems the nearest neighbor distance, the symmetry and the hybridization with the substrate play a crucial role for the magnetic properties. This may lead to a variety of magnetic structures, from the ferromagnetic and antiferromagnetic states through spin-spirals to more complex non-collinear spin textures. Nanomagnets possess a rich variety of magnetic properties and are expected as constituents of spintronics technologies. Development in sample preparation and experimental technology made it possible to validate the theoretical results, to make new discoveries and to raise further questions.

Among other experimetal methods spin-polarized scanning tunneling microscopy (SP-STM) and spin-polarized scanning tunneling spectroscopy (SP-STS) became now the leading techniques in exploring the fundamentals of magnetic interactions and complex magnetic ordering. [5] SP-STM is able to tailor nanomagnets ranging from linear chains to complex

two-dimensional arrays and to perform magnetometry in an atom-by-atom fashion. [6] A recent review on the effect of the quantum confinement on nanostructures can be found in Ref. 7.

Three basic classes of magnetic modeling are "full electronic description of the magnetic material", 'spin models' and 'micromagnetism'. A brief summary of the classical spin models is given here based on the review of Nowak. [8] Nowadays, large systems cannot be treated on first principles footing without any approximation. The large number of degrees of freedom of the electron system of a solid matter have to be reduced in order to handle the calculation. Rigid spin models can be considered as an extreme reduction of the degrees of freedom and also some neglection of quantum effects. In the framework of a rigid spin model every atom of the system is represented by a classical unit vector, $\boldsymbol{\sigma}_i = \boldsymbol{\mu}_i/\mu_i$, which corresponds to the direction of the spin magnetisation of the atom i, and $\boldsymbol{\mu}_i$ is the atomic spin magnetisation vector. The energy of the system depends only on the spin directions: $\mathcal{H} = \mathcal{H}\left(\{\boldsymbol{\sigma}_i\}\right)$. The realistic lattice structure can be taken into account and para-, ferri-, ferro- or antiferromagnets or even heterostructures can be modeled. The parameters of the model are often derived from or fitted to first principles calculations. In a micromagnetic description the magnetisation density of a solid medium is represented by a continuous function, $\mathbf{m}(\mathbf{r})$. One can think rigid spin models as a discretization of a continuous model, i.e., $\boldsymbol{\mu}_i = \int_{V_i} \mathbf{m}(\mathbf{r}) \, \mathrm{d}^3\mathbf{r}$ where V_i means the domain of the i-th atom. Magnetic particles in the nanometer regime can only be described by first principles or spin model methods since they are too small for a continuous model. Spin models and micromagnetic models can be straightforwardly generalized to the finite temperature equilibrium case. [8]

Often, the energy of the system, $\mathcal{H}$, is given in terms of a spin model, nevertheless, in this thesis (sections 4.5 and 5.1) an attempt is made at circumventing the application of a spin model and applying a Monte Carlo (MC) method to the full electronic description of the magnetic medium.

A widely used model for describing the magnetism of transition metals is the Heisenberg model which takes the following form if relativistic effects (spin-orbit coupling, SOC) are included:

$$\mathcal{H} = \sum_{\langle i,j \rangle} \boldsymbol{\sigma}_i^{\mathrm{T}} \mathbf{J}_{ij} \boldsymbol{\sigma}_j + \sum_i \boldsymbol{\sigma}_i^{\mathrm{T}} \mathbf{K}_i \boldsymbol{\sigma}_i, \tag{1.1}$$

where $\mathcal{H}$ is the energy of the spin system, the first summation runs over the interacting pairs of spins, $\boldsymbol{\sigma}_i$ is a unit vector parallel to the magnetization at site i, $\mathbf{J}_{ij}$ are generalized exchange interaction matrices and $\mathbf{K}_i$ represents the second-order on-site anisotropy matrix. Without loss of generality, the $\mathbf{K}_i$ matrices are chosen to be symmetric and traceless. The $\mathbf{J}_{ij}$ exchange matrices are usually decomposed into an isotropic part of $J_{ij} = \frac{1}{3} \mathrm{Tr}\, \mathbf{J}_{ij}$, a traceless symmetric anisotropic part defined as $\mathbf{J}_{ij}^{\mathrm{S}} = \frac{1}{2}\left(\mathbf{J}_{ij} + \mathbf{J}_{ij}^{\mathrm{T}}\right) - J_{ij}\mathbf{I}$ and an antisymmetric part given by $\mathbf{J}_{ij}^{\mathrm{A}} = \frac{1}{2}\left(\mathbf{J}_{ij} - \mathbf{J}_{ij}^{\mathrm{T}}\right)$. The latter term is usually formulated with the Dzyaloshinsky–Moriya (DM) vector, $\mathbf{D}_{ij}$, as $\boldsymbol{\sigma}_i^{\mathrm{T}} \mathbf{J}_{ij}^{\mathrm{A}} \boldsymbol{\sigma}_j = \mathbf{D}_{ij} \cdot (\boldsymbol{\sigma}_i \times \boldsymbol{\sigma}_j)$. The decomposed model reads:

$$\mathcal{H} = \sum_{\langle i,j \rangle} J_{ij} \left(\boldsymbol{\sigma}_i \cdot \boldsymbol{\sigma}_j\right) + \sum_{\langle i,j \rangle} \boldsymbol{\sigma}_i^{\mathrm{T}} \mathbf{J}_{ij}^{\mathrm{S}} \boldsymbol{\sigma}_j + \sum_{\langle i,j \rangle} \mathbf{D}_{ij} \cdot (\boldsymbol{\sigma}_i \times \boldsymbol{\sigma}_j) + \sum_i \boldsymbol{\sigma}_i^{\mathrm{T}} \mathbf{K}_i \boldsymbol{\sigma}_i. \tag{1.2}$$

This energy function includes magneto-crystalline anisotropy and spin-spin interactions up to second order. Dipole-dipole interaction is neglected in this thesis since in small clusters or in antiferromagnetic systems having zero net magnetisation the dipole-dipole interaction is negligible compared to the other interactions.

The first term in eq. (1.2) is of non-relativistic origin so usually it is the most stressed among the contributions. The Dzyaloshinsky–Moriya term appears in linear order in the spin-orbit parameter, ξ, when a second order perturbation theory is applied for the spin-orbit coupling. Therefore, it can be much larger than the symmetric anisotropic exchange (also called the pseudo-dipolar coupling) or the on-site anisotropy which appears in second order in ξ within the perturbation theory. However inversion symmetry eliminates the anti-symmetric part of the exchange tensor, i.e., the Dzyaloshinsky-Moriya interaction. [9–12] Spin-orbit coupling (SOC) has an important role in the formation of different magnetic states via magnetocrystalline anisotropy and Dzyaloshinsky-Moriya interactions. [13]

For layered systems the coupling constants exhibit translational symmetry and the symmetry of the lattice structure determines the form of the on-site anisotropy. For (001) and (111) surfaces of cubic materials, e.g., the leading on-site term is an uniaxial anisotropy. However, in the case of magnetic clusters the translational symmetry is removed and the parameterization of the on-site anisotropy gets complicated due to the reduced symmetry of the system.

Considering only the isotropic exchange coupling, i.e., discarding the relativistic effects, the following very simple model is derived:

$$\mathcal{H} = \sum_{\langle i,j \rangle} J_{ij} \left(\boldsymbol{\sigma}_i \cdot \boldsymbol{\sigma}_j \right). \tag{1.3}$$

$J_{ij} < 0$ for ferromagnetic (FM) and $J_{ij} > 0$ for antiferromagnetic (AFM) coupling. In both cases the isotropic coupling prefers collinear (parallel or antiparallel) spin alignment without preference of any direction. In the ground state of a ferromagnet all spins points to the same direction and since every bond is in its minimal energy state this is the solution of the model. Here, within this isotropic model the direction of the ferromagnetic alignment is not determined, however.

If the graph of the interacting spins is a bipartite graph (e.g., a square lattice, a simple cubic lattice) an antiferromagnetic system can also be in a state in which every bond is in the minimal energy state, namely, spins in one partition of the system point to the, e.g., $+\hat{\mathbf{z}}$ direction and the spins in the other partition point to the $-\hat{\mathbf{z}}$ direction. In the case of a non-bipartite lattice, e.g., a triangle, a triangular lattice, the energy minimum of each bond cannot be fulfilled simultaneously, and the ground state may become a non-collinear state. This phenomenon is called *geometric frustration*.

The most simple example of frustated systems is the antiferromagnetic equilateral triangle. Writing the energy expression of the AFM triangle ($J > 0$) in the following way,

$$
\begin{aligned}
\mathcal{H} &= J\left(\boldsymbol{\sigma}_1 \cdot \boldsymbol{\sigma}_2 + \boldsymbol{\sigma}_2 \cdot \boldsymbol{\sigma}_3 + \boldsymbol{\sigma}_3 \cdot \boldsymbol{\sigma}_1\right) \\
&= \frac{J}{2}\left[\left(\boldsymbol{\sigma}_1 + \boldsymbol{\sigma}_2 + \boldsymbol{\sigma}_3\right)^2 - \left(\boldsymbol{\sigma}_1\right)^2 - \left(\boldsymbol{\sigma}_2\right)^2 - \left(\boldsymbol{\sigma}_3\right)^2\right] \\
&= \frac{J}{2}\left(\boldsymbol{\sigma}_1 + \boldsymbol{\sigma}_2 + \boldsymbol{\sigma}_3\right)^2 - \frac{3J}{2},
\end{aligned}
\tag{1.4}
$$

it can be read off that the ground state is: $\boldsymbol{\sigma}_1 + \boldsymbol{\sigma}_2 + \boldsymbol{\sigma}_3 = \mathbf{0}$. The spins lie in one plane and enclose 120° with each other. This configuration is called the *120° Néel state*.

Frustration also accours in the AFM triangular lattice, in the FM square lattice with AFM next nearest neighbor coupling or in the FM classical Heisenberg model on Möbius strip [14].

The two type of 120° Néel structures can be distinguished by investigating the chirality of the configurations. According to Antal *et al.* [15] the chirality vector for a trimer is defined as

$$
\boldsymbol{\kappa} = \frac{2}{3\sqrt{3}}\left(\boldsymbol{\sigma}_1 \times \boldsymbol{\sigma}_2 + \boldsymbol{\sigma}_2 \times \boldsymbol{\sigma}_3 + \boldsymbol{\sigma}_3 \times \boldsymbol{\sigma}_1\right),
\tag{1.5}
$$

with the spin numbering in clockwise order around the triangle. Examples of the $\kappa^z = +1$ and the $\kappa^z = -1$ configurations are shown in fig. 1.1.
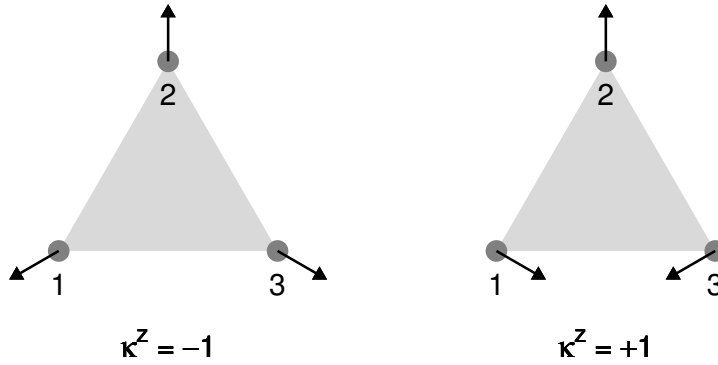
Figure 1.1   Two opposite chirality spin configurations of an equilateral trimer. $\boldsymbol{\sigma}_1 + \boldsymbol{\sigma}_2 + \boldsymbol{\sigma}_3 = \mathbf{0}$ holds and any pair of spins enclose 120° angle. $\boldsymbol{\kappa} = (0;0;-1)$ for the left and $\boldsymbol{\kappa} = (0;0;+1)$ for the right example. A 180° simultaneous rotation of the spin vectors around an axis parallel to the $\boldsymbol{\sigma}_2$ direction transforms one configuration into the other, but, e.g., a simultaneous rotation around the z axis does not change the chirality.

The Néel structure on an entire monolayer is a special case of the general spin spiral magnetic configuration. However, spin structures like row-wise or double-row-wise antiferromagnetic alignments [16], or even a three-dimensional spin structure [17] have been predicted for 2D triangular lattice. Also SP-STM measurements revealed that in the case of some thin films the spin-spiral magnetic configuration has lower energy than the ferromagnetic or anti-ferromagnetic configuration [13] due to the Dzyaloshinsky–Moriya interaction.

After this introductory chapter, an overview of previous experiments and theoretical developments are summarized based on the literature. (Chapter 2) Then, the objective of the work is given in more detail than in this paragraph. (Chapter 3) *Ab initio* calculations on magnetic nanostructures are useful and necessary for the interpretation of experimental results and to attain better understanding of the underlying physical phenomena. In this thesis, the embedded cluster Korringa–Kohn–Rostoker (EC-KKR) electronic structure calculation method is used. The method is outlined in Chapter 4. In Chapter 5, three applications are presented based on the published results. The first example is a 4 atom $\times$ 4 atom size Co cluster deposited on the (001) surface of Cu. A Monte Carlo simulation based on the *ab initio* results is applied to determine the temperature dependent magnetization of the cluster. (Section 5.1) In the second example, the magnetic ground state of an atomic size Co contact between Co leads is determinded. Opposite magnetic boundary conditions are fixed in the leads and no *a priori* spin model for the nano-contact is exploited. (Section 5.2) The third system is a frustrated triangular Cr cluster on the (111) surface of Au and it is investigated in four different positions. A spin model is established and the spin model parameters are determined based on the *ab initio* calculations. (Section 5.3) A short conclusion (Chapter 6) closes the thesis.

Chapter 2

Literature overview

Among the wide variety of nanostructure geometries the *contact-like* and the *island-like* geometries are chosen to be investigated in this thesis. The contact-like geometry consists of two metallic leads and the (usually) atomic size contact between them. Typical realisation of this geometry is the scanning tunneling microscopy (STM) arrangement or the break junction arrangement. These equipments serve for performing the measurements at the same time. In the scope of this thesis, the contact is made of magnetic material and the leads can be magnetic or non-magnetic. In the case of the island-like geometry, some magnetic atoms are placed onto a macroscopic magnetic or non-magnetic metallic substrate. The sample preparation and the experiment are usually carried out separately. Recent developments in nanotechnology permit the construction of these structures in a well controlled way down to the atomic scale and enable the measurement of various properties. In this chapter, an overview of the experimental and theoretical techniques and the results is given.

Jamneala *et al.* [18] found two states of the compact Cr trimer deposited on the Au(111) surface, either of them exhibits a narrow Kondo resonance at the Fermi energy. Probing the Kondo resonance in terms of low-temperature scanning tunneling spectroscopy Heinrich *et al.* [19] determined the spin-flip energy of single Mn atoms. Wahl *et al.* [20] were able to estimate the exchange coupling between deposited Co adatoms. Néel *et al.* [21] studied the transition from the tunneling to the contact regime by moving the STM tip closer to the surface adatom, and an enhanced Kondo temperature was found. Calvo *et al.* [22] found a Fano resonance for ferromagnetic point contacts indicating that the reduced coordination can dramatically effect the magnetic behavior of nanoclusters.

Magnetoresistance has a stressed importance in both applied and basic research. Experiments on atomic-sized contacts of ferromagnetic metals generated by a mechanically controllable break junction revealed magnetoresistance (MR) effects of unprecedented size. [23–25] In particular, based on *ab initio* calculations, the anisotropic MR has been shown to emerge in wire like transition metal nanocontacts and has been related to the giant orbital moment formed at the central atom. [26] Pasupathy *et al.* [27] showed a nice example of controlling the orientation of the magnetic moments in the two electrodes.

The measurements of Calvo *et al.* [22] and Autès *et al.* [26] on ferromagnetic 3d metal nanocontacts motivated the investigations of the magnetic ground state and the magnetic an-

isotropy of a Co point contact between oppositely magnetised ferromagnetic Co leads, see Section 5.2.

In bulk ferromagnets the formation of a magnetic domain wall is governed by a competition between the exchange and anisotropy energies [28] and the typical interface between the magnetic domains is the Bloch wall where the magnetization remains perpendicular to the axis of the wall. In thin films with easy plane anisotropy, a Néel wall is formed with atomic magnetic moments lying in the plane of the film; however, DM interactions can give rise to domain walls with out-of-plane magnetization and well-defined rotational sense. [29, 30] In a geometrically constrained system, e.g., in a nanocontact, the structure of a domain wall is mainly determined by the geometry irrespective of the exchange and anisotropy energies. [31] Thermal effects play an additional role and can lead to new types of domain walls beyond the usual restriction of constant magnetization magnitude. [32]

Development in spin-polarized scanning tunnelling microscopy (SP-STM) made it possible to explore non-collinear magnetic structures in atomic resolution. [13] SP-STS investigations on sub-monolayer Co on Cu(111) surface [33] pointed out that the magnetic adatoms form triangular islands with ferromagnetic ground state where the easy axis was perpendicular to the plane of the substrate. Frustrated non-collinear magnetic structures were reported by Gao *et al.* [34] for Mn islands deposited on Ag(111) surface. Based on topographic measurements which only collect information from the Mn layer and the topmost Ag layer, they concluded that fcc up and hcp down type islands and fcc stacked stripes were present. They demonstrated that the islands exhibit the 120° Néel magnetic structure and the orientation of the Mn moments differs by 30° between fcc and hcp stacked islands most likely due to spin-orbit coupling which is different for the two stackings. The latter phenomenon made it possible to distinguish the islands with different stackings.

The 120° Néel state of Cr mono-layer on Pd(111) substrate was observed by Waśniowska *et al.* [35] by SP-STM measurements. From first-principles calculations on flat spin spirals, they predicted the ground state to be the 120° Néel state which is in agreement with the measurements. Palotás *et al.* [36] demonstrated by first principles calculations that the two possible Néel states with opposite chiralities of a Cr mono-layer on Ag(111) are energetically in-equivalent. They also showed that the magnetic contrast of the simulated SP-STM image was sensitive to the electronic structure of the tip and to the bias voltage.

Accurately describing frustrated magnetic systems both experimentally and theoretically is still a challenge. The most simple system exhibiting geometric frustration is an antiferro-magnetically coupled symmetric trimer. An equilateral compact chromium trimer deposited on the (111) surface of gold is an archetype of such systems. The first non-collinear magnetic calculations of supported metallic 3d triangular trimers were presented fifteen years ago by Uzdin *et al.* [37] Within the vector Anderson model they showed that a supported equilateral Cr trimer exhibited zero net magnetic moment with the atomic moments enclosing 120° angles. Later, *ab initio* calculations [38, 39] agreed that the magnetization at all the sites were laying in the plane enclosing 120° with each other. Gotsits *et al.* [38] performed spin-polarized electronic structure calculation using the projector augmented-wave method with

the spin-orbit coupling (SOC) included. Bergman *et al.* [39] used an extension of the real space linear muffin tin orbital method (RS-LMTO) within the atomic sphere approximation (ASA) with relativistic effects included within the scalar relativistic approximation. Using fully relativistic constrained self-consistent multiple scattering Green's function electronic structure calculations [40] and adiabatic spin dynamics [41] to search for the ground state, Stocks *et al.* [42] also concluded that the ground state of the compact Cr trimer on Au(111) is the 120° Néel state. The energy of the two magnetic configurations with opposite chirality turned out to be different as it has also been confirmed by Antal *et al.* [15] They pointed out that the Dzyaloshinskii–Moriya (DM) interaction is responsible for the lifting of the degeneracy of the states with opposite chirality. Earlier works usually define the chirality at the triangular lattice "as the sign of rotation of the spins along the three sides of each elementary triangle". [43] Nowadays, the chirality of triangular antiferromagnetic clusters is even suggested as a realisation of a qubit. [44]

The measurements of Gao *et al.* [34] and the calculations of Stocks *et al.* [42] and Antal *et al.* [15] motivated the investigations of chirality and anisotropy of Cr trimers of different stacking on the Au(111) surface, see Section 5.3.

Next to the emphasized STM and break junction experimental techniques, a short note is given to present some other important experimental techniques. X-ray magnetic circular dichroism (XMCD) measurements revealed [45] that the magnetic anisotropy energies (MAE) of small Co clusters on Pt(111) surface are an order of magnitude larger than the anisotropy of the ordered CoPt alloy. The magnetic anisotropy is further enhanced in core–shell structures with Pt- and Co cores surrounded by Fe-, Co-, Pt- or Pd shells deposited on Pt(111) surface [46] according to the results of magneto optical Kerr effect (MOKE) experiments. Even magnetic anisotropy of a single Co adatom on MgO surface could be determined by XMCD measurements [6] where the orbital moment retains its free atom value resulting in a huge MAE of 60 meV.

In the following paragraphs, the numerical techniques of the simulation of magnetic systems is overviewed. The density functional theory (DFT) era in numerical calculation of ground state electronic structure started with the work of Hohenberg, Kohn and Sham. [47, 48] Kohn won the Nobel Prize in Chemistry "for his development of the density-functional theory" in 1998. The theory was extended to the relativistic case by Vignale and Rasolt as the current density-functional theory. [49–52]

Several methods to determine complex magnetic ground states of nanoparticles from first principles are based on a fully unconstrained local spin-density approximation (LSDA) implemented within the full-potential linearized augmented plane-wave (FLAPW) method [17] or the projector augmented-wave (PAW) method. [53] Unconstrained non-collinear magnetic calculations are also performed within a tight-binding approach, [54] using the tight-binding linearized muffin-tin orbital (TB-LMTO) method [39, 55] or the Korringa-Kohn-Rostoker (KKR) method. [56, 57] SOC is usually treated as a perturbation or by directly solving the Dirac equation. The latter concept is applied in studies relying on *ab initio* spin dynamics in terms of a constrained LSDA by means of a fully relativistic KKR method. [42, 58, 59]

In this thesis, the Korringa–Kohn–Rostoker (KKR) electronic structure calculation method [60, 61] is used. The KKR method uses Green's function instead of the wave function therefore it is well suitable for investigation of transport properties in metals. [62] One important advantage of the KKR method is that it uses the same formalism both in non-relativistic and in relativistic treatment. In this work, the investigation of anisotropic Heisenberg coupling and magnetocrystalline anisotropy requires the fully relativistic (non-perturbative) description. The KKR method is able to describe disorder (alloys [63] or paramagnetic phase [64]) in metals. Szunyogh *et al.* [65, 66] and Zeller *et al.* [67] applied the KKR method to surfaces (an interface calculation would be the same in formalism) by introducing the screening transformation, i.e., deriving the screened KKR (SKKR) method. Lazarovits *et al.* [68, 69] extended the KKR method with the embedding technique and applied it to finite clusters deposited onto a surface. The KKR Green's function method with the above developments is still a modern electronic structure calculation method, see the recent review of Ebert, Ködderitzsch and Minár. [70]

When describing magnetic structures, i.e., the energy of a spin-configuration, $E\left(\{\boldsymbol{\sigma}_i\}\right)$, relying on the electronic structure calculation we assume that the fast electronic degrees of freedom together with the longitudinal spin fluctuations and the slow transversal spin fluctuations are adiabatically decoupled. [71] Jansen showed [72] that the energy of the different magnetic configurations can be determined by using the band energy within the magnetic force theorem (MFT). To map the energy of the *ab initio* calculation onto a classical Heisenberg spin model the torque method or the method of infinitesimal rotations [73, 74], the rotational energy method [75, 76] and the spin cluster expansion [76–79] can be used.

In Section 4.1 a compact summary of the formalism of the fully relativistic KKR method is given. The extensions which are employed in this thesis are presented in more details in Sections 4.2–4.5.

Chapter 3

Objective of the work

In this work, magnetic nanostructures deposited onto magnetic or non-magnetic substrate are investigated by numerical calculations based on first principles. An effort is made to compare the first principles description to an appropriate spin-model description. In the studied systems SOC plays an important role. Fully relativistic electronic structure calculations are used, therefore, the SOC is taken into account in a non-perturbative way. It is presented how the relativistic effects lift the degeneracy of the non-relativistic ground state.

In nanoclusters compared to higher dimensionality structures the symmetry of the system is lower. Therefore, there are many independent coupling parameters and higher order spin-interactions also play an important role. [15] In the case of a magnetic overlayer the inversion symmetry is also broken which results in a non-vanishing DM coupling. Therefore, *ab initio* calculations on magnetic nano-structures are necessary for a clear interpretation of experimental results.

Among several theoretical tools available for determining electronic structure of magnetic systems, in my thesis the Korringa–Kohn–Rostoker [60, 61] method is applied. The magnetic properties of nanoclusters (cobalt, chromium) deposited onto a magnetic or onto a non-magnetic substrate (cobalt, copper, gold) have been calculated by using embedded cluster Green's function technique [68, 69] as combined with the KKR method. The KKR method extended with the screening technique [65–67] is suitable for the proper description of the semi-infinite magnetic or non-magnetic substrates.

In Sections 5.2 and 5.3, a spin model is constructed corresponding to the symmetry. From the *ab initio* band energy, the spin model parameters are determined by the torque [73, 74] and the rotational energy [75, 76] methods. In Section 5.1, a demonstration is provided that a fully *ab initio* based Monte Calrlo simulation of the magnetic structure of the nanocluster can be performed.

The common origin of the magnetic anisotropy energy (MAE) and the anisotropy of the orbital moment is the SOC. [12] The strong correlation between them is highly confirmed by the numerical investigation of the MAE and the orbital moment of the central atom of a cobalt point contact. (See Section 5.2.)

The classic example of frustration is the antiferromagnetically coupled symmetric trimer where it is impossible to set all the three spin-pairs in their lowest energy state simultaneously.

Compact Cr trimer on the Au(111) surface is a well-studied system, [15, 38, 39, 42] however, in this thesis something new is added to the understanding. There is consensus in the theoretical literature that the ground state is an in-plane 120° Néel state. The Dzyaloshinsky–Moriya interaction and the pseudo-dipolar coupling together determine the chirality of the trimer and the in-plane spin orientation. These two interactions both disappear in a non-relativistic treatment, therefore in a non-relativistic treatment the sense of the chirality is not lifted and the in-plane orientation remain degenerate. The results of this topic are presented in Section 5.3.

Ferromagnetic nanocontact can also show frustrated behaviour with opposing boundary conditions. A Co point contact between oppositely magnetized Co leads is investigated in Section 5.2. It is presented that the MAE of the central atom lifts the classical degeneracy of the domain wall.

3.1 Thesis points

1. I implemented a fully *ab initio* Monte Carlo simulation by extending the KKR code and calculated the temperature dependent magnetization of a 4×4 Co cluster deposited on the Cu(001) surface. The isotropic exchange parameters and an estimation of the uniaxial on-site anisotropy of the Heisenberg model of this system were determined. The spin model MC simulation was compared to the fully *ab initio* MC simulation. I found that the magnetization curves from the two simulations practically agree. The validity of the application of the spin model is confirmed. The unquestionable advantage of the *ab initio* MC approach is the non-requisiteness of an *a priori* spin model and the cost for that is the extreme computational demand.

   Publication II belongs to this thesis point.

2. The magnetic structure of a model of a Co point contact between two oppositely magnetized Co leads has been investigated by means of *ab initio* calculations. The strong ferromagnetic coupling and the symmetry enable two distinct domain walls: helical (HW) and cycloidal wall (CW) and the CW was 30 meV lower in energy. The width of the domain walls followed the length of the point contact under a deformation of $-15\% \ldots +15\%$. Strong uniaxial anisotropy of the central atom was experienced with an easy axis perpendicular to the leads which was the main reason of the lower energy of the CW. Anisotropy of the orbital moment of the central atom was also revealed in strong correlation with the magnetic anisotropy energy.

   Publication III belongs to this thesis point.

3. Equilateral compact Cr trimers deposited onto fcc hollow or hcp hollow positions of the Au(111) surface were investigated. Antiferromagnetic coupling between the Cr atoms results in a ground state of an in-plane 120° Néel state with two possible chirality. The ground state out of the two Néel states was the result of an interplay between the Dzyaloshinsky–Moriya (DM) interaction and the symmetric part of the two-site anisotropy. The DM interaction depended intriguingly on the geometry. In the case of a Cr

monolayer on the Au(111) surface the non-vanishing z component of the DM coupling results in an energy difference between the Néel structures with opposite chirality.

Publications I and **IV** belong to this thesis point.

3.2 Publications linked to the thesis points

The publications are listed in chronological order. In the Bibliography, see them as References 80, 81, 82 and 83, respectively.

[I] Antal, A., Lazarovits, B., Balogh, L., Udvardi, L. & Szunyogh, L. Multiscale studies of complex magnetism of nanostructures based on first principles. *Philosophical Magazine* **88**, 2715–2724 (2008).
DOI: 10.1080/14786430802389213.

[II] Balogh, L., Lebecki, K. M., Lazarovits, B., Udvardi, L., Szunyogh, L., & Nowak, U. Monte Carlo study on magnetic nanoparticles from first principle. *Journal of Physics: Conference Series* **200**, 072103 (2010). DOI: 10.1088/1742-6596/200/7/072103.

[III] Balogh, L., Palotás, K., Udvardi, L., Szunyogh, L. & Nowak, U. Theoretical study of magnetic domain walls through a cobalt nanocontact. *Phys. Rev. B* **86**,024406 (2012).
DOI: 10.1103/PhysRevB.86.024406.

[IV] Balogh, L., Udvardi, L. & Szunyogh, L. Magnetic anisotropy and chirality of frustrated Cr nanostructures on Au(111). *Journal of Physics: Condensed Matter* **26**, 436001 (2014). DOI: 10.1088/0953-8984/26/43/436001.

Chapter 4

Methods

4.1 Review of the Korringa–Kohn–Rostoker (KKR) electronic structure calculation method

Physical properties of quantum systems are strongly determined by symmetries. In crystals, the two symmetries are the symmetry of the lattice and the spherical symmetry of the potential in the close vicinity of the nuclei. The KKR method manages both by dividing the space into atomic spheres and the intersticial region. In this section, I try to give a review of the KKR method compactly but containing everything that we need in the further parts of this thesis. Among many variants of the KKR method, see Chapter 16 of Ref. 84, here the relativistic spin-polarized version will be outlined in terms of the atomic sphere approximation.

This section is based on two books: Refs. 85 and 84 and three theses: Refs. 69, 62 and 64. Subsequent citations to these references are omitted in this section.

The density functional theory (DFT) provides the procedure to describe a many electron system with a one-electron effective Hamiltonian self-consistently in terms of the charge and the magnetisation density. The DFT is not disscussed here; this section starts with the Kohn–Sham–Dirac-equation and presents the procedure how to solve it for the muffin tin potential construction. The treatment arrives at the fundamental equation of the multiple scattering theory (MST). In the subsequent sections of this chapter, formulas will be derived in order to calculate the energy of different magnetic configurations and the exchange coupling parameters between the magnetic moments.

4.1.1 Kohn–Sham–Dirac equation

The Kohn–Sham–Dirac Hamiltonian is:

$$\left(W - c\boldsymbol{\alpha} \cdot \mathbf{p} - \beta mc^2\right)\psi(\mathbf{r}) = U(\mathbf{r})\psi(\mathbf{r}), \tag{4.1}$$

where c is the speed of light, m is the electron rest mass, $\boldsymbol{\alpha}$ and β are the Dirac matrices (for the definitions see Appendix A), $\mathbf{p} = -i\hbar\boldsymbol{\nabla}$ is the momentum operator, W is the relativistic

energy eigenvalue, $U(\mathbf{r})$ is the effective potential and field as follows:

$$U(\mathbf{r}) = V_{\text{ext}}(\mathbf{r}) + \frac{e^2}{4\pi\varepsilon_0} \int \frac{n(\mathbf{r}')}{|\mathbf{r} - \mathbf{r}'|} \, \mathrm{d}^3\mathbf{r}' + V_{\text{xc}}(\mathbf{r}) + \frac{e\mu_0}{2m}\boldsymbol{\Sigma} \cdot (\mathbf{B}_{\text{ext}}(\mathbf{r}) + \mathbf{B}_{\text{xc}}(\mathbf{r})), \quad (4.2)$$

and $\psi(\mathbf{r})$ is the four component wave function. Eq. (4.1) should be solved self-consistently in terms of the charge and the magnetisation densities. The exchange–correlation potential and field are given as

$$V_{\text{xc}}(\mathbf{r}) = \frac{\delta E_{\text{xc}}}{\delta n(\mathbf{r})} \qquad \text{and} \qquad \mu_0\mathbf{B}_{\text{xc}}(\mathbf{r}) = \frac{\delta E_{\text{xc}}}{\delta \mathbf{S}(\mathbf{r})} \qquad (4.3)$$

with $n(\mathbf{r}) = \psi(\mathbf{r})^\dagger\psi(\mathbf{r})$ the electron density and $\mathbf{S}(\mathbf{r}) = \frac{1}{2}\psi(\mathbf{r})^\dagger\beta\boldsymbol{\Sigma}\psi(\mathbf{r})$ the spin density. The exchange–correlation potential and field were treated within the local spin-density approximation (LSDA), [86, 87] of the density functional theory as parametrized by Perdew and Zunger [88].

In some further formulas in the energy argument, p or ε is used instead of W:

$$p = \frac{1}{c}\sqrt{W^2 - m^2c^4} \quad \text{with} \quad \text{Im}\,p > 0 \qquad \text{and} \qquad \varepsilon = W - mc^2. \qquad (4.4)$$

4.1.2 Free particle Green's function

The solution of the Dirac Hamiltonian is sought in the following combination of bi-spinors:

$$\psi(\mathbf{r}) = \sum_{\kappa\mu} \begin{pmatrix} g_{\kappa\mu}(r)\chi_{\kappa\mu}(\hat{\mathbf{r}}) \\ \mathrm{i}f_{\kappa\mu}(r)\chi_{-\kappa\mu}(\hat{\mathbf{r}}) \end{pmatrix} = \sum_{Q} \begin{pmatrix} g_Q(r)\chi_Q(\hat{\mathbf{r}}) \\ \mathrm{i}f_Q(r)\chi_{\bar{Q}}(\hat{\mathbf{r}}) \end{pmatrix} \qquad (4.5)$$

where $g_{\kappa\mu}(r)$ and $f_{\kappa\mu}(r)$ are the radial functions and $\chi_{\kappa\mu}(\hat{\mathbf{r}})$ are the spin spherical harmonics. The $\chi_{\kappa\mu}$-s are common eigenfunctions of the total angular momentum operator, $\mathbf{J} = \mathbf{L} + \mathbf{S}$, its projection, J^z, and the $K = \mathbf{L} \cdot \boldsymbol{\sigma} + \hbar$ operator. A short summary of the $\kappa\mu$-representation is given in Appendix A.

Let us rewrite the $\boldsymbol{\nabla} = \hat{\mathbf{r}}(\hat{\mathbf{r}} \cdot \boldsymbol{\nabla}) - \hat{\mathbf{r}} \times (\hat{\mathbf{r}} \times \boldsymbol{\nabla}) = \hat{\mathbf{r}}\frac{\partial}{\partial r} - \frac{\hat{\mathbf{r}}}{r} \times (\mathbf{r} \times \boldsymbol{\nabla})$ vector calculus identity into the terms of the momentum, $\mathbf{p} = -\mathrm{i}\hbar\boldsymbol{\nabla}$, and the angular momentum, $\mathbf{L} = \mathbf{r} \times \mathbf{p}$, operators:

$$\mathbf{p} = -\mathrm{i}\hbar\hat{\mathbf{r}}\frac{\partial}{\partial r} - \frac{\hat{\mathbf{r}}}{r} \times \mathbf{L}. \qquad (4.6)$$

Using the definition of σ_r, see eq. (A.5), the identity (A.7) and the definition of the K operator, see eq. (A.19), one gets the kinetic energy operator in polar form:

$$c\boldsymbol{\alpha} \cdot \mathbf{p} = \begin{pmatrix} \mathbf{0} & -\mathrm{i}c\hbar\sigma_r\left(\frac{\partial}{\partial r} - \frac{1}{\hbar r}K + \frac{1}{r}\right) \\ -\mathrm{i}c\hbar\sigma_r\left(\frac{\partial}{\partial r} - \frac{1}{\hbar r}K + \frac{1}{r}\right) & \mathbf{0} \end{pmatrix}. \qquad (4.7)$$

First, we will solve the homogeneous part of eq. (4.1) in order to gain the free particle solution of the Kohn–Sham–Dirac-equation. It has to be exploited that the $\chi_Q(\hat{\mathbf{r}})$ spin spherical harmonics are eigenfunctions of the K operator with eigenvalue of $-\hbar\kappa$ and that $\sigma_r\chi_Q(\hat{\mathbf{r}}) = -\chi_{\bar{Q}}(\hat{\mathbf{r}})$, see eq. (A.25). Considering, that $U(\mathbf{r}) = 0$ in the free space case,

writing back the kinetic energy in polar form, eq. (4.7), into eq. (4.1) and exploiting the bi-spinor form of the wave funtion, eq. (4.5), one can derive the following coupled first order differential equations for the radial functions:

$$
\begin{pmatrix} W - mc^2 & \mathrm{i}c\hbar \left(\frac{\partial}{\partial r} - \frac{\kappa}{r} + \frac{1}{r} \right) \\ \mathrm{i}c\hbar \left(\frac{\partial}{\partial r} + \frac{\kappa}{r} + \frac{1}{r} \right) & W + mc^2 \end{pmatrix} \begin{pmatrix} g_{\kappa\mu}(r) \\ \mathrm{i}f_{\kappa\mu}(r) \end{pmatrix} = 0 \qquad \text{for every } (\kappa, \mu). \quad (4.8)
$$

The following second order differential equation can be derived for, e.g., $g_{\kappa\mu}(r)$ if one makes use of the relation $W^2 = p^2 c^2 + m^2 c^4$ and of $\kappa^2 + \kappa = \ell(\ell+1)$:

$$
\left(\frac{p^2}{\hbar^2} + \frac{\partial^2}{\partial r^2} + \frac{2}{r} \frac{\partial}{\partial r} - \frac{\ell(\ell+1)}{r^2} \right) g_{\kappa\mu}(r) = 0 \qquad (4.9)
$$

The linearly independent solutions of this equation are the

$$
j_\ell \left(\frac{pr}{\hbar} \right), \quad y_\ell \left(\frac{pr}{\hbar} \right); \qquad \text{or the} \qquad h_\ell^\pm \left(\frac{pr}{\hbar} \right) = j_\ell \left(\frac{pr}{\hbar} \right) \pm \mathrm{i}y_\ell \left(\frac{pr}{\hbar} \right) \qquad (4.10)
$$

spherical Bessel functions.

In summary, the solution of the free space Kohn–Sham–Dirac equation is:

$$
\psi^{\text{free space}}(\mathbf{r}) = \sum_Q \psi_Q^{\text{free space}}(\mathbf{r}) = \sum_Q \begin{pmatrix} h_\ell \left(\frac{pr}{\hbar} \right) \chi_Q(\hat{\mathbf{r}}) \\ \frac{\kappa}{|\kappa|} \frac{\mathrm{i}pc\hbar}{W+mc^2} h_{\bar{\ell}} \left(\frac{pr}{\hbar} \right) \chi_{\bar{Q}}(\hat{\mathbf{r}}) \end{pmatrix} \qquad (4.11)
$$

with $\bar{\ell} = \ell - \frac{\kappa}{|\kappa|}$ and the function h_ℓ can be either j_ℓ, y_ℓ or $h_\ell^\pm$ spherical Bessel-, Neumann- or Hankel-functions. Note, that in the numerical calculations the above and all the subsequent summations over Q are truncated at $\ell_{\max} = 2$ in this thesis, see table A.1 in Appendix A.

Here, the functions

$$
J_Q(\mathbf{r}) \qquad \text{and} \qquad H_Q^+(\mathbf{r}) \qquad (4.12)
$$

are introduced, which are $\psi_Q^{\text{free space}}(\mathbf{r})$ but the $j_\ell \left(\frac{pr}{\hbar} \right)$ and the $h_\ell^+ \left(\frac{pr}{\hbar} \right)$ spherical Bessel functions appear in place of h_ℓ, respectively. Note the $J_Q(\mathbf{r})$ and the $H_Q^+(\mathbf{r})$ functions are four component wave functions and they are solutions of the free space Dirac Hamiltonian.

The Green's function of the free particle case is defined as:

$$
\left(W - c\boldsymbol{\alpha} \cdot \mathbf{p} - \beta mc^2 \right) G_0(W; \mathbf{r}, \mathbf{r}') = \delta(\mathbf{r} - \mathbf{r}') \mathbb{1}_{4\times4}, \qquad (4.13)
$$

where we explicitly wrote the 4 by 4 unit matrix, $\mathbb{1}_{4\times4}$, on the right hand side emphasizing that the Green's function, $G_0(W; \mathbf{r}, \mathbf{r}')$, is a 4 by 4 matrix. In the following we omit the energy dependence of the Green's function and of the derived quantities. The free particle Green's function can be easily given as

$$
G_0(\mathbf{r}, \mathbf{r}') = \frac{1}{2mc^2} \left(W + \beta mc^2 + c\boldsymbol{\alpha} \cdot \mathbf{p} \right) \underbrace{\frac{-\mathrm{e}^{\mathrm{i}p|\mathbf{r}-\mathbf{r}'|}}{4\pi |\mathbf{r} - \mathbf{r}'|}}_{G_0^{\text{non-rel.}}(\mathbf{r}, \mathbf{r}')} \mathbb{1}_{4\times4}. \qquad (4.14)
$$

Note that the non-relativistic Green's function, $G_0^{\text{non-rel.}}(\mathbf{r}, \mathbf{r}')$, appears in the expression of the relativistic Green's function. This result follows since

$$\left(\boldsymbol{\nabla}^2 + p^2\right) \frac{-\mathrm{e}^{\mathrm{i}p|\mathbf{r}-\mathbf{r}'|}}{|\mathbf{r}-\mathbf{r}'|} = 4\pi\delta(\mathbf{r}-\mathbf{r}') \tag{4.15}$$

and one can start the evaluation of the Green's function with the expansion

$$\frac{-\mathrm{e}^{\mathrm{i}p|\mathbf{r}-\mathbf{r}'|}}{4\pi|\mathbf{r}-\mathbf{r}'|} = -\mathrm{i}p\sum_L h_\ell^+(pr_>)j_\ell(pr_<)Y_{\ell m}(\hat{\mathbf{r}})Y_{\ell m}(\hat{\mathbf{r}}')^* \tag{4.16}$$

with $r_< \equiv \min(r, r')$ and $r_> \equiv \max(r, r')$. Evaluating eq. (4.14) one arrives at the Green's function of the free Dirac Hamiltonian:

$$G_0(\mathbf{r}, \mathbf{r}') = -\mathrm{i}p\frac{W + mc^2}{2mc^2}\sum_Q H_Q^+(\mathbf{r}_>)J_Q(\mathbf{r}_<)^\dagger \tag{4.17}$$

where $\mathbf{r}_>$ and $\mathbf{r}_<$ mean the longer and the shorter vector out of $\mathbf{r}$ and $\mathbf{r}'$. The H_Q^+ and the J_Q functions are two linearly independent solutions of the free Dirac equation as introduced in eqs. (4.11) and (4.12). Note that the product of the four component column and row vectors, H_Q^+ and $J_Q{}^\dagger$, produces a four by four matrix.

4.1.3 The Lippmann–Schwinger equation

In this section the solution of the inhomogeneous Dirac equation will be solved and the transition operator will be introduced in the meanwhile.

Consider $\psi_0(\mathbf{r})$ as the soulution of the free particle part of the (4.1) Dirac equation with eigenvalue W:

$$(W - H_0)\psi_0(\mathbf{r}) = 0. \tag{4.18}$$

The inhomogeneous equation is

$$(W - H_0)\psi(\mathbf{r}) = U(\mathbf{r})\psi(\mathbf{r}) \tag{4.19}$$

and we look for the solution in the $\psi(\mathbf{r}) = \psi_0(\mathbf{r}) + \delta\psi(\mathbf{r})$ form. Putting this form into eq. (4.19) and exploiting eq. (4.18) one gets:

$$(W - H_0)\delta\psi(\mathbf{r}) = U(\mathbf{r})\psi(\mathbf{r}). \tag{4.20}$$

Using the definition of the Green's function, eq. (4.13), of the homogeneous equation the solution $\psi(\mathbf{r}) = \psi_0(\mathbf{r}) + \delta\psi(\mathbf{r})$ can be given as the following implicit equation:

$$\delta\psi(\mathbf{r}) = \int G_0(\mathbf{r}, \mathbf{r}')U(\mathbf{r}')\psi(\mathbf{r}')\,\mathrm{d}^3\mathbf{r}'. \tag{4.21}$$

From this, the solution of the inhomogeneous equation can be found by successive approximation:

$$\delta\psi(\mathbf{r}) = \int G_0(\mathbf{r},\mathbf{r}')U(\mathbf{r}')\Big(\psi_0(\mathbf{r}') + \int G_0(\mathbf{r}',\mathbf{r}'')U(\mathbf{r}'')\big(\psi_0(\mathbf{r}'') + \dots\big)\,\mathrm{d}^3\mathbf{r}''\Big)\,\mathrm{d}^3\mathbf{r}'. \tag{4.22}$$

Introducing the *transition operator:*

$$T(\mathbf{r}',\mathbf{r}'') = U(\mathbf{r}')\delta(\mathbf{r}'-\mathbf{r}'') + U(\mathbf{r}')G_0(\mathbf{r}',\mathbf{r}'')U(\mathbf{r}'')$$
$$+ \int U(\mathbf{r}')G_0(\mathbf{r}',\mathbf{r}''')U(\mathbf{r}''')G_0(\mathbf{r}''',\mathbf{r}'')U(\mathbf{r}'')\,\mathrm{d}^3\mathbf{r}''' + \dots \tag{4.23}$$

the solution of eq. (4.19) is:

$$\psi(\mathbf{r}) = \psi_0(\mathbf{r}) + \iint G_0(\mathbf{r},\mathbf{r}')T(\mathbf{r}',\mathbf{r}'')\psi_0(\mathbf{r}'')\,\mathrm{d}^3\mathbf{r}''\,\mathrm{d}^3\mathbf{r}' \tag{4.24}$$

which is the Lippmann–Schwinger equation in coordinate representation.

Note that the above thought does not require the Hamiltonian to be partitioned into the free particle part plus the potential but arbitrary partitioning, $H = H_0 + U$, can be used.

4.1.4 The muffin-tin potential construction

In order to exploit the crystal structure including discrete translational symmetry and the point group symmetry, the *multiple scattering theory* (MST) considers the following potential:

$$V(\mathbf{r}) = \sum_{n=1}^{N} V_n(\mathbf{r} - \mathbf{R}_n) \tag{4.25}$$

where $\{\mathbf{R}_n\}_{n=1}^{N}$ is the set of the lattice vectors and V_n is the atomic potential centered at site n. In the *atomic sphere approximation* (ASA) the atomic potential is considered spherically symmetric and confined in the atomic sphere:

$$V_n(\mathbf{r}_n) = \begin{cases} V_n(r_n) & \text{if } r_n \leq S_n, \\ 0 & \text{otherwise,} \end{cases} \tag{4.26}$$

where $\mathbf{r}_n = \mathbf{r} - \mathbf{R}_n$ and S_n is the radius of the atomic sphere around the site n.

The transition operator corresponding to site n is the *single site t-operator:*

$$t^n = V_n + V_n G_0 V_n + V_n G_0 V_n G_0 V_n + \dots. \tag{4.27}$$

The matrix elements of the single site transition operator are introduced:

$$t_{QQ'}^n = \iint J_Q(\mathbf{r})^\dagger t^n(\mathbf{r},\mathbf{r}') J_{Q'}(\mathbf{r}')\,\mathrm{d}^3\mathbf{r}\,\mathrm{d}^3\mathbf{r}' \tag{4.28}$$

and note that the integrals are performed inside the n-th atomic sphere because of the muffin-tin potential construction, eq. (4.26).

The T-operator of the whole system can be expressed with the sum of the single site t-operators as follows:

$$T = \sum_n t^n + \sum_{nm}(1 - \delta_{nm})t^n G_0 t^m + \sum_{n,m,k}(1 - \delta_{nm})(1 - \delta_{mk})t^n G_0 t^m G_0 t^k + \dots \quad (4.29)$$

The *scattering path operator* (SPO) is defined as:

$$\tau^{nm} = t^n \delta_{nm} + (1 - \delta_{nm})t^n G_0 t^m + \sum_k (1 - \delta_{nm})(1 - \delta_{mk})t^n G_0 t^m G_0 t^k + \dots . \quad (4.30)$$

For the further derivation of the *fundamental equation of the MST*, eq. (4.42), the following Dyson-equation should be noted:

$$\tau^{nm} = t^n \delta_{nm} + \sum_k t^n G_0 (1 - \delta_{km})\tau^{km} \quad (4.31)$$

and the matrix elements of the SPO are:

$$\tau^{nm}_{QQ'} = \int\limits_{r_n \leq S_n} \int\limits_{r_m \leq S_m} J_Q(\mathbf{r}_n)^\dagger \tau^{nm}(\mathbf{r}_n, \mathbf{r}_m) J_{Q'}(\mathbf{r}_m)\, \mathrm{d}^3\mathbf{r}_n\, \mathrm{d}^3\mathbf{r}_m. \quad (4.32)$$

4.1.5 Two-center expansion of the Green's function

In order to form the matrix elements of the Green's function with site and angular momentum indices the so-called *two-center expansion* is introduced. Let the two coordinate arguments of the free Green's function, eq. (4.17), be $\mathbf{r} = \mathbf{r}_n + \mathbf{R}_n$ and $\mathbf{r}' = \mathbf{r}_m + \mathbf{R}_m$ such that $r_n \leq S_n$ and $r_m \leq S_m$. The free particle Green's function only depends on the difference between its coordinate arguments:

$$G_0(\mathbf{r}_n + \mathbf{R}_n, \mathbf{r}_m + \mathbf{R}_m) = G_0(\mathbf{r}_n - \mathbf{r}_m, \mathbf{R}_{nm}) \quad (4.33)$$

where $\mathbf{R}_{nm} = \mathbf{R}_m - \mathbf{R}_n$ compact notation is introduced. If the muffin tin spheres do not overlap then $|\mathbf{r}_n - \mathbf{r}_m| \leq R_{nm}$ holds. Therefore

$$G_0(\mathbf{r}_n + \mathbf{R}_n, \mathbf{r}_m + \mathbf{R}_m) = -\mathrm{i}p \frac{W + mc^2}{2mc^2} \sum_Q H_Q^+(\mathbf{R}_{nm}) J_Q(\mathbf{r}_n - \mathbf{r}_m)^\dagger. \quad (4.34)$$

Two identities: expansion of plane waves into spherical Bessel functions (Bauer's identity) and the integral representation of the spherical Bessel functions:

$$\mathrm{e}^{\mathrm{i}\mathbf{k}(\mathbf{r}_n - \mathbf{r}_m)} = (4\pi)^2 \sum_{L'L''} \left(\mathrm{i}^{\ell'-\ell''} j_{\ell'}(kr_n) Y_{L'}(\hat{\mathbf{r}}_n) j_{\ell''}(kr_m) Y_{L''}(\hat{\mathbf{r}}_m)^* Y_{L'}(\hat{\mathbf{k}})^* Y_{L''}(\hat{\mathbf{k}}) \right)$$
$$(4.35)$$

and

$$j_\ell(kr)Y_L(\hat{\mathbf{r}})^* = \frac{\mathrm{i}^{-\ell}}{4\pi}\int \mathrm{e}^{\mathrm{i}\mathbf{k}\mathbf{r}}Y_L(\hat{\mathbf{k}})^*\,\mathrm{d}^2\hat{\mathbf{k}}. \tag{4.36}$$

Combining eqs. (4.35) and (4.36):

$$j_\ell(kr_{mn})Y_L(\hat{\mathbf{r}}_{mn})^*$$

$$= 4\pi\sum_{L'L''}\left(\mathrm{i}^{\ell'-\ell''-\ell}j_{\ell'}(kr_n)Y_{L'}(\hat{\mathbf{r}}_n)j_{\ell''}(kr_m)Y_{L''}(\hat{\mathbf{r}}_m)^*\underbrace{\int Y_{L'}(\hat{\mathbf{k}})^*Y_{L''}(\hat{\mathbf{k}})Y_L(\hat{\mathbf{k}})^*\,\mathrm{d}^2\hat{\mathbf{k}}}_{C_{LL'}^{L''},\ \text{Gaunt coefficients}}\right)$$

$$\tag{4.37}$$

where the $\mathbf{r}_{mn} = \mathbf{r}_n - \mathbf{r}_m$ compact notation is used.

With these formulas the two-center expansion of the relativistic free Green's function for $n \neq m$ can be derived:

$$G_0(\mathbf{r}_n + \mathbf{R}_n, \mathbf{r}_m + \mathbf{R}_m) = \sum_{QQ'} J_Q(\mathbf{r}_n)\big[G_0\big]_{QQ'}^{nm}J_{Q'}(\mathbf{r}_m)^\dagger. \tag{4.38}$$

The relativistic and the non-relativistic structure constants, $\big[G_0\big]_{QQ'}^{nm}$ and $\big[G_0^{\text{non-rel.}}\big]_{LL'}^{nm}$, are related to each other as:

$$\big[G_0\big]_{QQ'}^{nm} = \frac{W + mc^2}{2mc^2}\sum_{s=\pm\frac{1}{2}} C(\ell,\tfrac{1}{2},j;\mu-s,s,\mu)\big[G_0^{\text{non-rel.}}\big]_{\ell,\mu-s;\ell',\mu'-s}^{nm}C(\ell',\tfrac{1}{2},j';\mu'-s,s,\mu')$$

$$\tag{4.39}$$

and the non-relativistic structure contants are:

$$\big[G_0^{\text{non-rel.}}\big]_{LL'}^{nm} = -4\pi p\mathrm{i}\sum_{L''}C_{L'L''}^L\mathrm{i}^{\ell-\ell'-\ell''}h_{\ell''}^+\left(\frac{pR_{nm}}{\hbar}\right)Y_{L''}(\hat{\mathbf{R}}_{nm}). \tag{4.40}$$

Using the matrix elements of the transition operator and the SPO, eqs. (4.28), (4.32), and the two-center expansion of the free Green's function, eq. (4.38), the Dyson equation for the SPO, eq. (4.31), is compactly written in matrix form as

$$\boldsymbol{\tau} = \mathbf{t} + \mathbf{t}\mathbf{G}_0\boldsymbol{\tau} \tag{4.41}$$

or equivalently

$$\boldsymbol{\tau} = \left(\mathbf{t}^{-1} - \mathbf{G}_0\right)^{-1}. \tag{4.42}$$

This is the *fundamental equation of the MST* or the *KKR-equation*. The $\boldsymbol{\tau}$, $\mathbf{t}$ and the $\mathbf{G}_0$ supermatrices have site (n, m) and angular momentum (Q, Q') indices:

$$\mathbf{t} \equiv t_{QQ'}^n\delta_{nm}, \qquad \boldsymbol{\tau} \equiv \tau_{QQ'}^{nm}, \qquad \mathbf{G}_0 \equiv \big[G_0\big]_{QQ'}^{nm}(1 - \delta_{nm}). \tag{4.43}$$

Note that the structure constants, eq. (4.39), only depend on the geometric structure of the lattice via $\mathbf{R}_{nm}$, and the transition matrix, eq. (4.28), only depends on the scatterer potentials. This separation is the basis of the *embedding cluster* technique.

4.1.6 Two-dimensional translational symmetry

We now consider a *layered system* in which the layers and the sites inside one particular layer are indexed separately. Therefore a position vector inside the i-th atomic sphere of the p-th layer can be given as

$$\mathbf{r} = \mathbf{r}_n + \mathbf{R}_n = \mathbf{r}_{pi} + \mathbf{R}_p^\perp + \mathbf{R}_i^\parallel \qquad (4.44)$$

where $\mathbf{r}_n + \mathbf{R}_n$ is our partitioning until now, $\mathbf{R}_p^\perp$ is the origin of the p-th layer, $\mathbf{R}_i^\parallel$ is the position of the i-th site inside this layer and $\mathbf{r}_{pi}$ is a position vector inside the (p, i) site of the lattice. Every layers are composed of identical atoms or, in other words, discrete translational symmetry is preserved inside the layers and is broken in the out-of-plane direction. Different atoms in the unit cell are considered as different layers in this context. *Unit cell* may refer to chemical unit cell or magnetic unit cell as well. Site-indexed quantites now have layer and in-plane site indices:

$$\boldsymbol{\tau}^{nm} = \boldsymbol{\tau}^{pi,qj}, \qquad \mathbf{t}^n = \mathbf{t}^p, \qquad \mathbf{G}_0^{nm} = \mathbf{G}_0^{pi,qj}. \qquad (4.45)$$

The above quantities are still matrices in angular-momentum indices, (Q, Q'), and the single site t-matrix only depends on the layer index.

The in-plane translational invariance is exploited by using the in-plane lattice Fourier transformation:

$$\mathbf{G}_0^{pq}(\mathbf{k}^\parallel) = \sum_{\mathbf{R}_j^\parallel} \mathbf{G}_0^{p0,qj} e^{i\mathbf{k}^\parallel \mathbf{R}_j^\parallel} \qquad \text{and} \qquad \boldsymbol{\tau}^{pq}(\mathbf{k}^\parallel) = \sum_{\mathbf{R}_j^\parallel} \boldsymbol{\tau}^{p0,qj} e^{i\mathbf{k}^\parallel \mathbf{R}_j^\parallel} \qquad (4.46)$$

The fundametal equation of the MST holds in the in-plane Fourier space as:

$$\boldsymbol{\tau}(\mathbf{k}^\parallel) = \left(\mathbf{t}^{-1} - \mathbf{G}_0(\mathbf{k}^\parallel)\right)^{-1}. \qquad (4.47)$$

where the quantites are matrices in layer, (p, q), and in angular momentum indices, (Q, Q'), and the in-plane wave vector, $\mathbf{k}^\parallel$, lies in the first Brillouin zone of the in-plane lattice, i.e., in the first surface Brillouin zone (SBZ).

The backwards transformation from the reciprocal space into the real space is given for the SPO:

$$\boldsymbol{\tau}^{pi,qj} = \frac{1}{\Omega_{\mathrm{SBZ}}} \int\limits_{\mathrm{SBZ}} \boldsymbol{\tau}^{pq}(\mathbf{k}^\parallel) e^{-i\mathbf{k}^\parallel \left(\mathbf{R}_i^\parallel - \mathbf{R}_j^\parallel\right)} \, d^2\mathbf{k}^\parallel \qquad (4.48)$$

where the integration is performed in the first SBZ and Ω_{SBZ} is the area of the SBZ. In this step, the symmetry of the 2D lattice is usually utilized, namely, the $\mathbf{k}^\parallel$-dependent SPO is only computed in one irreducible wedge of the SBZ (IBZ). In other parts of the SBZ, the transfor-

mation of the SPO from the IBZ is used instead of the time-consuming matrix inversion in eq. (4.47).

4.1.7 Screening transformation

The model of a real layered system is composed of a semi-infinite left region plus a finite interface region plus a semi-infinite right region. The layers in one semi-infinite component are identical. In a surface calculation, the right region is vacuum; and also bulk calculation can be performed within this design by choosing all these three regions to be composed of the same material. Note the the 2D lattice in each layer must be the same, however, varying the layer–layer distance and/or in-plane shifting are allowed in the interface region.

In practice, *principal layers* are introduced in which treatment multiple physical layers are held together into one logical layer. This is performed with two motivations:

(*i*) by applying the screening transformation, the structure constants become short-ranged and by choosing the principal layer suitably, and by neglecting interactions beyond adjacent principal layers, the SPO become block-tridiagonal which is a computational gain contrary to a full matrix [65]; and

(*ii*) in an interface calculation, the *surface SPO* can be calculated by the removal invariance of the semi-infinite surface.

4.1.8 Embedded cluster (EC) Green's function technique

Consider a *host* system composed of the muffin-tin potentials, $V_{\text{host}}^n(r_n)$, for which the single site t-matrices, $\mathbf{t}_{\text{host}}^n$, are known and the SPO is calculated as

$$\boldsymbol{\tau}_{\text{host}} = \left(\mathbf{t}_{\text{host}}^{-1} - \mathbf{G}_0\right)^{-1}, \tag{4.49}$$

where $\mathbf{G}_0$ is the stucture constant of the host lattice.

Let $\mathcal{C}$ be a set of site indices (a cluster) for which the scatterers are changed from the host potential to some *impurity* potential. The potential of this system is given by:

$$V_n(\mathbf{r}_n) = \begin{cases} V_{\text{imp}}^n(r_n) & \text{if } n \in \mathcal{C} \\ V_{\text{host}}^n(r_n) & \text{if } n \notin \mathcal{C}. \end{cases} \tag{4.50}$$

Ad-atoms on a surface are comprised in this model: the host system should be composed of a semi-infinite substrate and a semi-infinite vacuum region with some substrate and vacuum buffer layers held into an interface region and then the appropriate vacuum spheres in the first vacuum layer should be replaced by the ad-atom potentials. Note, that no further geometrical relaxation is considered here, namely, the substituting impurities must be placed in the host lattice sites. The SPO of this impured system is $\boldsymbol{\tau} = (\mathbf{t}^{-1} - \mathbf{G}_0)^{-1}$, where $\mathbf{t}$ corresponds to the impured potential, eq. (4.50), and note that the structure constant is the same for the host
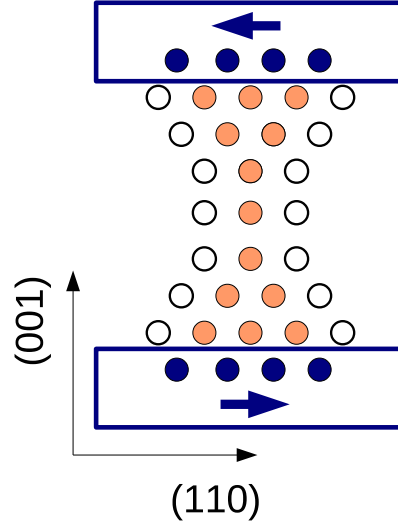
Figure 4.1 Side view of the embedded cluster in the cobalt nanocontact calculation. (Section 5.2.) The physical cluster is the 29 Co atoms (orange circles) between the bulk Co leads. In addition, 16 Co atoms from the bottom lead, 16 Co atoms from the top lead (blue circles) and 80 vacuum spheres (empty circles) around the nanocontact were taken into account in the self-consistent embedded cluster calculation. Blue arrows mark the magnetization of the leads.

and the impured system. Relating this SPO to the host SPO, eq. (4.49), one obtains

$$\boldsymbol{\tau} = \left(\mathbf{t}^{-1} - \mathbf{t}_{\text{host}}^{-1} + \boldsymbol{\tau}_{\text{host}}^{-1} \right)^{-1} = \boldsymbol{\tau}_{\text{host}} \left[\mathbb{1} - \left(\mathbf{t}_{\text{host}}^{-1} - \mathbf{t}^{-1} \right) \boldsymbol{\tau}_{\text{host}} \right]^{-1}. \tag{4.51}$$

From the rightmost expression, using that the $\mathbf{t}$ and the $\mathbf{t}_{\text{host}}$ are site-diagonal matrices, follows that the above equation holds for the cluster block of the $\boldsymbol{\tau}$ matrix:

$$\boldsymbol{\tau}^{\mathcal{CC}} = \left[\left(\mathbf{t}_{\text{imp}}^{\mathcal{C}} \right)^{-1} - \left(\mathbf{t}_{\text{host}}^{\mathcal{C}} \right)^{-1} + \left(\boldsymbol{\tau}_{\text{host}}^{\mathcal{CC}} \right)^{-1} \right]^{-1}, \tag{4.52}$$

where the $\mathcal{C}$ and the $\mathcal{CC}$ upper indices mark that the site indices are confined to the cluster sites. Note, that for the $\mathcal{CC}$ block of the $\boldsymbol{\tau}$-matrix there is no approximation in the above formula.

Note also, that eq. (4.52) should be solved self-consistently, i.e., the charge and magnetization densities are calculated from the latest iteration of $\boldsymbol{\tau}^{\mathcal{CC}}$, then the effective potential and field, $V_{\text{imp}}^n(r_n)$, and from that the single site impurity transition operators, $\mathbf{t}_{\text{imp}}^{\mathcal{C}}$, are updated and eq. (4.52) solved again as next iteration. Around a cluster, charge re-organization and induced magnetization arise which should be also treated self-consistently. For this reason, some environment of the physical cluster is also included in the embedded cluster, $\mathcal{C}$. In this thesis, the first neighbor shell is icluded in addition. As an example, the environment of the cobalt nanocontact (see Section 5.2) is presented in Fig. 4.1. Note, that for the environment atoms, their positions are also restricted to the host lattice.

The magnetic configuration is given by the unit vectors at each site: $\{\boldsymbol{\sigma}_n\}_{n \in \mathcal{C}}$. In terms of the atomic sphere approximation (ASA), the magnitude of the exchange-correlation field,

B_{xc}, is a radial function and the direction, $\hat{\mathbf{B}}_{\mathrm{xc}}$, is homogeneous inside one atomic sphere. The impurity t-matrix can be solved easily in a frame of reference where the exchange-correlation field is parallel to the $\hat{\mathbf{z}}$ direction. The t-matrix corresponding to arbitrary direction of $\hat{\mathbf{B}}_{\mathrm{xc}}$ can be given as the following similarity transformation: [74, 84]

$$\mathbf{t}_{\mathrm{imp}}^{n} = R^{\dagger}(\vartheta_n, \varphi_n)\mathbf{t}_{\mathrm{imp},\,\hat{\mathbf{z}}}^{n} R(\vartheta_n, \varphi_n) \tag{4.53}$$

where $R(\vartheta_n, \varphi_n)$ is a rotation matrix in the angular momentum representation which rotates the z axis into the $\boldsymbol{\sigma}_n$ direction given by the ϑ_n and φ_n polar angles.

4.2 Lloyd formula. Rotational energy

The Lloyd formula [89] can be given in matrix representation based on Eq. (3.134) in Ref. 84:

$$N(\varepsilon, \{\boldsymbol{\sigma}_i\}) = \frac{1}{\pi}\,\mathrm{Im}\,\ln\det\boldsymbol{\tau}(\varepsilon, \{\boldsymbol{\sigma}_i\}) \tag{4.54}$$

where N is the integrated density of states, ε denotes the energy dependence (which is omitted for brevity through Section 4.1), $\{\boldsymbol{\sigma}_i\}$ denotes the dependence on the magnetic configuration, and $\boldsymbol{\tau}$ is the SPO of the system, see Eq. (4.51).

The *band energy* is defined by: [74]

$$E_{\mathrm{b}}(\{\boldsymbol{\sigma}_i\}) = \int_{-\infty}^{\varepsilon_{\mathrm{F}}} (\varepsilon - \varepsilon_{\mathrm{F}})\,n(\varepsilon, \{\boldsymbol{\sigma}_i\})\,\mathrm{d}\varepsilon = -\int_{-\infty}^{\varepsilon_{\mathrm{F}}} N(\varepsilon, \{\boldsymbol{\sigma}_i\})\,\mathrm{d}\varepsilon \tag{4.55}$$

where ε_{F} is the Fermi energy provided by the substrate, n is the density of states and an integration by parts is applied to derive the second equality.

Substituting Eqs. (4.51) and (4.54) into Eq. (4.55) one arrives at

$$E_{\mathrm{b}}(\{\boldsymbol{\sigma}_i\}) = \frac{1}{\pi}\,\mathrm{Im}\int_{-\infty}^{\varepsilon_{\mathrm{F}}} \ln\det\left\{\mathbb{1} + \boldsymbol{\tau}_{\mathrm{host}}^{\mathcal{CC}}(\varepsilon)\left[\mathbf{t}_{\mathrm{imp}}^{\mathcal{C}}(\varepsilon, \{\boldsymbol{\sigma}_i\})^{-1} - \mathbf{t}_{\mathrm{host}}^{\mathcal{C}}(\varepsilon)^{-1}\right]\right\}\mathrm{d}\varepsilon. \tag{4.56}$$

Note that only the (finite) $\mathcal{CC}$ block of the SPO and the t-matrices appear in the Lloyd formula because of the determinant. Note also that a constant shift of the energy not affected by the magnetic configuration is omitted.

Following the method proposed by Szunyogh *et al.* [75, 76] to analyze the magnetic anisotropy of IrMn and IrMn$_3$ ordered alloys and an IrMn$_3$/Co interface the energies of the system are calculated during the simultaneous rotation of the magnetic configuration around an appropriate axis. In the following, this energy will be referred to as *rotational energy*.

The rotational energies were calculated in the spirit of the magnetic force theorem [72]. The effective potentials and exchange fields determined in ground state configurations were kept fixed and the change in energy of the system with respect to the rotational angle is approximated by the change in band energy, Eq. (4.56).

Note that using formula (4.56), the change in the band energy due to the change of the magnetic configuration in cluster $\mathcal{C}$ is accounted for the whole system, while the direct integration of the local DOS in equation (4.55) is always restricted to a given environment of $\mathcal{C}$ only. In other words, the Lloyd formula is accounting for the Friedel oscillations up to infinity.

4.3   Torque method. Relativistic torque method

In the multiple scattering formalism the exchange field enters the electronic structure via the single-site scattering matrix, t_i. The first and higher order changes of the t_i matrices as well as the derivatives of the band energy can straightforwardly be calculated in the local frame of reference introduced at all sites of the cluster, where the direction vector $\boldsymbol{\sigma}_i$ of the magnetization at site i, and the two transverse vectors, $\mathbf{e}_{i1}$ and $\mathbf{e}_{i2}$, form a right-handed coordinate system as shown in Fig. 4.2. The first and second order change of the single site scattering matrix at site i with respect to rotations by $\Delta\phi_{i\alpha}$ around the transverse axes $\mathbf{e}_{i\alpha}$ can be given by the following commutator formulas: [82]

$$\Delta t_i^{(1)} = i[\mathbf{e}_{i\alpha}\mathbf{J}, t_i]\Delta\phi_{i\alpha}, \tag{4.57}$$

$$\Delta t_i^{(2)} = -[\mathbf{e}_{i\alpha}\mathbf{J}, [\mathbf{e}_{i\beta}\mathbf{J}, t_i]]\Delta\phi_{i\alpha}\Delta\phi_{i\beta}, \tag{4.58}$$

where $\mathbf{J}$ is the matrix representation of the total angular momentum operator and $\alpha, \beta \in \{1, 2\}$. Following Ref. 74, the first and second derivatives of the band energy can then be expressed as: [82]

$$\frac{\partial E_\mathbf{b}}{\partial \phi_{i\alpha}} = \frac{1}{\pi}\operatorname{Re}\int\limits_{-\infty}^{\varepsilon_\mathrm{F}} \operatorname{Tr}\left\{\tau_{ii}\left[\mathbf{e}_{i\alpha}\mathbf{J}, m_i\right]\right\}\,\mathrm{d}\varepsilon, \tag{4.59}$$

$$\frac{\partial^2 E_\mathbf{b}}{\partial \phi_{i\alpha}\partial \phi_{j\beta}} = -\frac{1}{\pi}\operatorname{Im}\int\limits_{-\infty}^{\varepsilon_\mathrm{F}} \operatorname{Tr}\left\{\tau_{ij}[\mathbf{e}_{j\beta}\mathbf{J}, m_j]\tau_{ji}[\mathbf{e}_{i\alpha}\mathbf{J}, m_i]\right\}\,\mathrm{d}\varepsilon$$

$$+ \delta_{ij}\frac{1}{\pi}\operatorname{Im}\int\limits_{-\infty}^{\varepsilon_\mathrm{F}} \operatorname{Tr}\left\{\tau_{ii}[\mathbf{e}_{i\alpha}\mathbf{J}, [\mathbf{e}_{i\beta}\mathbf{J}, m_i]]\right\}\,\mathrm{d}\varepsilon, \tag{4.60}$$

where $m_i = t_i^{-1}$ and τ_{ij} is the block of the SPO matrix between sites i and j. Note that for brevity we dropped the energy arguments of the corresponding matrices in Eqs. (4.57)–(4.60).

4.4   Extension to the KKR method: Newton–Raphson method

In general context, the Newton–Raphson method is an iterative method to find a minimum of a function, $f(x)$. The starting guess, x_0, should be close enough to the solution. Then, the iteration process is defind by the following rule:

$$x_{n+1} = x_n - \frac{f'(x_n)}{f''(x_n)}. \tag{4.61}$$
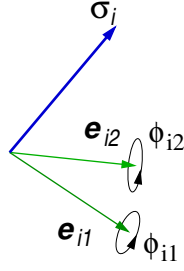
Figure 4.2 Sketch of the local frame of reference. The unit vector $\boldsymbol{\sigma}_i$ is parallel to the magnetization at site i, while the unit vectors $\mathbf{e}_{i1}$ and $\mathbf{e}_{i2}$ point into the transverse directions. Rotations around these axes by ϕ_{i1} and ϕ_{i2} are also indicated.

Applying this to our situation, the magnetic structure dependent band energy, $E_{\mathrm{b}}(\{\boldsymbol{\sigma}_i\})$, is minimized in terms of its degrees of freedom, the $\boldsymbol{\sigma}_i$ vectors. In every iteration step, the changes of the $\boldsymbol{\sigma}_i$ vectors are parametrized by the angles ϕ_{i1} and ϕ_{i2} as presented in Fig. 4.2. The first guess should be set by an other method close to the expected solution, as it is explained in detail in Subsection 5.2.2.

In the spirit of a gradient minimization, rotating the exchange field by a small amount around the torque vector at each sites,

$$\mathbf{T}_i = \mathbf{e}_{i1} \frac{\partial E_{\mathrm{b}}}{\partial \phi_{i1}} + \mathbf{e}_{i2} \frac{\partial E_{\mathrm{b}}}{\partial \phi_{i2}}, \tag{4.62}$$

the magnetic configuration gets closer to the local minimum of the energy; however, the convergence is very slow. In order to speed up this procedure, a Newton-Raphson iteration scheme has been applied, where the inverse of the second derivative tensor, also referred to as the Hessian, Eq. (4.60), is used to estimate the angle of rotations around the torque vector given by Eq. (4.62). The eigenvalues of the Hessian also provide information about the stability of a configuration with zero torque: If the Hessian is a positive or negative definite matrix then the given configuration is stable or unstable state of equilibrium, respectively. Once the Newton-Raphson iteration has converged, new effective potentials and exchange fields are generated and the procedure is repeated until the effective potential converges and the torque in Eq. (4.62) is decreased below a predefined value of, typically, 10^{-4} meV.

4.5   Extension to the KKR method: Monte Carlo method

A widely used method to describe magnetic systems coupled to a heat bath is the Monte Carlo (MC) method. MC methods generate an appropriate random series of states according to the Boltzmann distribution. Using this series of states the expectation value, $\langle Q \rangle$, of some quantity, Q, is simply

$$\langle Q \rangle = \frac{1}{M} \sum_{i=1}^{M} Q_{s_i} \tag{4.63}$$

where the $s_1, s_2, \ldots, s_M$ states have been generated and Q_s is the value of the quantity of interest in the state s.

The probability of generating a new state, s', out of the previous state, s, is $P(s \rightarrow s')$. Almost all MC scheemes rely on a Markov process which means that the transition probabilities, $P(s \rightarrow s')$, depend only on s and s' but do dot depend on time or any former state. [90] In such a MC method "only the irreversible part of the dynamics of the system is considered including the relaxation and the fluctuation, but not the energy conserving part of the equation of motion – the precession." [8]

In many MC algorithms the generation of the state s' out of the state s is divided into two steps. First, a new target state is selected with $g(s \rightarrow s')$ selection probability, then we change our system into the new state, s', with an acceptance ratio of $A(s \rightarrow s')$ and stay in state s with a ratio of $1 - A(s \rightarrow s')$. Obviously, the transition probability is the product of the selection probability and the acceptance ratio:

$$P(s \rightarrow s') = g(s \rightarrow s')A(s \rightarrow s'). \tag{4.64}$$

The algorithm must be ergodic which means that the algorithm should be able to "reach any state of the system from any other state, if we run it for long enough." [90]

The detailed balance requires

$$\frac{P(s \rightarrow s')}{P(s' \rightarrow s)} = \mathrm{e}^{-\beta(\mathcal{H}(s') - \mathcal{H}(s))} \tag{4.65}$$

where $\beta = 1/(k_\mathrm{B}T)$ is the inverse temperature and $\mathcal{H}(s)$ is the energy of the system in state s. Satisfying the detailed balance ensures that the distribution of the states generated by the above Markov process tend to an equilibrium distribution and this is the Boltzmann distribution. [90] In the present thesis a symmetric algorithm is used, i.e., $g(s \rightarrow s') = g(s' \rightarrow s)$ for any states s and s'. The Metropolis algorithm [91] is used for the acceptance ratios:

$$A(s \rightarrow s') = \begin{cases} \mathrm{e}^{-\beta(\mathcal{H}(s') - \mathcal{H}(s))} & \text{if } \mathcal{H}(s') - \mathcal{H}(s) > 0 \\ 1 & \text{otherwise.} \end{cases} \tag{4.66}$$

In this thesis a Monte Carlo simulation is applied with the Metropolis algorithm for the band energy of the system, $E_\mathrm{b}(\{\boldsymbol{\sigma}_i\})$. Single spin flip dynamics is applied to ensure detailed balance and the trial directions were chosen uniformly on the surface of the unit sphere.

4.6 Summary of the approximations used in this thesis

There are many approximations used in the calculations. The general approximations are listed here:

- The effective potentials and fields were treated within the atomic sphere approximation (ASA).

Table 4.1 The clusters of this thesis with their basic characteristics: in which section they are discussed, the atoms forming the physical cluster, the environment atoms and the total number of atoms in the embedded cluster (EC).

Cluster name	Section	Physical cluster	Environment	Total EC
Square Co cluster	5.1	16 Co	—	16
Co nanocontact	5.2	29 Co	32 Co, 80 vacuum	141
Fcc up Cr trimer	5.3.2	3 Cr	6 Au, 16 vacuum	25
Fcc down Cr trimer	5.3.2	3 Cr	7 Au, 15 vacuum	25
Hcp up Cr trimer	5.3.2	3 Cr	7 Au, 16 vacuum	26
Hcp down Cr trimer	5.3.2	3 Cr	6 Au, 15 vacuum	24

- The local spin-density approximation (LSDA), [86, 87] of the density functional theory as parametrized by Perdew and Zunger [88] was applied for both the layered hosts and the clusters.

- A cutoff of $\ell_{max} = 2$ for the angular momentum expansion was used. See, e.g., Eq. (4.43) and Table A.1.

- 3 physical layers are held together into one principal layer. (See Subsection 4.1.7.)

- 3300 k-points were used in the irreducible wedge of the surface Brillouin zone (SBZ). We have checked the accuracy of the SBZ-integrals by performing the same calculations using 1900 k-points in the irreducible wedge of the SBZ and a deviation of up to 4 % was found in the resulting model parameters, see Table 5.4.

- The energy integration in Eq. (4.56) was performed by sampling 16 points on a semicircular path in the upper complex semi-plane.

- The size of the self-consistently calculated finite cluster also has stressed effect on the results. The clusters in this thesis together with their considered environments are summarized in Table 4.1.

- The energy of the different magnetic configurations is determined by using the band energy within the magnetic force theorem [72].

In the following, some further computational details are given correspondig various parts of the thesis.

Layered host for the Co/Co(001) calculations (Section 5.2)

The host system assembled of two oppositely magnetized semi-infinite Co leads and separated by 7 layers of empty spheres (vacuum) is considered.

Layered host for the Cr/Au(111) calculations (Subsection 5.3.2)

For the chromium cluster calculations the interface region was composed of 4 Au layers and 5 vacuum layers.

Cr/Au(111) monolayer calculations (Subsection 5.3.3)

For the chromium monolayer studies the self-consistently calculated region was composed of 4 Au layers, one Cr layer and 4 layers of empty spheres (vacuum) between the semi-infinite bulk Au and the semi-infinite vacuum with no attempt at geometric relaxation.

"To ensure that both the" Cr layer (in planar Néel magnetic configuration) and the Au supporter " share the same two-dimensional translational periodicity, which is necessary within the layered SKKR method for an interface, the calculations " [76] for the monolayer studies were carried out with three atoms per unit cell, i.e., the magnetic unit cell of the Néel configuration. Note, that in the case of the non-magnetic layered system serving as the host system for the cluster calculations one atom per unit cell 2D lattice was used.

Chapter 5

Results

5.1 Monte Carlo study on magnetic nanoparticles from first principle

In this chapter the result of the *ab initio* MC method is presented through a square-shaped Co cluster deposited onto a Cu(100) surface. Using this approach an attempt is made at mixing the advantages of a spin model based MC method and the *ab initio* calculation. In low symmetry clusters the coupling parameters between the spins is not a trivial task to determine. Moreover, theoretical studies on small Cr clusters on Au (111) surface pointed out [15] that higher order spin-spin interactions must not be neglected when fitting a spin model to the *ab initio* results. In order to overcome these complications, an *ab initio* MC simulation is presented where the change of the energy for every MC step is calculated directly from the electronic structure of the cluster. An unambiguous drawback of the *ab initio* simulation is the extreme computational demand compared to a spin model simulation.

For a test of this new type of finite temperature *ab initio* simulation, the temperature dependence of the magnetization of a square-shaped cobalt cluster deposited on a Cu(100) surface has been calculated and compared with the results of a MC simulation based on a classical Heisenberg model. In this Heisenberg model isotropic exchange coupling between all pair of spins and a uniform uniaxial easy-plane anisotropy ($K > 0$) were taken into account:

$$\mathcal{H}^{\text{model}} = \sum_{\langle i,j \rangle} J_{ij} \left(\boldsymbol{\sigma}_i \cdot \boldsymbol{\sigma}_j \right) + K \sum_i (\sigma_i^z)^2. \tag{5.1}$$

The exchange couplings were determined for the 4×4 cluster using the method described in ref. 74. In order to speed up the simulation, only the 16 cobalt atoms formed the embedded cluster in the EC-KKR calculation. The nearest neighbor couplings are visualised in fig. 5.1. The spin magnetic moments of the non-equivalent sites were found as $m_1 = 1.74\,\mu_{\text{B}}$, $m_5 = 1.82\,\mu_{\text{B}}$ and $m_6 = 1.87\,\mu_{\text{B}}$. An enhancement of the nearest neighbor exchange couplings has been found at the corners and the edges of the cluster. Interestingly, an opposite tendency has been seen for the magnetic moments. The anisotropy constant was chosen to be the same as that of a Co monolayer on the Cu(001), $K = 0.310\,\text{meV}$.
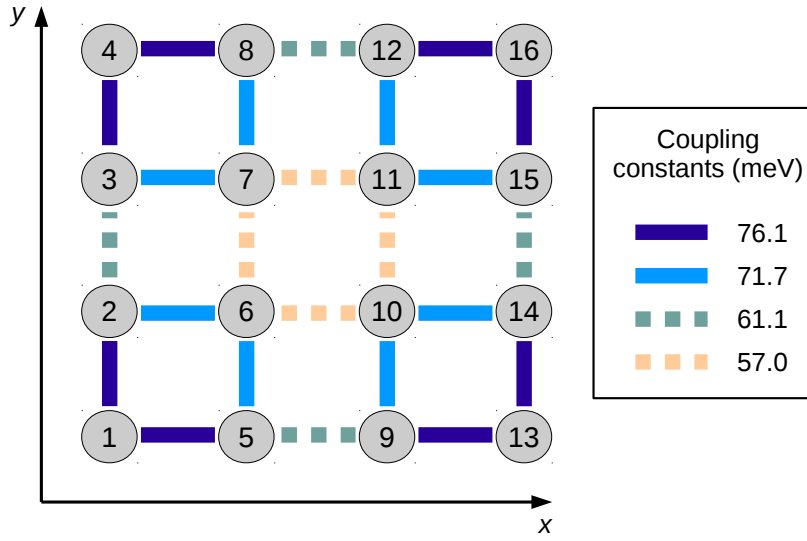
Figure 5.1 The positions of the cobalt atoms and the nearest neighbor isotropic exchange couplings between them in the 4×4 size cluster.

Since the cluster is small the simultaneous flipping of the magnetization cannot be ruled out. When it happens multiple times during a simulation the simple average of the z component of the magnetization would tend to zero. In order to see the magnetic arrangement of the cluster the square of the magnetization is averaged as:

$$\langle m \rangle = \sqrt{\left\langle \sum_{i=1}^{16} \boldsymbol{\mu}_i^2 \right\rangle} \tag{5.2}$$

where $\boldsymbol{\mu}_i$ is the magnetization vector of atom i and $\langle \ldots \rangle$ means the thermal average.

For comparison, the thermal average of the square of the magnetization of the cluster was calculated by the two methods. At a given temperature 10^5 MC steps were performed in the Heisenberg MC simulations, and 5 independent samples, with 10^4 MC steps each, were performed in the *ab initio* MC simulation in order to see the spreading of the data. (See fig. 5.2.) Since the magnetic anisotropy is small for the present system, the simulation based on the Heisenberg model was expected to give similar dependence of the magnetization on the temperature as our ab-initio simulation. The two result are in good agreement as shown in fig. 5.2.
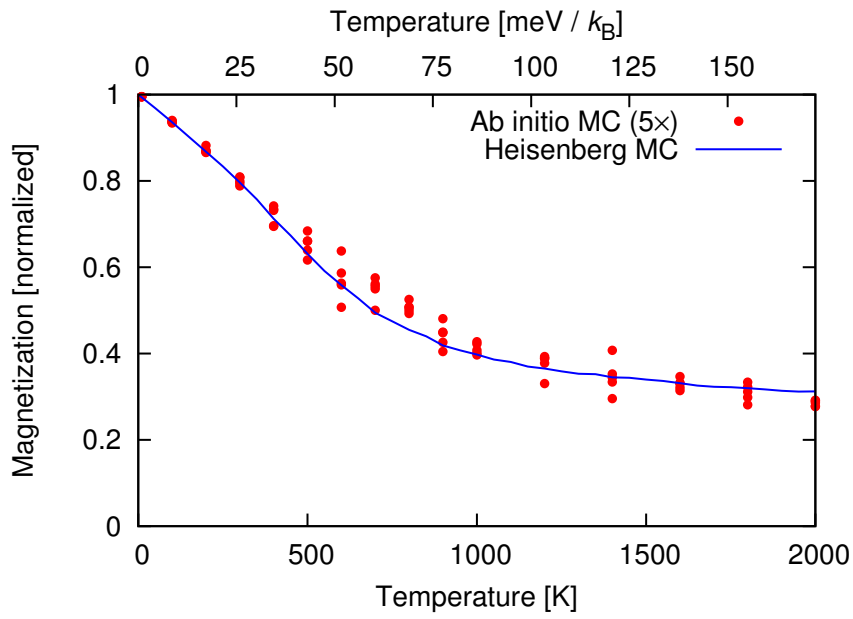
Figure 5.2   Square root of the thermal average of the square of the magnetization [see eq. (5.2)] for a 4×4 Co cluster on a Cu(001) surface. The solid line represents the magnetization of the Heisenberg model, points refer to the 5 independent samples of the *ab initio* MC calculation. The temperature scale is given in kelvins (bottom scale) and in milli-electronvolts (top scale).

5.2 Domain wall through a cobalt nanocontact

In this section, a domain wall through a Co point contact between (001) surfaces of fcc Co is studied, where the magnetizations are aligned in the (110) and the ($\overline{1}10$) directions in the leads. An Fe break junction between bcc Fe surfaces was studied both experimentally and theoretically by Autès *et al.* [26] Using a "head-to-head square pyramids" geometry the anisotropic magneto-resistance (anisotropic MR) is explained by "the existence of two metastable electronic states which differ mainly by the direction of the spin and orbital moment on the central atom". [26] The geometrical model of the present Co point contact is decribed in Subsection 5.2.1. Note that this geometrical model is almost the same (shorter) as the one labeled by C2 in Ref. 26, except that there a break junction between bcc Fe surfaces was studied. It should be noted that Co exhibits a hcp structure in bulk; however, as a thin film it often displays a fcc-related geometry.

The contradicting boundary condition enforces a magnetic domain wall to be formed through the contact. Bruno [31] investigated a continuum model of magnetic material incorporating exchange interaction and uniaxial anisotropy applied to a constriction separating two wider regions. "A new kind of magnetic wall, besides the well known Bloch and Néel walls," the *geometrically constrained magnetic wall* is described with a wall width highly related to the geometry of the constriction rather then the material parameters. [31] In the case of $Fe_{20}Ni_{80}$ thin films it has been experimentally found that the constrained geometry can reduce the width of the Néel wall. [92] The effect is more pronounced in ultrathin films of a few atomic layers where the width of the domain wall can be as small as a few nanometers in the vicinity of a step edge. [93] The domain wall structure of the Co contact is discussed in Subsection 5.2.2.

The electronic structure of the nanocontact is calculated with the fully relativistic EC-KKR method, see Subsection 4.1.8. The ground state configuration is found by the Newton–Raphson method which is described in Section 4.4. An enhancement of the magnetic anisotropy energy has been established theoretically by Thiess *et al.* [94] in atomic scale junctions even for elements that are nonmagnetic in bulk. In agreement with this finding, the presented results reveal that the central atom with the lowest coordination number has the main contribution to the magnetic anisotropy of the contact. To highlight the relationship between the obtained cycloidal domain wall configuration and the magnetic anisotropy, the orientational dependence of the band energy of the point contact is analyzed in detail, see Subsections 5.2.3 – 5.2.5.

5.2.1 Geometry

The model of the atomic-sized point contact has been built from Co atoms forming two identical pyramids facing each other between (001) interfaces of fcc Co as it is shown in fig. 5.3 (a) and (b). The distance between the central atom and its neighbors was chosen identical to the fcc nearest neighbor distance, a, of 2.506 Å. Inspired by the STM layout it was a natural
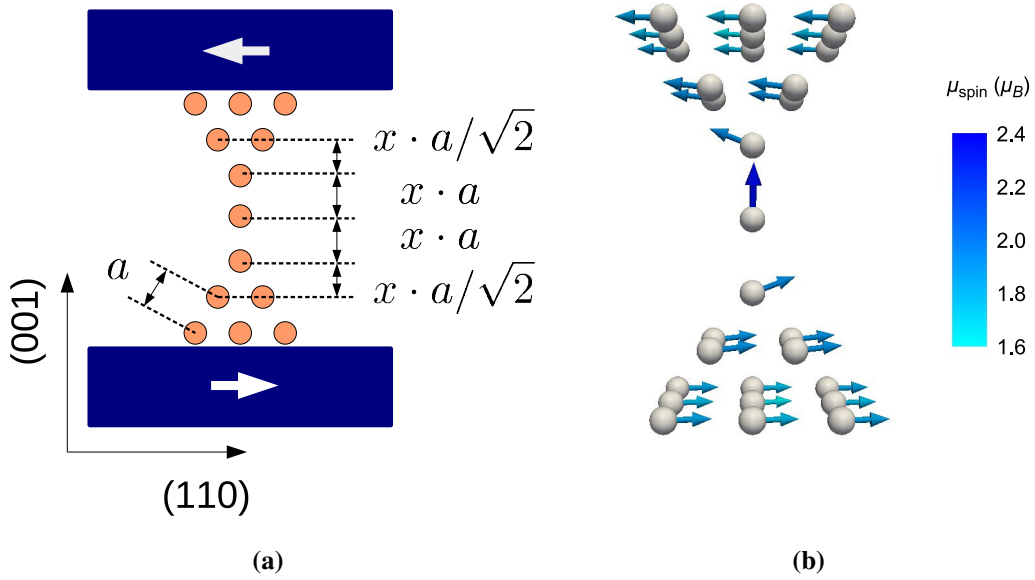
Figure 5.3 **(a)** The geometry of the contact viewed from the $(1\bar{1}0)$ direction. The semi-infinite cobalt leads are depicted as blue rectangles, the directions of magnetization in the leads are marked by white arrows, the cobalt atoms forming the contact are represented by orange circles, and a denotes the nearest neighbor distance in the fcc structure. The length of the contact is tuned via $x = 0.85, 0.90, 0.95, 1.00, 1.05, 1.10$, and 1.15. Note that only the marked distances were scaled. **(b)** The perspective view of the contact. The arrows show the ground state spin configuration obtained for the unstretched contact ($x = 1$). This configuration is called the *cycloidal wall* (CW) configuration. The lengths of the arrows, indicated also with color coding, are proportional to the size of the spin magnetic moments.

idea to mimic the contraction and expansion of the contact: The normal-to-plane distances in the vicinity of the central atom have been scaled by a factor, hereinafter denoted by x, between 0.85 and 1.15, see fig. 5.3 (a). Through this section many results will be presented as a function of the stretching factor, x. By doing this, trends and robust phenomena can be presented.

Due to the symmetry of the system the central atom is the middle of the domain wall. In the (constrained) magnetic ground state the magnetisation of the central atom points to one of the $(1\bar{1}0)$ or the (001) high symmetry directions. In the first case, the magnetic moments at all sites (layers) remain within the (001) plane, i.e., normal to the axis of the point contact; therefore, in the following this spin configuration will be termed as a *helical domain wall* (HW). In the second case, all the spin moments are confined to the $(1\bar{1}0)$ plane; thus, we shall call this case the *cycloidal domain wall* (CW), see fig. 5.3 (b), Note that the helical and cycloidal spin configurations closely resemble the Bloch and Néel types of domain walls well known in bulk and thin-film magnets, respectively. Since, however, these types of domain walls are distinct through the magnetostatic energy, to avoid confusion we skipped using the traditional terminology.

5.2.2 Domain wall configurations

A first guess of the domain wall configuration has been given by Monte Carlo (MC) simulated annealing based on a simple isotropic Heisenberg model, $\mathcal{H} = \frac{1}{2} \sum_{i \neq j} J_{ij} \boldsymbol{\sigma}_i \boldsymbol{\sigma}_j$, where J_{ij} is the isotropic exchange coupling between sites i and j. The coupling coefficients between the atomic moments were calculated by using the torque method proposed by Liechtenstein *et al.* [73] The exchange field directions were set in a ferromagnetic configuration parallel to the (110) direction in the case of the self-consistently calculated potentials used for the above exchange coupling calculation. The magnetization of the central atom was fixed in the $(1\bar{1}0)$ and the (001) directions during the MC simulated annealing providing the first guess for the helical and the cycloidal domain walls, respectively. Note, that in an isotropic model there is no energy difference between these two domain walls.

Self-consistent potentials and exchange fields have been first determined for both the cycloidal and the helical domain walls using the configurations from the above MC simulated annealing. Then, the Newton-Raphson iterations (see sec. 4.4) were started from both initial configurations. Interestingly, when starting from a helical spin configuration, the gradients, eq. (4.59), were initially zero, but the Hessian, eq. (4.60), had a negative eigenvalue indicating that the helical spin configuration belonged to a saddle point of the energy surface. Throwing the system off this saddle point, the Newton–Raphson iterations converged to the cycloidal spin-configuration. Thus, independent of the starting configuration, the magnetic state of the nanojunction converged to the cycloidal wall structure for the stretching range considered. In fig. 5.3(b) the ground-state cycloidal wall configuration is displayed for $x = 1$.

At sites within the same geometrical layer, fairly similar orientations for the magnetic moments were obtained; therefore, the shape of the domain wall can well be characterized by orientations determined as an average within layers. In fig. 5.4 such a profile is shown for $x = 1$ in terms of polar angles, $\vartheta(z)$. Remarkably, the well-known analytical form, $\vartheta(z) = -\frac{\pi}{2} \tanh(2z/d_{\rm w})$, could be well fitted defining, thus, the width of the domain wall, $d_{\rm w}$. This fit is also shown in fig. 5.4.

The change of the width of the domain walls against the length of the point contact is shown in fig. 5.5. For a clear interpretation, the width of the walls is normalized to the width of the domain wall for $x = 1$. As is obvious from this figure, $d_{\rm w}(x) \approx x \, d_{\rm w}(1.00)$ demonstrating that the width of the domain walls follows the length of the point contact. Since the exchange energy gain for the few atoms of the contact is small compared to the increase of the exchange energy of the leads, the domain wall cannot penetrate into the substrates and the wall is confined to the contact.

5.2.3 Magnetic moments

The low coordination number in thin films and in nanostructures is often accompanied by the enhancement of the atomic spin and orbital moments. In fig. 5.6 the calculated values of the local spin and orbital moments are given in a point contact with cycloidal wall configuration and stretching factor, $x = 1$. Since the orbital moment is found almost parallel to the spin
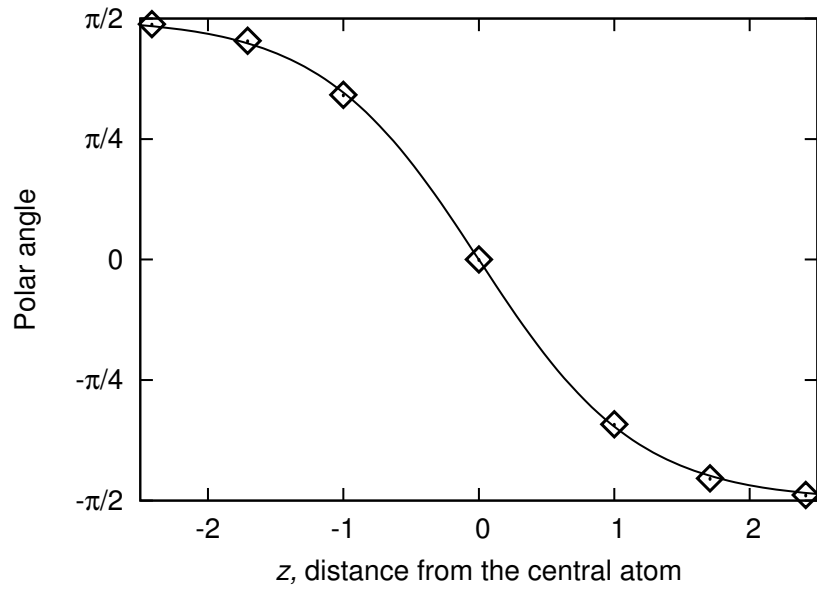
Figure 5.4   Polar angles averaged within a layer of cobalt atoms in the contact with $x = 1$ as the function of the distance from the central atom (in units of the fcc nearest neighbor distance, a). The solid curve displays the fit, $\vartheta(z) = -\frac{\pi}{2}\tanh(2z/d_\mathrm{w})$; $d_\mathrm{w} = 2.34\,a$ in this case.
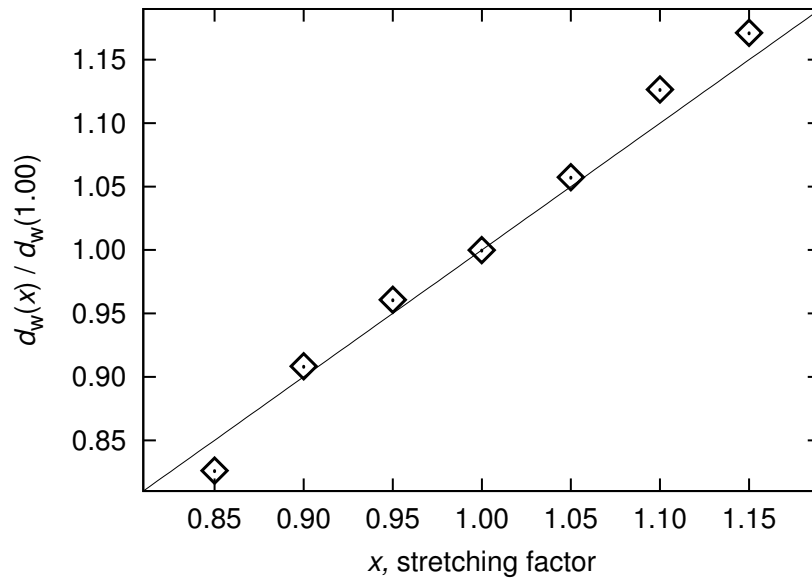
Figure 5.5   Width of the domain walls through the point contact as a function of the stretching factor, x. Note that $d_\mathrm{w}(1.00) = 2.34\,a$, where a is the fcc nearest neighbor distance. The solid line stands for the identity function.

Figure 5.6 Calculated atomic magnetic moments (μ_B) in half of the nanocontact for the stretching factor, $x = 1$. In the upper and lower panels shown are the spin and orbital moments, μ_{spin} and μ_{orb}, respectively. For comparison, the spin moments at the Co surface and in the bulk are $1.82\,\mu_B$ and $1.67\,\mu_B/\text{atom}$, while the corresponding values of the orbital moments are $0.14\,\mu_B$ and $0.08\,\mu_B$.

moment at each site, we presented the projection of the orbital moment to the local spin quantization axis. Since the contact has a mirror symmetry with respect to the horizontal plane including the central atom, the moments in only one half of the contact are displayed. Our data fit nicely the observation reported in refs. 95 and 96 that the spin and orbital moments at sites with lower coordination number are larger then at sites with larger coordination number. This is, in particular, true for the central atom with coordination number of only two where the values of the spin and orbital moments are even larger than those obtained for small clusters on Pt(111) and Au(111) surfaces. [95–97]

Figure 5.7 shows the spin and orbital moments of the central atom as a function of the stretching ratio x, for both the cycloidal and the helical spin configurations in the point contact. Clearly, the spin moments are fairly insensitive to the domain wall configuration: This can easily be understood as the relative spin directions are nearly the same in the two types of domain walls. Also, there is only a moderate change of the spin moment in the range of $2.35\,\mu_B \leq \mu_{\text{spin}} \leq 2.49\,\mu_B$ for the stretching ratios under consideration. These values compare well to $\mu_{\text{spin}} = 2.15\,\mu_B$ and $\mu_{\text{spin}} = 2.26\,\mu_B$ calculated for a single Co adatom on Pt and Au(111) surfaces in refs. 95 and 96, respectively.

The dependence of the orbital moment of the central atom on the stretching is more pronounced than that of the spin moment: In the case of a cycloidal and a helical wall it increases from about $1\,\mu_B$ to $2\,\mu_B$ and from $0.3\,\mu_B$ to $1.5\,\mu_B$, respectively. Similar high values of μ_{orb} for the central atom of a wire like Fe point contact were reported in ref. 26 and attributed to localized atomic-like electronic states treated within a full Hartree-Fock scheme. It should be
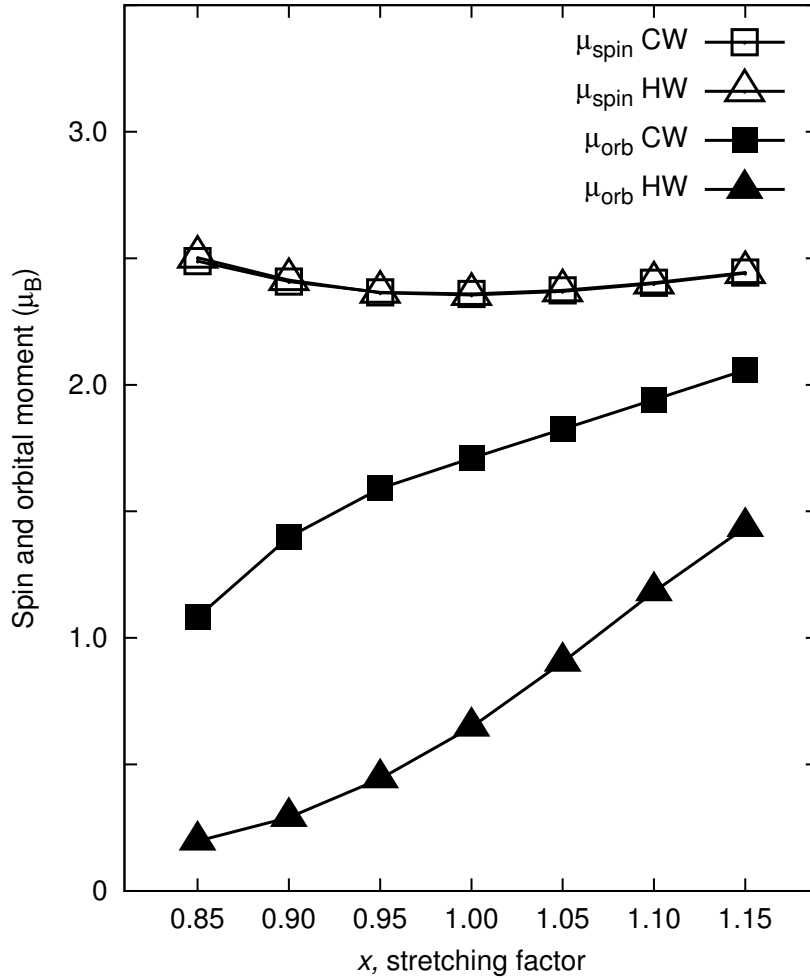
Figure 5.7   The spin and orbital moments of the central atom as a func-
tion of the stretching. Spin moments are displayed by open symbols; or-
bital moments are displayed by filled symbols as calculated in the cycloidal
wall (CW, squares) and in the helical wall (HW, triangles) configurations.

mentioned that for a more reliable description of highly localized states, the plain LSDA we
used in our calculations should be extended with, e.g., the local self-interaction correction,
LSDA+SIC, [98] or the dynamical mean field theory, LSDA+DMFT. [99]

Apparently, the orbital moment of the central atom is systematically larger in a cycloidal
wall than in a helical wall. This can be understood since these orbital moments correspond to
different directions: In the case of a cycloidal wall it points along the (001) directions, while
for a helical wall, along the $(1\bar{1}0)$ direction. Such a huge anisotropy of the orbital moment at
the central atom has also been observed in ref. 26. The anisotropy of the orbital momentum
is compared with the magnetic anisotropy energy in Subsection 5.2.5.

5.2.4 Rotational energy of the domain wall

The cycloidal and helical spin configurations of the point contact can be transformed into
each other in term of a simultaneous rotation of the spin directions around the axis parallel
to the magnetization of the leads. The energy along the path of this global rotation, termed

the *rotational energy* of the domain wall, was calculated using the magnetic force theorem, namely, from the band energy of the system by rotating the orientation of the exchange field at each atomic site around the (110) axis and keeping frozen the effective potentials and fields as obtained for the ground-state cycloidal wall configuration. For the case of the unstretched configuration the results are plotted in fig. 5.8. The two minima and maxima of the band energy belong to the twofold degenerate cycloidal and helical domain wall configurations. The height of the energy barrier between the two ground-state cycloidal spin configurations is 32.0 meV. Similar behavior has been found for the whole stretching range of the point contact. The energy differences between the two types of domain walls as a function of the stretching ratio are displayed by diamonds in fig. 5.9.

Due to time reversal symmetry, the magnetic anisotropy energy has a periodicity of π, but it does not comply with a usual $\cos^2(\theta)$ dependence. To explore this deviation we performed the Fourier expansion,

$$E_{\mathrm{b}}(\theta) = K_0 + \sum_{k=2,4,\dots}^{\infty} K_k \cos(k\theta), \tag{5.3}$$

for the contacts with different stretching. Note that because of the inversion symmetry of the contact $E_{\mathrm{b}}(\theta) = E_{\mathrm{b}}(\pi - \theta)$ applies, and the $\sin(k\theta)$ ($k = 2, 4, \dots$) terms do not appear in the expansion, eq. (5.3). The Fourier coefficients, K_k, are summarized in tab. 5.1. It is found that in each case the term $K_2 \cos(2\theta)$ adds the largest weight to the rotational energy of the domain wall. The $k \geq 8$ terms of the Fourier expansion have practically vanishing weight.

5.2.5 Magnetic anisotropy of the central atom

As it has been seen in Subsection 5.2.3, the central atom of the contact exhibits a huge orbital moment anisotropy that should be accompanied by a large magnetic anisotropy energy. [12] For that reason, the band energy of the point contact, $E_{\mathrm{b}}(\boldsymbol{\sigma})$, with $\boldsymbol{\sigma}$ denoting the spin orientation at the central atom, has been analized whereas the spin orientations of all the other sites in the contact are kept fixed as obtained in the ground-state cycloidal wall configuration.

The analysis is based on an expansion of $E_{\mathrm{b}}(\boldsymbol{\sigma})$ in terms of (real) spherical harmonics, $R_\ell^m(\boldsymbol{\sigma})$,

$$E_{\mathrm{b}}(\boldsymbol{\sigma}) = \sum_{\substack{\ell=0,1,2,\dots \\ -\ell \leq m \leq \ell}} K_\ell^m R_\ell^m(\boldsymbol{\sigma}). \tag{5.4}$$

The definition of the R_ℓ^m functions is given in tab. 5.2. Similar to the rotational energy of the domain wall, we used the magnetic force theorem to evaluate $E_{\mathrm{b}}(\boldsymbol{\sigma})$, but here we employed Lloyd formula, [89] since it accurately accounts for the change of the band energy of the whole point contact with respect to the change of the spin orientation at the central site. For the expansion, the integration over $\boldsymbol{\sigma}$ was performed using a 51-point Gaussian quadrature along the z direction and a uniform mesh of 100 points in the azimuth angle, resulting in a spherical grid of 5100 points. The obtained coefficients are summarized in tab. 5.2 up to $\ell = 4$ and for all the stretching ratios under consideration.
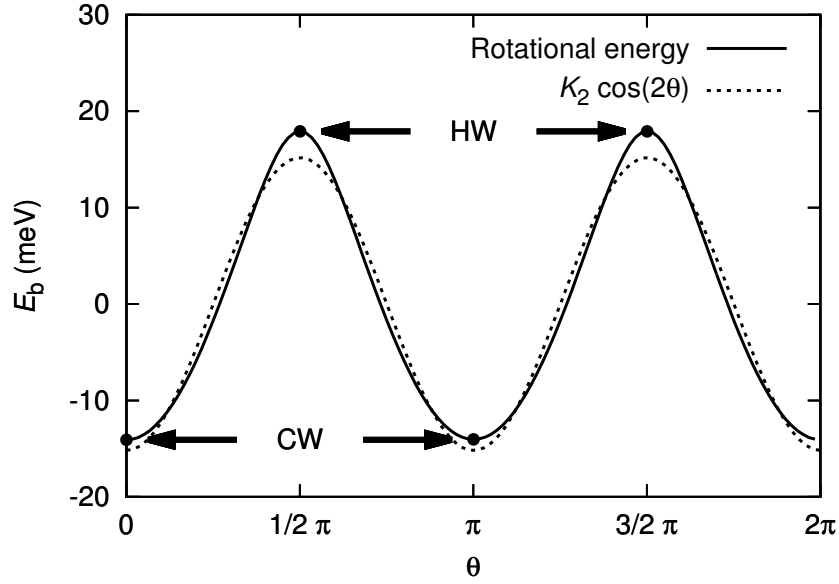
Figure 5.8   The band energy of the nanocontact with $x = 1.00$ while rotating the exchange field at each atomic site simultaneously around the (110) axis. By rotating all the spins by $90°$ the system goes over from the cycloidal wall (CW) into the helical wall (HW). The dashed line denotes the leading Fourier component of the band energy, $-15.2\,[\text{meV}]\cos(2\theta)$; see Eq. (5.3). Note that the zero level of the energy is shifted to the constant term, K_0.

Table 5.1   The $k = 2$, 4, and 6 Fourier coefficients (in units of meV) of the rotational energy of the point contact, eq. (5.3), as a function of the stretching parameter, x.

x	K_2	K_4	K_6
0.85	-6.3	0.15	0.397
0.90	-10.0	0.36	0.499
0.95	-13.6	1.40	0.298
1.00	-15.2	2.17	-0.040
1.05	-15.1	2.35	-0.122
1.10	-14.4	2.24	-0.083
1.15	-13.2	1.92	0.025

Table 5.2 Expansion coefficients, K_ℓ^m, (in units of meV) of the band energy of the contact, see eq. (5.4), according to real spherical harmonics, R_ℓ^m, up to $\ell = 4$. Only the nonvanishing coefficients are presented.

ℓ	m	R_ℓ^m	$K_\ell^m(x);\quad x = \dots$						
			0.85	0.90	0.95	1.00	1.05	1.10	1.15
1	0	$\frac{1}{2}\sqrt{\frac{3}{\pi}}z$	-240	-247	-235	-212	-192	-176	-159
2	0	$\frac{1}{4}\sqrt{\frac{5}{\pi}}\left(3z^2-1\right)$	-25.3	-30.0	-33.2	-32.4	-30.9	-28.4	-25.6
2	2	$\frac{1}{4}\sqrt{\frac{15}{\pi}}\left(x^2-y^2\right)$	4.30	2.54	1.39	0.51	-0.29	-0.92	-1.36
3	0	$\frac{1}{4}\sqrt{\frac{7}{\pi}}\left(5z^3-3z\right)$	4.12	3.06	1.63	0.71	-0.28	-1.43	-2.67
3	2	$\frac{1}{4}\sqrt{\frac{105}{\pi}}\left(x^2-y^2\right)z$	-0.199	-0.093	0.004	0.108	0.196	0.267	0.293
4	0	$\frac{3}{16}\sqrt{\frac{1}{\pi}}\left(35z^4-30z^2+3\right)$	-0.63	1.72	4.60	4.94	5.05	4.85	4.32
4	2	$\frac{3}{8}\sqrt{\frac{5}{\pi}}\left(x^2-y^2\right)\left(7z^2-1\right)$	0.033	0.125	0.184	0.108	0.051	0.001	-0.052
4	4	$\frac{3}{16}\sqrt{\frac{35}{\pi}}\left(x^4-6x^2y^2+y^4\right)$	-0.007	-0.005	-0.018	-0.041	-0.088	-0.187	-0.345

The absence of certain spherical harmonics in expansion eq. (5.4) can be discussed based on group-theoretical arguments. The function $E_{\rm b}(\boldsymbol{\sigma})$ should be invariant under symmetry transformations, g, of the point contact, $E_{\rm b}(\boldsymbol{\sigma}) = E_{\rm b}(g\boldsymbol{\sigma})$, including the symmetry of both the lattice and the given (cycloidal) spin configuration. Regarding that the spin vectors transform as axial vectors, the only allowed transformation is the reflection onto the (001) plane: $(x, y, z) \to (-x, -y, z)$. Thus it is concluded that only those functions can enter the expansion of $E_{\rm b}(\boldsymbol{\sigma})$ that contain even powers of the variables x and y. As seen from tab. 5.2, this is fully confirmed by the calculations. Apparently, the expansion eq. (5.4) shows a satisfactory decay as the coefficients rapidly decrease with increasing ℓ. Noticeably, among the terms with a given ℓ, the one associated with the z component of the magnetization ($m = 0$), i.e., excluding in-plane anisotropy, has the largest weight.

In order to connect the above results to the rotational energy of the domain wall discussed in Subsection 5.2.5, eq. (5.4) is related to the Heisenberg model of the form eq. (1.1). The energy in eq. (5.4) can be expressed as

$$E(\boldsymbol{\sigma}) = E_{\rm anis}(\boldsymbol{\sigma}) + \boldsymbol{\sigma} \sum_j \mathbf{J}_{{\rm c}j} \boldsymbol{\sigma}_j \,, \tag{5.5}$$

where $\mathbf{J}_{{\rm c}j}$ denote the exchange coupling tensor between the central site and the other sites of the contact with classical spin vectors, $\boldsymbol{\sigma}_j$, and $E_{\rm anis}(\boldsymbol{\sigma})$ stands for the on-site anisotropy energy that, due to the tetragonal (D_{4h}) point-group symmetry of the point contact, can be expanded up to $\ell = 4$ as

$$E_{\rm anis}(\boldsymbol{\sigma}) = K_2^0 R_2^0(\boldsymbol{\sigma}) + K_4^0 R_4^0(\boldsymbol{\sigma}) + K_4^4 R_4^4(\boldsymbol{\sigma}) \,. \tag{5.6}$$

The $(\ell, m) = (1, 0)$ term in eq. (5.4) is related to the exchange coupling and, due to the presence of a cycloidal wall, it represents a strong Weiss field along the z direction. Because of the increasing distances between the central site and the other sites of the contact, it is also easy to understand why this term significantly decreases with increasing stretching ratio. Note that the contribution of the Weiss field is canceled in eq. (5.3) since in that case the relative orientation of the spins is unchanged.

In relation to eq. (5.6), the terms proportional to R_2^0, R_4^0, and R_4^4 in eq. (5.4) can mainly be attributed to on-site anisotropy contributions to the spin Hamiltonian; however, the effect of higher order spin interactions cannot be ruled out. The second-order uniaxial anisotropy coefficients, K_2^0, are negative in the whole range of stretching, favoring thus a normal-to-plane direction. Remarkably, the magnitude of K_2^0 is around $30\,{\rm meV}$, with a maximum of $\left|K_2^0\right| = 33.2\,{\rm meV}$ at $x = 0.95$. This value should be compared to some results communicated in the literature: Etz *et al.* [100] and Bornemann *et al.* [101] calculated 5.3 meV and 4.76 meV, respectively, for the MAE of a Co adatom on the Pt(111) surface, while, including orbital polarization, Gambardella *et al.* [45] obtained 18.45 meV for the same system. In a similar geometrical confinement of an atomic scale junction, W and Ir turned out to be magnetic with a magnetic anisotropy energy comparable to the above values. [94]

A brief comment is made on the terms corresponding to $(\ell, m) = (2, 2), (3, 0), (3, 2)$, and $(4, 2)$ in tab. 5.2. Since these terms are not invariant under transformations of the D_{4h} point group, they cannot be accounted for the on-site anisotropy terms. In terms of a spin model, these terms should, therefore, be related to higher order spin interactions. The $(\ell, m) = (2, 2)$ term can, e.g., be identified as the consequence of biquadratic interactions, [79] $\sum_i B_{ci}(\boldsymbol{\sigma}\boldsymbol{\sigma}_i)^2$, while the $\ell = 3$ terms of triquadratic interactions, [102] $\sum_i T_{ci}(\boldsymbol{\sigma}\boldsymbol{\sigma}_i)^3$. Four-spin interactions have been explicitly calculated and proved to give significant contributions to a spin Hamiltonian of Cr trimers deposited on the Au(111) surface by Antal *et al.*, [15] but recently their presence was highlighted even in bulk magnets. [103]

From fig. 5.8 and tab. 5.1 it can be inferred that the rotational energy of the domain wall is dominated by the uniaxial magnetic anisotropy term proportional to $\cos^2 \theta = z^2$. In fig. 5.9 the energy differences obtained between the helical wall configuration and the ground-state cycloidal wall configuration are plotted as a function of the stretching factor (diamonds). The uniaxial anisotropy of the central atom, $-\frac{3}{4}\sqrt{\frac{5}{\pi}}K_2^0$, is also plotted (circles). The values of ΔE from the two calculations agree well for $x \geq 0.95$, while for more squeezed contacts the uniaxial anisotropy of the central atom overestimates the energy difference between the different types of domain walls. The anisotropy of the orbital moment of the central atom, i.e., the difference in the orbital moment between the cycloidal and the helical wall is also plotted in fig. 5.9 ($\times$ signs). The orbital moment anisotropy shows strong correlation with the anisotropy energies. The ratio of the uniaxial anisotropy constant and the orbital moment anisotropy is presented in tab. 5.3. The correlation is not surprising since the magnetic anisotropy energy and the anisotropy of the orbital moment show the same angular dependence in the perturbative theory of the SOC. [12] In monolayers this ratio is in the order of $\frac{1}{4}\xi$, with ξ being the spin-orbit constant in the order of $0.05 \, \mathrm{eV}$. [12]

Table 5.3   The ratio of the uniaxial anisotropy energy term of the central atom, K_2^0, and the anisotropy of the orbital moment of the central atom as a function of the stretching. (In meV/μ_B units.)

x	0.85	0.90	0.95	1.00	1.05	1.10	1.15
$\dfrac{-\frac{3}{4}\sqrt{\frac{5}{\pi}}K_2^0}{\mu_\mathrm{CW}^\mathrm{orb} - \mu_\mathrm{HW}^\mathrm{orb}}$	27.08	25.64	27.37	28.82	31.74	35.43	38.90

5.2.6   Summary

It can be concluded that the main driving force of the formation of a cycloidal domain wall is a giant uniaxial on-site magnetic anisotropy at the central atom: In the cycloidal wall the magnetic moment of the central atom is parallel to the easy axis, while in the helical wall configuration it lies within the hard plane. The obtained ground state, the cycloidal domain wall, remains stable against squeezing or stretching the contact along the normal-to-plane direction. A huge enhancement, as well as anisotropy of the orbital moment, is found at the central site of the contact.
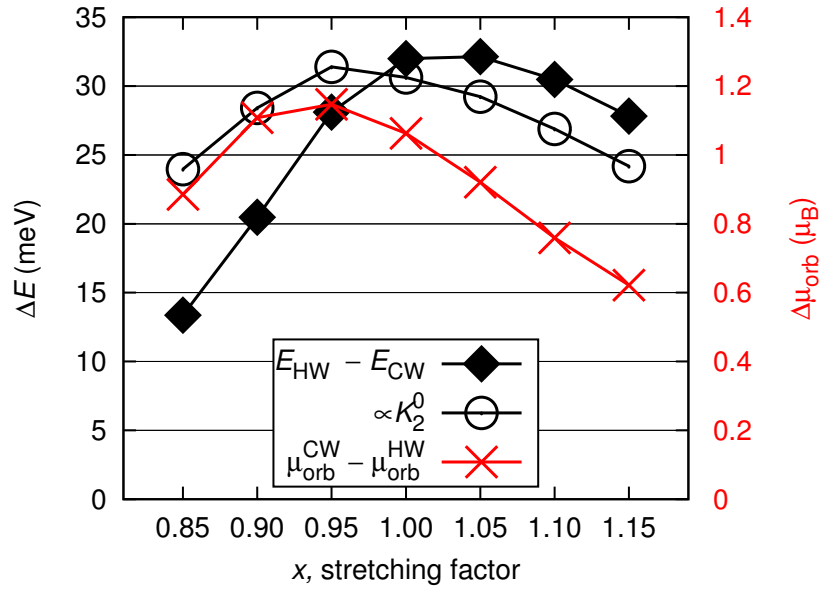
Figure 5.9 Diamonds: Calculated energy differences between the helical and cycloidal domain walls, $E_{\mathrm{HW}} - E_{\mathrm{CW}}$; circles: on-site uniaxial magnetic anisotropy energy of the central atom (see text); red $\times$ signs: orbital moment anisotropy of the central atom, $\mu_{\mathrm{CW}}^{\mathrm{orb}} - \mu_{\mathrm{HW}}^{\mathrm{orb}}$, as a function of the stretching parameter, x.

5.3   Frustrated Cr nanostructures on Au(111)

After presenting the ferromagnetic clusters in the last two sections, in this section antiferro-magnetic Cr structures on the (111) surface of Au are presented which show frustration due to the triangular arrangement. There are four different positions for a compact trimer on the fcc (111) surface as is explained in Subsection 5.3.1. In Subsection 5.3.2 the Dzyaloshinsky–Moriya interaction and other anisotropy terms are discussed in the framework of a second order Heisenberg spin model with special attention to the chirality of the trimers. The model parameters are determined by the fully relativistic EC-KKR method. (Subsection 4.1.8) In the last subsection (Subsection 5.3.3) the same questions are discussed for the fcc and hcp stacked Cr monolayers on the Au (111) surface.

5.3.1   The geometry of the fcc(111) surface

The high symmetry adsorption sites of a fcc(111) surface are the fcc hollow, the hcp hollow, the bridge and the on-top sites, see fig. 5.10. By labelling the in-equivalent layers of the fcc lattice along the [111] direction with capital letters, the order of the fcc stacking is
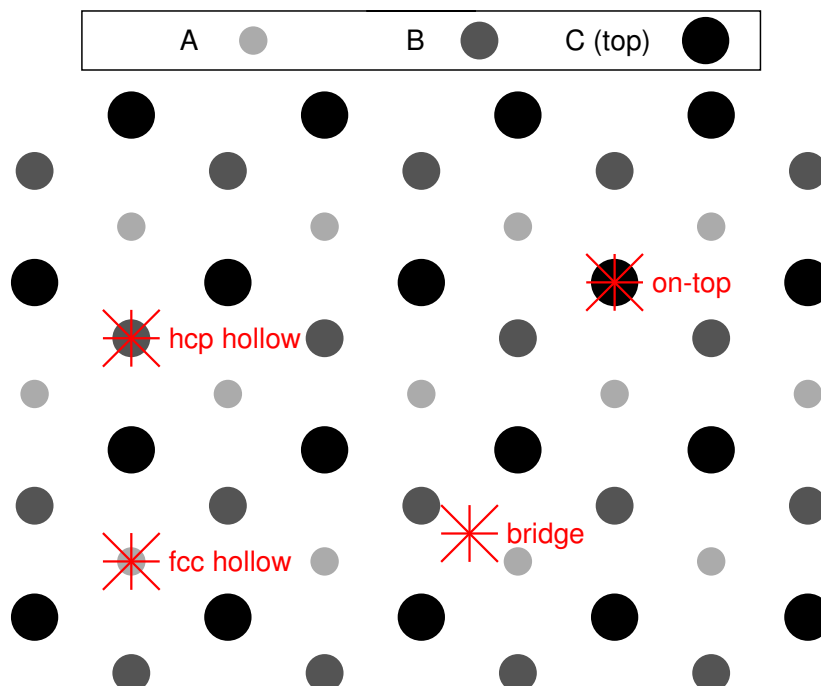
Figure 5.10   The (111) surface of a fcc lattice and the high symmetry adsorption sites viewed from above. The layers of the lattice are depicted as black (C), dark gray (B) and light gray (A) circles, from the top layer towards the deeper layers, respectively. The *bridge* sites are between two sites of the top layer. The *on-top, hcp hollow* and *fcc hollow* sites can be labelled as ABCABC**C**, ABCABC**B** and ABCABC**A** stackings, respectively.

(a) Fcc up, $\kappa^z = +1$.

(b) Fcc down, $\kappa^z = -1$.

(c) Hcp up, $\kappa^z = -1$.

(d) Hcp down, $\kappa^z = +1$.
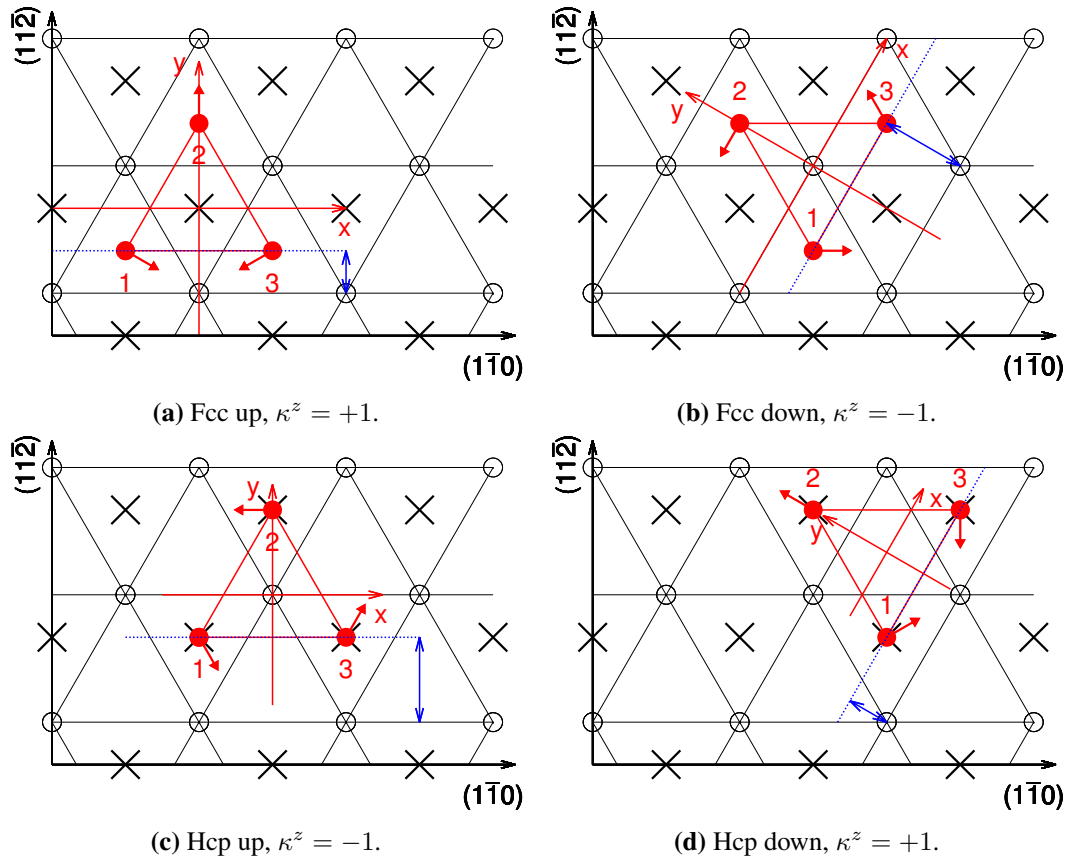
Figure 5.11 Top view of the fcc(111) supporter and the deposited trimers. The atomic positions in the first (second) layer are marked with the lattice of empty circles ($\times$ signs). The positions of the ad-atoms are displayed as filled red circles. The blue double arrows mark the two different lateral displacements between the trimers and the atomic rows of the supporter measuring towards the base of the trimers. For the symmetry analysis of the interaction matrices we use local coordinate systems as displayed in red colour. The ground state magnetic configurations are drawn by the thick red arrows. The indicated chiralities in the sub-captions refer to the (1.5) definition.

ABCABC**A**, while the order for the hcp stacking is ABCABC**B**, where the last (boldface) symbol corresponds to the deposited layer.

We note that in the experiments by examining the topography of the supporter surface and the ad-atoms it is not easy to distinguish between the fcc or hcp stacking. This is because the measured images show the top layer (C) and the ad-atom positions which differ from the C sites but whether they are above the A or above the B layer is not clear. A possible solution is to find a step edge of the supporter close to the ad-island and there the second layer (B) become visible and the stacking of the ad-island is decidable. For an example see the work of Gao *et al.* [34] Later on, we consider fcc hollow and hcp hollow sites of Au(111) surface for the equilateral Cr trimer or full Cr monolayers.

5.3.2 Trimers

There are two different hollow adsorption site of the fcc(111) surface, however, equilateral triangles of adjacent adsorption sites can be placed in four different configurations as it is shown in fig. 5.11. Fcc and hcp stacked compact trimers both can be either *up* or *down*

triangles. (See fig. 5.11.) One attribute to characterize the triangles (by using only the position of them with respect to the top layer of the supporter) is the lateral displacement between the supporter atomic rows and the base of the triangle as it is indicated by the blue double arrows in fig. 5.11. It can be $\frac{\sqrt{3}}{6}a_{2D}$ (for fcc up and for hcp down trimers) or $\frac{\sqrt{3}}{3}a_{2D}$ (for hcp up and for fcc down trimers) where a_{2D} is the two-dimensional lattice constant, i.e., the nearest atom-atom distance in the crystal. Note, that one cannot distinguish between an fcc up and an hcp down island (fcc down and hcp up) if one only sees the island itself and the topmost supporter layer which is the situation in a constant current non-magnetic STM experiment. The four clusters are, however, different: the Cr atoms in an fcc up or an hcp down cluster surround an interstice in the first supporter layer (*breezy* triangle) while in an fcc down or an hcp up cluster they surround a substrate atom (*crammed* triangle). STM images of triangular fcc up and hcp down islands (much larger than a trimer, of course) and schematic illustration of all the four possible islands are presented in fig. 2. of ref. 34.

Previous studies on Cr clusters forming equilateral triangle considered the fcc up trimer [15, 38, 39, 42] and, according to my knowledge, magnetic properties of the other compact Cr trimers have not been investigated yet.

In this work, I neglected possible relaxations of the geometry, i.e., Cr atoms occupied hollow positions above the topmost Au layer with the 2D lattice constant of gold ($a_{2D} =$ 2.874 Å). The layer-layer distances of bulk gold was applied as the distance between the top gold layer and the plane of the chromium ad-atoms.

In the case of the trimers the spin moments of the Cr atoms scattered between 4.18 μ_B and 4.22 μ_B while the orbital moments between 0.021 μ_B and 0.038 μ_B depending on the geometry and the magnetic structure. These values are in good agreement with the results of previous studies: 3.15 μ_B/atom if geometrical relaxation is included [38]; 4.25 μ_B/atom [39] and 4.4 μ_B/atom [15] if it is neglected. For the orbital moment also small values have been reported: ≤ 0.036 μ_B/atom with geometrical relaxation included [38] and ≈ 0.03 μ_B/atom [15] without relaxation.

The trimers with fcc and hcp stacking together with the substrate exhibit a C_{3v} point group symmetry where the C_3 axis intersects the centre of the triangle normal to the substrate and the reflection planes contain the C_3 axis and one of the cluster atom. The C_{3v} point group symmetry prescribes relations between the parameters of the spin-Hamiltonian (1.1). The derivation is given in Appendix B and the complete list of the exchange coupling matrices and the anisotropy matrices with an unrelated parameter set is given as eqs. (B.9)–(B.14).

The derivation of the rotational energies in the framework of the Heisenberg model is also given in Appendix B and the complete formulas are found in eqs. (B.20)–(B.22). For the rotations around the three fold axis the energy has the form of

$$E_z^+(\varphi) = E_{0z}, \tag{5.7}$$

$$E_z^-(\varphi) = E_{0z} - 3\sqrt{3}D^z + 3(S^{\varphi\varphi} + K^{\varphi\varphi})\cos(2\varphi), \tag{5.8}$$

where E_{0z} is an energy independent on the angle of rotation and the $\pm$ superscripts indicate whether a configuration with positive or negative chirality is rotated rigidly around the axis. Similarly, when the configuration is rotated around the axis parallel to the magnetization at the 2$^{\text{nd}}$ Cr atom (see fig. 5.11) the energy can be given as:

$$E_y^\pm(\vartheta) = E_{0y} \pm \left[\frac{3\sqrt{3}}{2}D^z - \frac{3}{2}(S^{\varphi\varphi} + K^{\varphi\varphi})\right]\cos(\vartheta)$$

$$+ \left[\frac{3}{8}(S^{\varphi\varphi} + K^{\varphi\varphi}) + \frac{9}{16}(S^{zz} - 2K^{zz})\right]\cos(2\vartheta). \qquad (5.9)$$

The $\pm$ superscript indicates here the chirality at $\vartheta = 0$. Note, that the rotation around the y axis reverses the chirality but the rotation around the z axis does not alter the chirality.

By comparing these rotational energy functions to the results of the first principles calculations the values of the coefficients of the trigonometric functions can be extracted. From equation (5.9) the energy difference between the positive and the negative chirality configuration can be read off:

$$\Delta E = E_y^+(0) - E_y^-(0) = 3\sqrt{3}D^z - 3(S^{\varphi\varphi} + K^{\varphi\varphi}). \qquad (5.10)$$

Since the relative angle between the spins does not change during the global spin rotations, the contribution of the isotropic exchange cancel out and the J parameter of the model is not accessible through the $E_z^\pm(\varphi)$ and $E_y^\pm(\vartheta)$ functions. Regarding the focus of the recent work, the factual value of the isotropic exchange is, therefore, irrelevant. Furthermore, we note that the rotational invariant fourth order terms introduced by Antal *et al.* [15] neither contribute to the rotational energy.

The rotational energies are calculated with a resolution of 3° for all four trimers and the results are shown in figure 5.12. The parameters in equations (5.8) and (5.9) are obtained as the Fourier components of the rotational energies and listed in table 5.4. Using these parameters the functions given by equations (5.8) and (5.9) fit with a high accuracy to the results provided by the ab-initio calculations.

From fig. 5.12 and tab. 5.4 it can be inferred that the energy minimum corresponds to $\kappa^z = +1$ for the fcc up and hcp down trimers while to $\kappa^z = -1$ for the fcc down and hcp up trimers. The minimal energy configurations are visualized in fig. 5.11. Note, however, that in case of the fcc up trimer the energy difference between the two chiral states is found to be $-18 \ \mu$eV which is near the computational accuracy of our method.

In the case of the $\kappa^z = -1$, the relative orientation of the magnetization vector and the easy direction set by the on-site anisotropy term ($\mathbf{K}_i$) is the same for the three Cr atoms and this situation is preserved during the global in-plane rotation, therefore, the anisotropy energies of the single atoms are simply summed up. The same argument holds for the two-site anisotropies ($\mathbf{J}_{ij}^{\text{S}}$), thus, as indicated by equation (5.8), we expect a $\cos(2\varphi)$ angular dependence for the in-plane rotational energy. This is clearly confirmed by the first principles calculations, see the lower graph of figure 5.12.
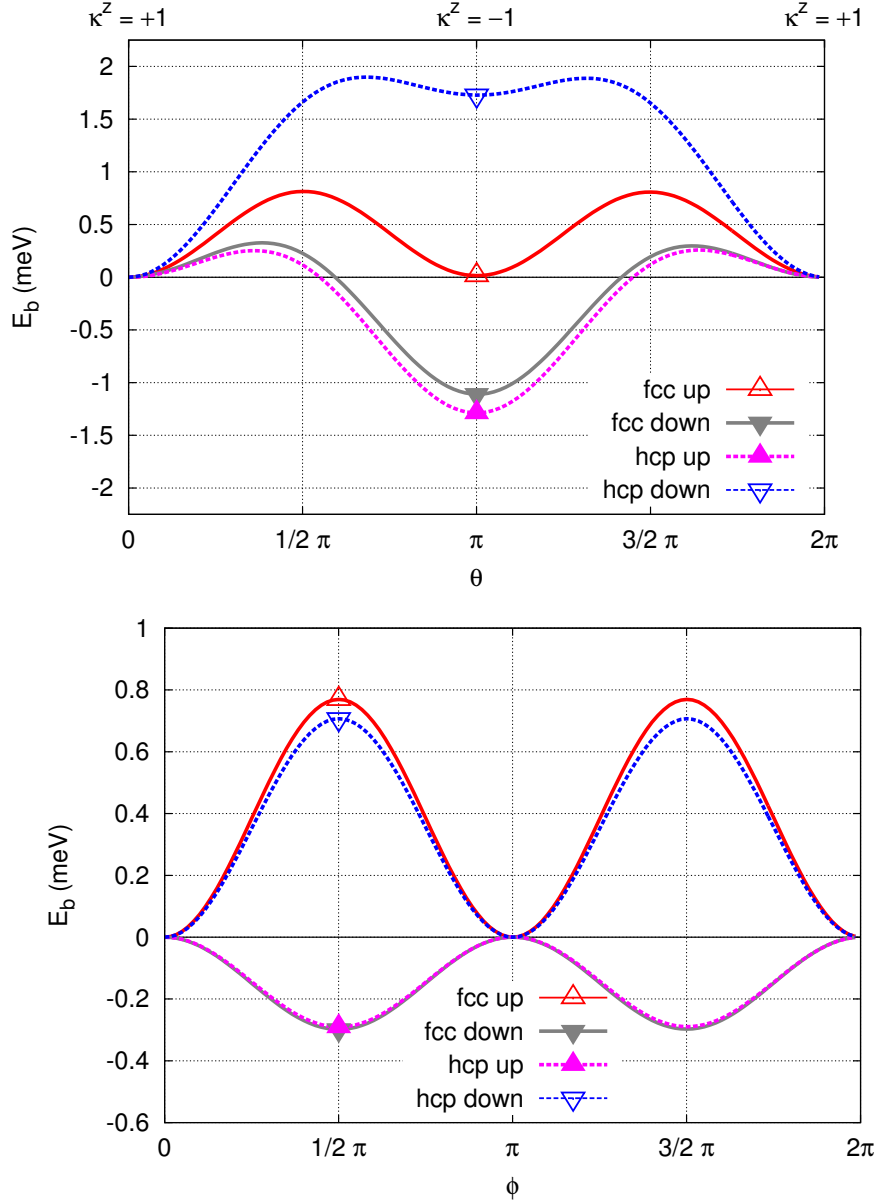
Figure 5.12 Rotational energy of the trimers, $E_y^+(\vartheta)$ (upper graph) and $E_z^-(\varphi)$ (lower graph). The symbols refer to the trimer geometries shown in figure 5.11. The points forming the lines were calculated with a resolution of 3°. The κ^z component of the chirality vector is indicated above the upper graph and we note that a global rotation about the z axis (lower graph) does not alter the chirality. The energy curves are shifted to zero at the initial configuration, $\vartheta = 0$ or $\varphi = 0$.

Table 5.4 Fitted spin-model parameters entering eqs. (5.8) and (5.9) together with the energy difference between the two chiral states, $\Delta E = E_y^+(0) - E_y^-(0)$, for the four different trimers and the two monolayers (ML). The values are given in units of meV. With gray background I also indicate the results originated from the less fine resolution BZ-integral.

Trimer/ML	$S^{\varphi\varphi} + K^{\varphi\varphi}$	D^z	$S^{zz} - 2K^{zz}$	ΔE
fcc up	-0.128	-0.077	-0.629	-0.018
	-0.131	-0.078	-0.632	-0.009
fcc down	0.050	0.242	-0.714	$+1.110$
	0.048	0.237	-0.719	$+1.086$
hcp up	0.048	0.276	-0.711	$+1.288$
	0.046	0.270	-0.715	$+1.263$
hcp down	-0.118	-0.401	-0.625	-1.730
	-0.121	-0.401	-0.628	-1.722
fcc ML	$< 1. \, \mu$eV	-1.086	-0.469	-5.643
hcp ML	$< 1. \, \mu$eV	2.972	-0.482	$+15.444$

For the in-plane rotational energy of the $\kappa^z = +1$ trimers we expect the anisotropy terms to cancel since the second order in-plane anisotropy energies are sampled at angles $\varphi_1 = \varphi$, $\varphi_2 = 120° + \varphi$, and $\varphi_3 = 240° + \varphi$, for which $\sum_{i=1}^{3} \cos^2 \varphi_i = \frac{3}{2}$, i.e., independent of the angle of rotation. The magnitude of the rotational energies of the positive chirality trimers was indeed found below 7 μeV, indicating a very small deviation between the spin model (1.1) and the *ab initio* calculation. Similarly, Szunyogh *et al.* [75] found a $\cos(2\varphi)$ angular dependence of the rotational energy of IrMn$_3$ with an amplitude of 10.42 meV in the so-called $T1$ state with negative chirality, while for the states with positive chirality the rotational energy had no angular dependence up to an absolute error of 2 μeV.

It can be read off from tab. 5.4 that the trimers with similar environment, i.e., the breezy and the crammed triangles, exhibit similar parameter values. This is, in particular, valid for the out-of-plane and in-plane anisotropy parameters, $S^{zz} - 2K^{zz}$ and $S^{\varphi\varphi} + K^{\varphi\varphi}$, respectively. The z component of the DM vector turned out to be similar for the fcc down and the hcp up (crammed) trimers, but D^z for the fcc up and the hcp down (breezy) trimers are rather different. I notice that for an fcc up trimer Antal *et al.* [15] reported a value of $D^z = 0.97$ meV which is a remarkable difference compared to my present value of $D^z = -0.077$ meV. There are, however, distinct differences between the two calculations. Here I included one shell of environment around the atoms forming the trimer, whereas in ref. 15 only the Cr atoms were taken into account in the self-consistent calculations. On the the other hand, I calculated the rotational energies in terms of the Lloyd formula, eq. (4.56), while Antal *et al.* [15] used eq. (4.55) to evaluate the band-energy.

I repeated the magnetic force theorem calculations of the rotational energies by using the self-consistent effective potentials and fields from the higher energy chirality configurations and found that the lowest energy configurations do not change.   Remarkably, how-

(a) Fcc stackig, $\kappa^z = +1$.   **(b)** Fcc stacking, $\kappa^z = -1$.
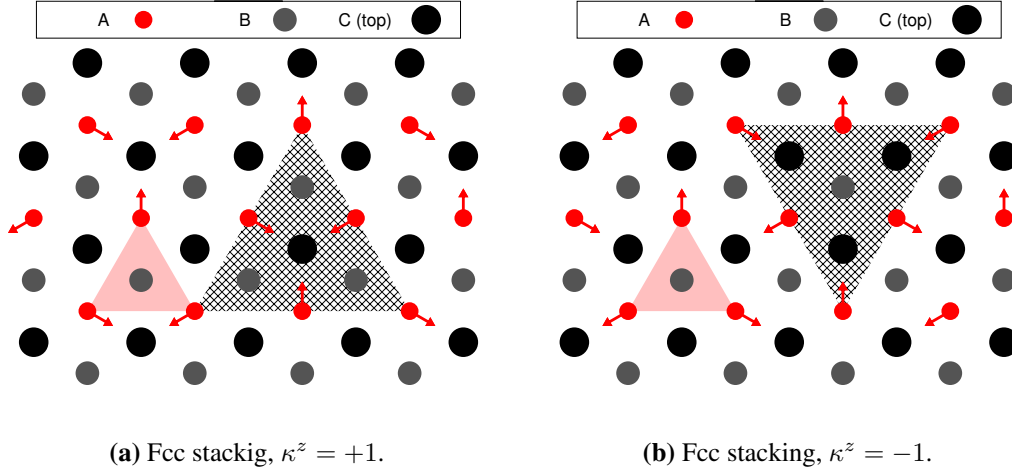
Figure 5.13   Illustration of the (a) positive and the (b) negative chirality Néel state of the triangular lattice. The fcc stacking (ABCABC**A**) is presented as an example. The first and the second layer of the lattice is depicted as black (C) and dark gray (B) circles, and the deposited magnetic layer as red circles (A) with arrows representing their magnetization direction. The *up* elementary triangle of the monolayer is highlighted by the red triangle. (a) An up island and (b) a down islad are also illustrated as shaded triangles.

ever, Stocks *et al.* [42] found a change of sign in $\Delta E = E_y^+(0) - E_y^-(0)$ if they used the negative chirality Néel state ($\Delta E = +7$ meV) or the out-of-plane ferromagnetic state ($\Delta E = -4$ meV) for the self-consistent reference potential and field calculation.

Regarding the in-plane anisotropy (see the lower graph of figure 5.12), for the fcc up and hcp down trimers I found a value of $S^{\varphi\varphi} + K^{\varphi\varphi}$ which is about 50 % larger in magnitude as compared to the fcc up trimer calculations of Stocks *et al.* [42]. The reason for this difference is the same as mentioned above in context to D^z. In the case of fcc down and hcp up trimers, the reversed (positive) value of $S^{\varphi\varphi} + K^{\varphi\varphi}$ means that the ground state of these trimers is rotated by 90° with respect to the conventional, high symmetry directions of the Néel state, see figs. 5.11(b) and 5.11(c). Similarly, Gao *et al.* [34] found that triangular Mn islands of different stackings exhibit different easy directions inside the 120° Néel structure.

5.3.3   Mono-layers

In the case of the deposited monolayers the distance between the host and the deposited layer was also kept equal to the layer–layer distance of the bulk supporter crystal.

For both fcc and hcp stacked mono-layers I obtained a spin magnetic moment of $3.70 \, \mu_B$ and an orbital magnetic moment of $0.02 \, \mu_B$ for the Cr atoms.

For the mono-layers with fcc and hcp stacking the C_{3v} point group symmetry also holds with C_3 axes intersecting the centre of an elementary triangle or a Cr atom. Note that the mono-layers contain alternating up and down elementary triangles. The two types of triangles are in-equivalent, i.e., one type of triangle can not be transformed into the other type by any of the symmetry operations of the system.

In the case of an in-plane Néel spin structure of a mono-layer, the chirality for the up and down triangles alternates between the values of $+1$ or -1. In this case, the *chirality of*

the mono-layer is associated with the *chirality of the up triangles*. The energy of the Néel structures with opposite chiralities may be different due to the non-vanishing z component of the DM vector. The two different chirality Néel states with the defining up triangles (red triangles in the figure) are illustrated in fig. 5.13.

Conversely, the above definition might not fit to the experiments because it is the breeziness of the trimers or islands which is identifiable in a topographic STM experiment not the up/down property. It might be better to connect the chirality definition of the monolayer to the breeziness of the elementary triangles. Despite that idea, I use the first definition of the chirality of a monolayer spin structure through this dissertation.

For mono-layers, the coupling between the sub-lattices p and q, $\mathbf{J}_{pq}$, is defined as the sum of the corresponding exchange tensors, see eq. (B.25). If all the sites are located in the same sub-lattice, $\mathbf{J}_{pp}$ will contribute to the $\mathbf{K}$ anisotropy matrix, which will be the same for all sub-lattices. Due to the symmetry of the mono-layer, it turns out that the terms K^{yz}, $K^{\varphi\varphi}$, S^{yz}, $S^{\varphi\varphi}$ and D^y disappear from the spin model. For the details see Appendix B. The rotational energy of the monolayer is given in eqs. (B.33) and (B.34).

The band energies while rotating the magnetic configuration around the axis lying in the plane of the mono-layer are shown in fig. 5.14. Using the parameters in tab. 5.4 the results of the first principles calculations can be fitted with a high accuracy by the function given in eq. (B.34).

Corresponding to eq. (B.33) the band energy turned out to be practically independent on the angle of rotation around the C_3 axis, $S^{\varphi\varphi} + K^{\varphi\varphi} < 1$ μeV. Note that Szunyogh *et al.* found non-vanishing in-plane anisotropy parameters for the (111) layers in bulk $IrMn_3$ [75] or at the $IrMn_3/Co$ interface [76] since for these systems the above symmetry does not apply.

Fitting the out-of-plane rotational energy in fig. 5.14 to eq. (B.34), I obtain nearly the same $S^{zz} - 2K^{zz}$ parameters for the fcc and hcp mono-layers, see tab. 5.4. These parameters are somewhat reduced in magnitude as compared to those for the trimers. As obvious from the nearly $\cos\vartheta$-like dependence of the band-energy curves in figure 5.14, the out-of-plane rotational energies are dominated by the normal-to-plane components of the DM interactions and D^z is opposite in sign for the fcc and the hcp mono-layers. Note that for the mono-layer case D^z is the only interaction which distinguishes between the two Néel states with opposite chiralities.

The D^z parameters are almost an order larger in magnitude for the mono-layers than for the trimers, see table 5.4. This can be understood due to the following reasoning. The main contribution to the DM interactions is due to the nearest Cr neighbours. Since in the case of mono-layers the number of nearest neighbours is three times larger then those in the trimers, a corresponding enhancement of D^z is expected. More quantitatively, the magnetic unit cell of the mono-layers is composed of 3 up and 3 down elementary trimers. Hence, a first estimation of the energy difference between the two chirality states of the mono-layer could be 3 times the sum of the energy differences of the trimers. (It should be recalled that the chirality index of the up and down trimers are opposite in a mono-layer, therefore, the chiral energy of the down trimer should be subtracted from that of the up trimer.) From the data of table 5.4 we
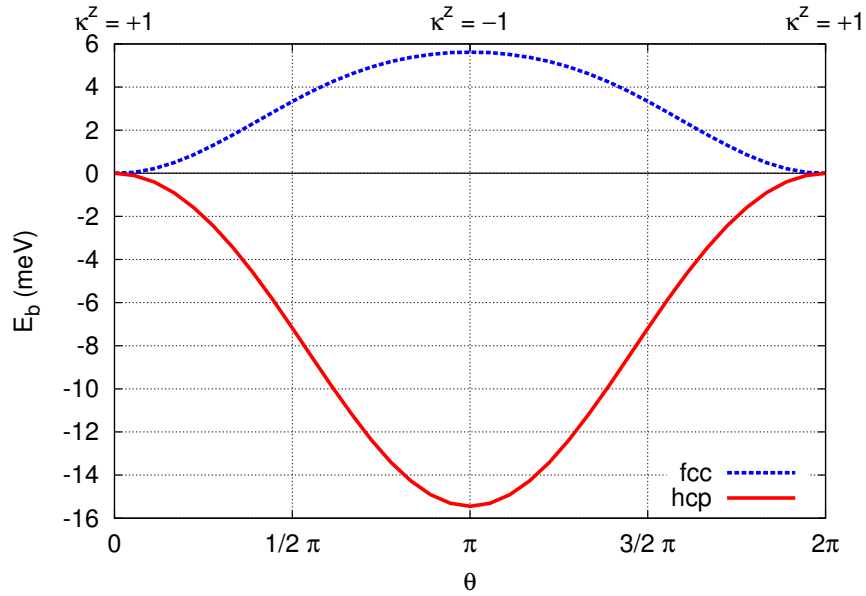
Figure 5.14   Rotational energy of the mono-layers about the y axis, $E_y^+(\vartheta)$. The lines were calculated with a resolution of $10°$. The κ^z component of the chirality vector is indicated above the graph. The energy curves are shifted to zero at the initial configuration, $\vartheta = 0$.

calculate $\Delta E_{\mathrm{ML}}/\left(\Delta E_{\mathrm{up}} - \Delta E_{\mathrm{down}}\right) = 5.003$ for the fcc mono-layer and 5.118 for the hcp mono-layer. The large deviation of these values from 3 indicates that the spin-interactions in a mono-layer are rather different from those in the trimers and/or interactions between more distant pairs have important contributions.

Chapter 6

Concluding remarks

In this thesis 3d transition metal clusters deposited onto magnetic or non-magnetic substrate were investigated by first principles numerical calculations.

It is emphasized that the geomety of the clusters influences the magnetic behaviour. The disclosure of the regularities of these influences is an open topic. The magnetic anisotropy energy of a Co nanocontact show a strong dependence on the stretching of the contact. The Dzyaloshinsky–Moriya (DM) interaction in Cr trimers turn out to depend intriguingly on the stacking of the cluster on the substrate. Through the DM interaction and the pseudo-dipolar coupling the ground state chirality is also a consequence on the geometry. A novel study of Błoński *et al.* [104], however, reveals the reverse effect: for Ni clusters "the change in the magnetic symmetry leads to small geometric distortions of the cluster".

The other subject of this thesis is to relate the results of the *ab initio* calculation to a classical Heisenberg model. A 4×4 Co cluster is used as an example to demonstrate, that the spin model based Monte Carlo simulation can reach the accuracy of the *ab initio* based Monte Carlo simulation. Two different methods, the torque method and the rotational energy method, are demonstrated in the case of the Co nanocontact and the Cr clusters to determine the spin model parameters. In general, however, it is not clear which higher order terms are to be included into the spin model to reproduce an accurate description of a magnetic nanostructure. [15]

Appendix A

Elements of the relativistic quantum theory

Dirac matrices

The well-known Pauli matrices:

$$\sigma_x = \begin{pmatrix} 0 & 1 \\ 1 & 0 \end{pmatrix}, \qquad \sigma_y = \begin{pmatrix} 0 & -i \\ i & 0 \end{pmatrix}, \qquad \sigma_z = \begin{pmatrix} 1 & 0 \\ 0 & -1 \end{pmatrix}. \tag{A.1}$$

A vector is usually composed of them:

$$\boldsymbol{\sigma} = \begin{pmatrix} \sigma_x, & \sigma_y, & \sigma_z \end{pmatrix}. \tag{A.2}$$

The 4 by 4 Dirac matrices in a 2 by 2 supermatrix notation:

$$\alpha_i = \begin{pmatrix} \mathbf{0} & \sigma_i \\ \sigma_i & \mathbf{0} \end{pmatrix}, \qquad \beta = \begin{pmatrix} \mathbb{1} & \mathbf{0} \\ \mathbf{0} & -\mathbb{1} \end{pmatrix}, \qquad \Sigma_i = \begin{pmatrix} \sigma_i & \mathbf{0} \\ \mathbf{0} & \sigma_i \end{pmatrix} \qquad \text{for } i \in \{x, y, z\} \tag{A.3}$$

and vectors:

$$\boldsymbol{\alpha} = \begin{pmatrix} \alpha_x, & \alpha_y, & \alpha_z \end{pmatrix}, \qquad \boldsymbol{\Sigma} = \begin{pmatrix} \Sigma_x, & \Sigma_y, & \Sigma_z \end{pmatrix}. \tag{A.4}$$

Let us introduce

$$\sigma_r = \hat{\mathbf{r}} \cdot \boldsymbol{\sigma} = \frac{\mathbf{r}}{r} \cdot \boldsymbol{\sigma} \qquad \text{and} \qquad \alpha_r = \hat{\mathbf{r}} \cdot \boldsymbol{\alpha} = \begin{pmatrix} \mathbf{0} & \sigma_r \\ \sigma_r & \mathbf{0} \end{pmatrix} \tag{A.5}$$

with the position operator, $\mathbf{r}$.

A useful identity of the Pauli matrices with arbitrary vectors $\mathbf{A}$ and $\mathbf{B}$:

$$(\boldsymbol{\sigma} \cdot \mathbf{A})(\boldsymbol{\sigma} \cdot \mathbf{B}) = \mathbf{A} \cdot \mathbf{B} + i\boldsymbol{\sigma} \cdot (\mathbf{A} \times \mathbf{B}). \tag{A.6}$$

Appying this to $\mathbf{A} = \hat{\mathbf{r}}$ and $\mathbf{B} = \mathbf{L} = \mathbf{r} \times \mathbf{p}$ one gets:

$$\boldsymbol{\sigma} \cdot (\hat{\mathbf{r}} \times \mathbf{L}) = -\mathrm{i}\sigma_r \left(\boldsymbol{\sigma} \cdot \mathbf{L}\right). \tag{A.7}$$

Addition of two angular momentum operators: $\mathbf{J} = \mathbf{J}_1 + \mathbf{J}_2$

$\mathbf{J}_1$ and $\mathbf{J}_2$ are two vector angular momentum operators acting on a $(2\ell_1{+}1)$ and on a $(2\ell_2{+}1)$-dimensional Hilbert spaces, respectively. The total angular momentum operator, $\mathbf{J}$, acts on the tensor product space as:

$$J^i = J_1^i \otimes \mathbb{1} + \mathbb{1} \otimes J_2^i \qquad \text{for } i \in \{x, y, z\}. \tag{A.8}$$

The uncoupled basis of the tensor product space is:

$$|\ell_1, m_1\rangle \otimes |\ell_2, m_2\rangle \tag{A.9}$$

with $m_1 = -\ell_1, \ldots, \ell_1$ and $m_2 = -\ell_2, \ldots, \ell_2$. In the coupled representation the basis, $|j, \mu\rangle$, is the common eigenfunctions of $\mathbf{J}^2$ and J^z:

$$\mathbf{J}^2 |j, \mu\rangle = \hbar^2 j(j+1) |j, \mu\rangle \qquad \text{and} \qquad J^z |j, \mu\rangle = \hbar\mu |j, \mu\rangle. \tag{A.10}$$

The coupled representation can be produced by the Clebsch–Gordan coefficients from the decoupled representation as

$$|j, \mu\rangle = \sum_{m_1=-\ell_1}^{\ell_1} \sum_{m_2=-\ell_2}^{\ell_2} C(\ell_1, \ell_2, j; m_1, m_2, \mu) |\ell_1, m_1\rangle \otimes |\ell_2, m_2\rangle. \tag{A.11}$$

For the length of the total angular momentum vector, j, the triangular relation holds:

$$|\ell_1 - \ell_2| \le j \le \ell_1 + \ell_2. \tag{A.12}$$

Since $|\ell_1, m_1\rangle \otimes |\ell_2, m_2\rangle$ is an eigenfunction of $J^z = J_1^z \otimes \mathbb{1} + \mathbb{1} \otimes J_2^z$ with the eigenvalue of $m_1 + m_2$ and the basis functions in eq. (A.11) are linearly independent therefore $C(\ell_1, \ell_2, j; m_1, m_2, \mu)$ is nonzero only if $\mu = m_1 + m_2$. Exploiting this restriction one single sum in eq. (A.11) is sufficient:

$$|j, \mu\rangle = \sum_{m_2=-\ell_2}^{\ell_2} C(\ell_1, \ell_2, j; \mu - m_2, m_2, \mu) |\ell_1, m_1\rangle \otimes |\ell_2, m_2\rangle. \tag{A.13}$$

Addition of the orbital and the spin-angular momentum: $\mathbf{J} = \mathbf{L} + \mathbf{S}$

The eigenfunctions of $\mathbf{L}$ are:

$$Y_{\ell,m}(\hat{\mathbf{r}}) \tag{A.14}$$

and the eigenfunctions of $\mathbf{S}$ are Φ_s as:

$$\Phi_{\frac{1}{2}} = \begin{pmatrix} 1 \\ 0 \end{pmatrix} \qquad \text{and} \qquad \Phi_{-\frac{1}{2}} = \begin{pmatrix} 0 \\ 1 \end{pmatrix}. \tag{A.15}$$

The triangular relation, eq. (A.12), in this case reads:

$$\left| \ell - \tfrac{1}{2} \right| \leq j \leq \ell + \tfrac{1}{2}. \tag{A.16}$$

Which means:

$$j = \begin{cases} \ell \pm \tfrac{1}{2} & \text{if } \ell > 0, \\ \ell + \tfrac{1}{2} & \text{if } \ell = 0. \end{cases} \tag{A.17}$$

Taking into account the $\mu = m + s$ restriction in the $C(\ell, \tfrac{1}{2}, j; m, s, \mu)$ Clebsch–Gordan coefficients the uncoupled basis of the total angular momentum can be produced as:

$$\psi_{j,\mu}(\hat{\mathbf{r}}) = \sum_{s=\pm\frac{1}{2}} C(\ell, \tfrac{1}{2}, j; \mu - s, s, \mu) Y_{\ell,\mu-s}(\hat{\mathbf{r}}) \Phi_s. \tag{A.18}$$

Let us define the K operator as

$$K = \mathbf{L} \cdot \boldsymbol{\sigma} + \hbar \tag{A.19}$$

with $\boldsymbol{\sigma}$ being the vector composed of the Pauli matrices (see eq. (A.2)) and note that the spin operator is: $\mathbf{S} = \frac{\hbar}{2}\boldsymbol{\sigma}$.

It can be derived that $\psi_{j,\mu}(\hat{\mathbf{r}})$ is an eigenfunction of K with eigenvalue

$$\hbar\left(\left(j + \tfrac{1}{2}\right)^2 - \ell(\ell+1) \right) \tag{A.20}$$

which is defined as $-\hbar\kappa$. Using this definition and eq. (A.17) κ can be given:

$$\kappa = \begin{cases} \ell & \text{for } j = \ell - \tfrac{1}{2}, \\ -\ell - 1 & \text{for } j = \ell + \tfrac{1}{2}. \end{cases} \tag{A.21}$$

Note that κ can be any integer except zero. It is important that both j and ℓ is a function of κ:

$$j = |\kappa| - \tfrac{1}{2} \qquad \text{and} \qquad \ell = \begin{cases} \kappa & \text{for } \kappa > 0, \\ -\kappa - 1 & \text{for } \kappa < 0. \end{cases} \tag{A.22}$$

The $\kappa\mu$-representation

Taking advantage of the fact that the value of κ gives both j and l, the spin spherical harmonics, $\chi_{\kappa,\mu}(\hat{\mathbf{r}})$, are defined as:

$$\chi_{\kappa,\mu}(\hat{\mathbf{r}}) = \sum_{s=\pm\frac{1}{2}} C(\ell, \tfrac{1}{2}, j; \mu-s, s, \mu) Y_{\ell,\mu-s}(\hat{\mathbf{r}})\Phi_s, \tag{A.23}$$

where ℓ and j on the right hand side are given by κ through eq. (A.22).

Let us summarize here that the $\chi_{\kappa,\mu}(\hat{\mathbf{r}})$ are common eigenfunctions of the total angular momentum, $\mathbf{J}^2$, its z component, J^z, and the K-operator:

$$\mathbf{J}^2 \chi_{\kappa,\mu}(\hat{\mathbf{r}}) = \hbar^2 j(j+1)\chi_{\kappa,\mu}(\hat{\mathbf{r}}),$$

$$J^z \chi_{\kappa,\mu}(\hat{\mathbf{r}}) = \hbar\mu\chi_{\kappa,\mu}(\hat{\mathbf{r}}), \tag{A.24}$$

$$K\chi_{\kappa,\mu}(\hat{\mathbf{r}}) = -\hbar\kappa\chi_{\kappa,\mu}(\hat{\mathbf{r}}).$$

Note the following useful property of the spin spherical harmonics:

$$\sigma_r \chi_{\kappa,\mu}(\hat{\mathbf{r}}) = -\chi_{-\kappa,\mu}(\hat{\mathbf{r}}) \tag{A.25}$$

The composite indices, Q and $\bar{Q}$, are introduced:

$$Q \equiv (\kappa, \mu) \qquad \text{and} \qquad \bar{Q} \equiv (-\kappa, \mu) \tag{A.26}$$

and the summation over Q means:

$$\sum_Q \equiv \sum_{\kappa=\dots,-3,-2,-1,1,2,3,\dots} \sum_{\mu=-|\kappa|+\frac{1}{2}}^{|\kappa|-\frac{1}{2}}. \tag{A.27}$$

Often, the ℓ quantum number appears after a $\sum_Q$ operation. In this case, application of eq. (A.22) is implied, implicitly.

Through this thesis, an angular momentum cutoff of $\ell_{\max} = 2$ is used. The remaining (κ, μ) indices in this approximation are summarized in tab. A.1.

Table A.1 List of the (κ, μ) indices up to $\ell_{\mathrm{max}} = 2$. As a result, the dimension of the matrices in the QQ' angular momentum indices is 18×18.

		κ	μ
$\ell = 0$	$j = \ell + \frac{1}{2} = \frac{1}{2}$	-1	$-1/2$
			$1/2$
$\ell = 1$	$j = \ell + \frac{1}{2} = \frac{3}{2}$	-2	$-3/2$
			$-1/2$
			$1/2$
			$3/2$
	$j = \ell - \frac{1}{2} = \frac{1}{2}$	1	$-1/2$
			$1/2$
$\ell = 2$	$j = \ell + \frac{1}{2} = \frac{5}{2}$	-3	$-5/2$
			$-3/2$
			$-1/2$
			$1/2$
			$3/2$
			$5/2$
	$j = \ell - \frac{1}{2} = \frac{3}{2}$	2	$-3/2$
			$-1/2$
			$1/2$
			$3/2$

Appendix B

Spin models of the C_{3v} symmetric systems

Trimer

In this chapter the manifestation of the C_{3v} symmetry in terms of the second order coupling constants, $\mathbf{J}_{ij}$, and the anisotropy constants, $\mathbf{K}_i$, in a symmetrical trimer will be derived.

The general second order Heisenberg Hamiltonian of the trimer is the following, see eq. (1.1) in the Introduction:

$$\mathcal{H} = \sum_{ij=12,23,31} \boldsymbol{\sigma}_i^{\mathrm{T}} \mathbf{J}_{ij} \boldsymbol{\sigma}_j + \sum_{i=1,2,3} \boldsymbol{\sigma}_i^{\mathrm{T}} \mathbf{K}_i \boldsymbol{\sigma}_i. \tag{B.1}$$

The parametrization for the exchange interaction matrices and the on-site anisotropy matrices is the following:

$$\mathbf{J}_{31} = \frac{1}{3} \begin{pmatrix} J & & \\ & J & \\ & & J \end{pmatrix} + \begin{pmatrix} -\frac{1}{2}S^{zz} + \frac{1}{2}S^{\varphi\varphi} & S^{xy} & S^{zx} \\ S^{xy} & -\frac{1}{2}S^{zz} - \frac{1}{2}S^{\varphi\varphi} & S^{yz} \\ S^{zx} & S^{yz} & S^{zz} \end{pmatrix} + \begin{pmatrix} 0 & D^z & -D^y \\ -D^z & 0 & D^x \\ D^y & -D^x & 0 \end{pmatrix}, \tag{B.2}$$

$$\mathbf{K}_2 = \begin{pmatrix} -\frac{1}{2}K^{zz} + \frac{1}{2}K^{\varphi\varphi} & K^{xy} & K^{zx} \\ K^{xy} & -\frac{1}{2}K^{zz} - \frac{1}{2}K^{\varphi\varphi} & K^{yz} \\ K^{zx} & K^{yz} & K^{zz} \end{pmatrix}. \tag{B.3}$$

$\begin{pmatrix} D^x & D^y & D^z \end{pmatrix}$ form the $\mathbf{D}_{31}$ Dzyaloshinsky–Moriya (DM) vector which corresponds to the antisymmetric interaction term: $\boldsymbol{\sigma}_3^{\mathrm{T}} \mathbf{J}_{31}^{\mathrm{A}} \boldsymbol{\sigma}_1 = \mathbf{D}_{31} (\boldsymbol{\sigma}_3 \times \boldsymbol{\sigma}_1)$ as introduced in the Introduction.

The trimer together with the substrate is symmetric in terms of the C_{3v} point group, see fig. B.1. The parameters in eq. (B.1) will be given in such a way that $\mathcal{H}(\mathcal{G}\{\boldsymbol{\sigma}_i\}) = \mathcal{H}(\{\boldsymbol{\sigma}_i\})$ where $\mathcal{G}$ can be any symmetry operation of the C_{3v} group. The generators of the C_{3v} group are the reflection to the yz plane and the rotation about the z axis by $\frac{2\pi}{3}$. For the sake of
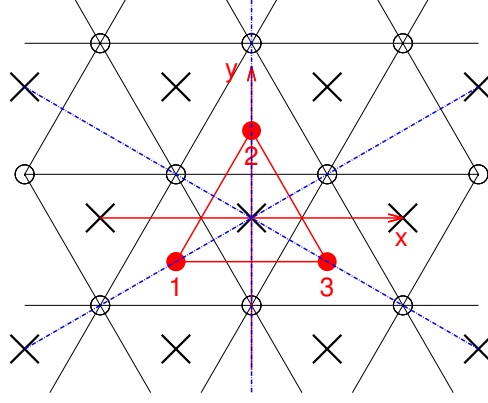
Figure B.1 Example of a C_{3v} symmetric trimer. The σ_v reflection planes are shown as blue dash-dotted lines and the C_3 rotation axis is at the common intersection of the blue lines and it is perpendicular to the plane of the figure. The lattice of empty circles and $\times$ signs denote the positions of the first and second layer of the fcc(111) supporter as in fig. 5.11.

completeness I give the matrices of these transformations:

$$
R^{yz} = \begin{pmatrix} -1 & & \\ & 1 & \\ & & 1 \end{pmatrix} \quad \text{and} \quad C^z_{\frac{2\pi}{3}} = \begin{pmatrix} -\frac{1}{2} & -\frac{\sqrt{3}}{2} & 0 \\ \frac{\sqrt{3}}{2} & -\frac{1}{2} & 0 \\ 0 & 0 & 1 \end{pmatrix}. \tag{B.4}
$$

The 3—1 bond and the atom number 2 are the mirror images of themselves according to the reflection to the yz plane, see fig. B.1, thus

$$
\mathbf{J}_{31} = (R^{yz})^{\mathrm{T}} \mathbf{J}_{31}{}^{\mathrm{T}} R^{yz} \qquad \text{and} \qquad \mathbf{K}_2 = (R^{yz})^{\mathrm{T}} \mathbf{K}_2 R^{yz} \tag{B.5}
$$

hold which yield the following requirements for the matrix elements:

$$
S^{xy} = 0, \qquad S^{zx} = 0, \qquad D^x = 0, \qquad K^{xy} = 0, \qquad K^{zx} = 0. \tag{B.6}
$$

The other exchange interaction matrices and the on-site anisotropy matrices are constructed by similarity transformations out of the $\mathbf{J}_{31}$ and the $\mathbf{K}_2$ matrices:

$$
\mathbf{J}_{23} = C^z_{\frac{2\pi}{3}} \mathbf{J}_{31} \big(C^z_{\frac{2\pi}{3}}\big)^{\mathrm{T}} \qquad\qquad \mathbf{J}_{12} = \big(C^z_{\frac{2\pi}{3}}\big)^{\mathrm{T}} \mathbf{J}_{31} C^z_{\frac{2\pi}{3}} \tag{B.7}
$$

$$
\mathbf{K}_1 = C^z_{\frac{2\pi}{3}} \mathbf{K}_2 \big(C^z_{\frac{2\pi}{3}}\big)^{\mathrm{T}} \qquad\qquad \mathbf{K}_3 = \big(C^z_{\frac{2\pi}{3}}\big)^{\mathrm{T}} \mathbf{K}_2 C^z_{\frac{2\pi}{3}} \tag{B.8}
$$

The complete list of the coupling and anisotropy matrices:

$$
\mathbf{J}_{31} = \begin{pmatrix} J - \frac{1}{2}S^{zz} - S^{\varphi\varphi} & D^z & -D^y \\ -D^z & J - \frac{1}{2}S^{zz} + S^{\varphi\varphi} & S^{yz} \\ D^y & S^{yz} & J + S^{zz} \end{pmatrix}, \tag{B.9}
$$

$$\mathbf{J}_{23} = \begin{pmatrix} J - \frac{1}{2}S^{zz} + \frac{1}{2}S^{\varphi\varphi} & D^z + \frac{\sqrt{3}}{2}S^{\varphi\varphi} & \frac{1}{2}D^y - \frac{\sqrt{3}}{2}S^{yz} \\ -D^z + \frac{\sqrt{3}}{2}S^{\varphi\varphi} & J - \frac{1}{2}S^{zz} - \frac{1}{2}S^{\varphi\varphi} & -\frac{\sqrt{3}}{2}D^y - \frac{1}{2}S^{yz} \\ -\frac{1}{2}D^y - \frac{\sqrt{3}}{2}S^{yz} & \frac{\sqrt{3}}{2}D^y - \frac{1}{2}S^{yz} & J + S^{zz} \end{pmatrix}, \qquad \text{(B.10)}$$

$$\mathbf{J}_{12} = \begin{pmatrix} J - \frac{1}{2}S^{zz} + \frac{1}{2}S^{\varphi\varphi} & D^z - \frac{\sqrt{3}}{2}S^{\varphi\varphi} & \frac{1}{2}D^y + \frac{\sqrt{3}}{2}S^{yz} \\ -D^z - \frac{\sqrt{3}}{2}S^{\varphi\varphi} & J - \frac{1}{2}S^{zz} - \frac{1}{2}S^{\varphi\varphi} & \frac{\sqrt{3}}{2}D^y - \frac{1}{2}S^{yz} \\ -\frac{1}{2}D^y + \frac{\sqrt{3}}{2}S^{yz} & -\frac{\sqrt{3}}{2}D^y - \frac{1}{2}S^{yz} & J + S^{zz} \end{pmatrix}, \qquad \text{(B.11)}$$

$$\mathbf{K}_2 = \begin{pmatrix} -\frac{1}{2}K^{zz} - K^{\varphi\varphi} & 0 & 0 \\ 0 & -\frac{1}{2}K^{zz} + K^{\varphi\varphi} & K^{yz} \\ 0 & K^{yz} & K^{zz} \end{pmatrix}, \qquad \text{(B.12)}$$

$$\mathbf{K}_1 = \begin{pmatrix} -\frac{1}{2}K^{zz} + \frac{1}{2}K^{\varphi\varphi} & \frac{\sqrt{3}}{2}K^{\varphi\varphi} & -\frac{\sqrt{3}}{2}K^{yz} \\ \frac{\sqrt{3}}{2}K^{\varphi\varphi} & -\frac{1}{2}K^{zz} - \frac{1}{2}K^{\varphi\varphi} & -\frac{1}{2}K^{yz} \\ -\frac{\sqrt{3}}{2}K^{yz} & -\frac{1}{2}K^{yz} & K^{zz} \end{pmatrix}, \qquad \text{(B.13)}$$

$$\mathbf{K}_3 = \begin{pmatrix} -\frac{1}{2}K^{zz} + \frac{1}{2}K^{\varphi\varphi} & -\frac{\sqrt{3}}{2}K^{\varphi\varphi} & \frac{\sqrt{3}}{2}K^{yz} \\ -\frac{\sqrt{3}}{2}K^{\varphi\varphi} & -\frac{1}{2}K^{zz} - \frac{1}{2}K^{\varphi\varphi} & -\frac{1}{2}K^{yz} \\ \frac{\sqrt{3}}{2}K^{yz} & -\frac{1}{2}K^{yz} & K^{zz} \end{pmatrix}. \qquad \text{(B.14)}$$

We need the energy of rigidly rotated positive and negative chirality spin configurations. The two starting configurations are:

$$\boldsymbol{\sigma}_1^+ = \begin{pmatrix} \frac{\sqrt{3}}{2} \\ -\frac{1}{2} \\ 0 \end{pmatrix} \qquad \boldsymbol{\sigma}_2^+ = \begin{pmatrix} 0 \\ 1 \\ 0 \end{pmatrix} \qquad \boldsymbol{\sigma}_3^+ = \begin{pmatrix} -\frac{\sqrt{3}}{2} \\ -\frac{1}{2} \\ 0 \end{pmatrix} \qquad \text{and} \qquad \text{(B.15)}$$

$$\boldsymbol{\sigma}_1^- = \begin{pmatrix} -\frac{\sqrt{3}}{2} \\ -\frac{1}{2} \\ 0 \end{pmatrix} \qquad \boldsymbol{\sigma}_2^- = \begin{pmatrix} 0 \\ 1 \\ 0 \end{pmatrix} \qquad \boldsymbol{\sigma}_3^- = \begin{pmatrix} \frac{\sqrt{3}}{2} \\ -\frac{1}{2} \\ 0 \end{pmatrix} \qquad \text{(B.16)}$$

where the '+' and the '−' superscripts refer to $\kappa^z = +1$ and $\kappa^z = -1$ chirality of the configurations, respectively. For the definition of $\boldsymbol{\kappa}$ see eq. (1.5) in the Introduction. The matrices of rotations about the y and the z axis are:

$$R_y(\vartheta) = \begin{pmatrix} \cos(\vartheta) & 0 & \sin(\vartheta) \\ 0 & 1 & 0 \\ -\sin(\vartheta) & 0 & \cos(\vartheta) \end{pmatrix}, \qquad R_z(\varphi) = \begin{pmatrix} \cos(\varphi) & -\sin(\varphi) & 0 \\ \sin(\varphi) & \cos(\varphi) & 0 \\ 0 & 0 & 1 \end{pmatrix}. \qquad \text{(B.17)}$$

The *rotational energy* used in the main text is defined in terms of the Heisenberg model by:

$$E_y^\pm(\vartheta) = \sum_{ij=12,23,31} \left(R_y(\vartheta)\boldsymbol{\sigma}_i^\pm \right)^{\mathrm{T}} \mathbf{J}_{ij} \left(R_y(\vartheta)\boldsymbol{\sigma}_j^\pm \right) + \sum_{i=1,2,3} \left(R_y(\vartheta)\boldsymbol{\sigma}_i^\pm \right)^{\mathrm{T}} \mathbf{K}_i \left(R_y(\vartheta)\boldsymbol{\sigma}_i^\pm \right),$$

$$\text{(B.18)}$$

$$E_z^\pm(\varphi) = \sum_{ij=12,23,31} \left(R_z(\varphi)\boldsymbol{\sigma}_i^\pm \right)^{\mathrm{T}} \mathbf{J}_{ij} \left(R_z(\varphi)\boldsymbol{\sigma}_j^\pm \right) + \sum_{i=1,2,3} \left(R_z(\varphi)\boldsymbol{\sigma}_i^\pm \right)^{\mathrm{T}} \mathbf{K}_i \left(R_z(\varphi)\boldsymbol{\sigma}_i^\pm \right).$$

$$\text{(B.19)}$$

Substituting (B.9)–(B.17) into (B.18) and (B.19) and performing the operatios one gets the following formulas for the rotational energies:

$$E_z^+(\varphi) = -\frac{3}{2}J + \frac{3}{4}(S^{zz} - 2K^{zz}) + \frac{3\sqrt{3}}{2}D^z, \tag{B.20}$$

$$E_z^-(\varphi) = -\frac{3}{2}J + \frac{3}{4}(S^{zz} - 2K^{zz}) - \frac{3\sqrt{3}}{2}D^z + 3(S^{\varphi\varphi} + K^{\varphi\varphi})\cos(2\varphi), \tag{B.21}$$

$$E_y^\pm(\vartheta) = -\frac{3}{2}J + \frac{3}{16}(S^{zz} - 2K^{zz}) + \frac{3}{4}(S^{\varphi\varphi} + K^{\varphi\varphi})$$
$$\pm \left[\frac{3\sqrt{3}}{2}D^z - \frac{3}{2}(S^{\varphi\varphi} + K^{\varphi\varphi})\right]\cos(\vartheta)$$
$$+ \left[\frac{3}{8}(S^{\varphi\varphi} + K^{\varphi\varphi}) + \frac{9}{16}(S^{zz} - 2K^{zz})\right]\cos(2\vartheta). \tag{B.22}$$

Note, that the chirality vector rotates simultaneously with the spin directions, therefore during the rotation about the y axis at the point of $\vartheta = \pi$ κ^z is of opposite sign than in the starting configuration. The rotation about the z axis does not alter the chirality.

Three sub-lattice monolayer

In this chapter the spin model of a 2 dimensional triangular lattice will be derived. The coupling matrices and the on-site anisotropy matrices corresponding to the symmetry of the system and the resulting rotational energy functions will be given. The investigations will be restricted to magnetic states with 3 atoms per magnetic unit cell (3-sublattice magnetic structures), for an example see fig. B.2. Note, that description of different spin structures requires different size magnetic unit cell in the spin models.

The atomic positions of the 3-sublattice structure is given by the $\mathbf{R}_i + \mathbf{r}_p$ vectors where $\mathbf{R}_i$ gives the origin of the i-th magnetic unit cell and $\mathbf{r}_p$ $(p = 1, 2, 3)$ is the atomic position interpreted inside the magnetic unit cell. The magnetization directions, $\boldsymbol{\sigma}_{pi}$, and the interaction matrices, $\mathbf{J}_{pi,qj}$ and $\mathbf{K}_{pi}$, therefore have composite (unit cell plus sub-lattice) indices. The Heisenberg model for the monolayer reads:

$$\mathcal{H} = \sum_{\langle pi,qj\rangle} \boldsymbol{\sigma}_{pi}^{\mathrm{T}}\mathbf{J}_{pi,qj}\boldsymbol{\sigma}_{qj} + \sum_{p,i} \boldsymbol{\sigma}_{pi}^{\mathrm{T}}\mathbf{K}_{pi}\boldsymbol{\sigma}_{pi}, \tag{B.23}$$

where the first summation runs over the interacting spin pairs, $\mathbf{J}_{pi,qj}$ are the generalized exchange interaction matrices between the atoms at $\mathbf{R}_i + \mathbf{r}_p$ and $\mathbf{R}_j + \mathbf{r}_q$ positions and $\mathbf{K}_{pi}$ is the on-site anisotropy matrix at the $\mathbf{R}_i + \mathbf{r}_p$ site.

Assuming only 3-sublattice structures the degrees of freedom of the monolayer spin model is the directions of the magnetization at each sublattices thus $\boldsymbol{\sigma}_{pi} = \boldsymbol{\sigma}_p$. The on-site anisotropy matrix must be uniform at every site of the monolayer, i.e., $\mathbf{K}_{pi} = \mathbf{K}$. Taking these into
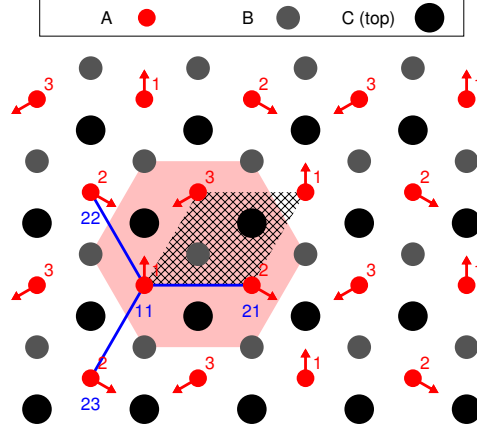
Figure B.2   Three atoms per magnetic unit cell spin structure: the Néel state of the fcc stacked monolayer. 'A' denotes the magnetic layer and 'C' and 'B' denote the first and the second layer of the supporter in the ABCABC**A** stacking. The directions of the magnetizations are drawn by red arrows and the sublattice indices ('1', '2', '3') of the atoms are written in red. The magnetic unit cell of the structure (red hexagon) contains 3 atoms while the chemical unit cell (shaded rhomb) contains only one. In the text the interaction of the 1$^{\text{st}}$ atom of the 1$^{\text{st}}$ sub-lattice (blue '11' label) and the first three atoms of the 2$^{\text{nd}}$ sublattice (blue '21', '22' and '23' labels) is analyzed.

account and rearranging the summations in eq. (B.23):

$$\mathcal{H} = \sum_{pq=12,23,31} \boldsymbol{\sigma}_p^{\text{T}} \left(\sum_{ij} \mathbf{J}_{pi,qj} \right) \boldsymbol{\sigma}_q + \sum_{p=1,2,3} \boldsymbol{\sigma}_p^{\text{T}} \left(\frac{1}{2} \sum_{i \neq j} \mathbf{J}_{pi,pj} \right) \boldsymbol{\sigma}_p + \sum_{\substack{p=1,2,3 \\ i}} \boldsymbol{\sigma}_p^{\text{T}} \mathbf{K} \boldsymbol{\sigma}_p. \tag{B.24}$$

Using the fact that the system exhibits discrete translational invariance by the $\mathbf{R}_i$ magnetic lattice vectors, the $\mathbf{J}_{p,i,q,j} = \mathbf{J}_{p,0,q,(j-i)}$ identity is obvious. The sublattice–sublattice exchange interaction matrices are introduced as:

$$\mathbf{J}_{pq} = \begin{cases} \sum_j \mathbf{J}_{p0,qj} & \text{if } p \neq q, \\ \frac{1}{2} \sum_{j \neq 0} \mathbf{J}_{p0,pj} & \text{if } p = q. \end{cases} \tag{B.25}$$

Substituting this quantity into eq. (B.24) every term is independent of i and the summation over i simplifies into a multiplication by the number of atoms in one sublattice, N, i.e., the number of magnetic unit cells. The energy per magnetic unit cell is then:

$$\frac{\mathcal{H}}{N} = \sum_{pq=12,23,31} \boldsymbol{\sigma}_p^{\text{T}} \mathbf{J}_{pq} \boldsymbol{\sigma}_q + \sum_{p=1,2,3} \boldsymbol{\sigma}_p^{\text{T}} \left(\mathbf{J}_{pp} + \mathbf{K} \right) \boldsymbol{\sigma}_p. \tag{B.26}$$

Since the environment of a particular atom exhibits C_{3v} symmetry only uniaxial on-site anisotropy is allowed up to second order. One complete sublattice also exhibits the C_{3v} symmetry so the $\mathbf{J}_{pp}$ intra-sublattice coupling matrices have the same symmetry properties as the

on-site anisotropy matrix, $\mathbf{K}$, and are independent of p because the sublattices are equivalent. These two uniaxial, one-sublattice energy contributions are incorporated into one term in the spin model:

$$\mathbf{J}_{pp} + \mathbf{K} = \begin{pmatrix} -\frac{1}{2}K^{zz} & 0 & 0 \\ 0 & -\frac{1}{2}K^{zz} & 0 \\ 0 & 0 & K^{zz} \end{pmatrix}. \qquad (p = 1, 2, 3) \qquad (\text{B.27})$$

Confronting with the parameters of the spin model of the trimer [eqs. (B.12)–(B.14)] this can be interpreted as the following extra requirements:

$$K^{yz} = 0 \qquad \text{and} \qquad K^{\varphi\varphi} = 0. \qquad (\text{B.28})$$

C_{3v} symmetry with the C_3 axis in the center of an elementary triangle takes the 3 sub-lattices into each other in the same way as it takes atoms into each other in the case of the trimer. Therefore the inter-sublattice coupling matrices have at least the same symmetry properties as the atom–atom coupling matrices in the case of the trimers. [Eqs. (B.9)–(B.11).] The monolayer possesses extra symmetry compared to the trimer: C_{3v} symmetry with the C_3 axis intersecting a chromium atom. The latter symmetry operations takes every sub-lattice into itself but transforms the exchange interaction matrices. The effect is presented by the transformation of the 1$^{\text{st}}$ atom of the 1$^{\text{st}}$ sub-lattice and the first three atoms of the 2$^{\text{nd}}$ sublattice, see the blue bonds in fig. B.2:

$$\boldsymbol{\sigma}_1^{\text{T}}(\mathbf{J}_{11,21} + \mathbf{J}_{11,22} + \mathbf{J}_{11,23})\boldsymbol{\sigma}_2$$
$$= \left(C_{\frac{2\pi}{3}}^z \boldsymbol{\sigma}_1\right)^{\text{T}}(\mathbf{J}_{11,21} + \mathbf{J}_{11,22} + \mathbf{J}_{11,23})\left(C_{\frac{2\pi}{3}}^z \boldsymbol{\sigma}_2\right)$$
$$= \boldsymbol{\sigma}_1^{\text{T}}\left[\left(C_{\frac{2\pi}{3}}^z\right)^{\text{T}}(\mathbf{J}_{11,21} + \mathbf{J}_{11,22} + \mathbf{J}_{11,23})C_{\frac{2\pi}{3}}^z\right]\boldsymbol{\sigma}_2. \qquad (\text{B.29})$$

The matrix of the $C_{\frac{2\pi}{3}}^z$ transformation is given in eq. (B.4). The above equation holds for any value of $\boldsymbol{\sigma}_1$ and $\boldsymbol{\sigma}_2$ so the sum of the exchange coupling matrices must be invariant under the $C_{\frac{2\pi}{3}}^z$ transformation. By writing down this conception for the complete sub-lattice one gets the following requirements for the inter-sub-lattice couplings:

$$\mathbf{J}_{pq} = \left(C_{\frac{2\pi}{3}}^z\right)^{\text{T}}\mathbf{J}_{pq}C_{\frac{2\pi}{3}}^z = C_{\frac{2\pi}{3}}^z\mathbf{J}_{pq}\left(C_{\frac{2\pi}{3}}^z\right)^{\text{T}} \qquad (pq = 12, 23, 31) \qquad (\text{B.30})$$

which implies

$$S^{yz} = 0, \qquad S^{\varphi\varphi} = 0, \qquad D^y = 0. \qquad (\text{B.31})$$

Finally, I give the form of the inter-sublattice exchange matrices:

$$\mathbf{J}_{pq} = \begin{pmatrix} J - \frac{1}{2}S^{zz} & D^z & 0 \\ -D^z & J - \frac{1}{2}S^{zz} & 0 \\ 0 & 0 & J + S^{zz} \end{pmatrix}. \qquad (pq = 12, 23, 31) \qquad (\text{B.32})$$

The rotational energy of the layer Néel structure is the same as that of the trimers [eqs. (B.20)–(B.22)] with taking into account the (B.28) and the (B.31) restrictions:

$$E_z^{\pm}(\varphi) = -\frac{3}{2}J + \frac{3}{4}(S^{zz} - 2K^{zz}) \ \pm \frac{3\sqrt{3}}{2}D^z, \tag{B.33}$$

$$E_y^{\pm}(\vartheta) = -\frac{3}{2}J + \frac{3}{16}(S^{zz} - 2K^{zz}) \pm \frac{3\sqrt{3}}{2}D^z \cos(\vartheta) + \frac{9}{16}(S^{zz} - 2K^{zz})\cos(2\vartheta). \tag{B.34}$$

Note that because of the non-vanishing z component of the DM vector the energy of the layer Néel structures with opposite chiralities are different.

Bibliography

[1] Marchon, B. & Olson, T. Magnetic spacing trends: From LMR to PMR and beyond. *IEEE Transactions on Magnetics* **45**, 3608–3611 (2009). DOI: 10.1109/TMAG.2009.2023624. Cited: page 1.

[2] Seagate Reaches 1 Terabit Per Square Inch Milestone In Hard Drive Storage With New Technology Demonstration. http://www.seagate.com/gb/en/newsroom/press-releases/terabit-milestone-storage-seagate-master-pr/ (2012). Cited: page 1.

[3] Everspin debuts first Spin-Torque MRAM for high performance storage systems. http://www.everspin.com/PDF/ST-MRAM_Press_Release.pdf (2012). Cited: page 1.

[4] Spin-Torque MRAM Technical Brief. http://www.everspin.com/PDF/ST-MRAM_Technical_Brief.pdf (2013). Cited: page 1.

[5] Wiesendanger, R. Spin mapping at the nanoscale and atomic scale. *Rev. Mod. Phys.* **81**, 1495–1550 (2009). DOI: 10.1103/RevModPhys.81.1495. Cited: page 1.

[6] Khajetoorians, A. A. & Wiebe, J. Hitting the limit of magnetic anisotropy. *Science* **344**, 976–977 (2014). DOI: 10.1126/science.1254402. Cited: pages 2, 9.

[7] Oka, H., Brovko, O. O., Corbetta, M., Stepanyuk, V. S., Sander, D. & Kirschner, J. Spin-polarized quantum confinement in nanostructures: Scanning tunneling microscopy. *Rev. Mod. Phys.* **86**, 1127–1168 (2014). DOI: 10.1103/RevModPhys.86.1127. Cited: page 2.

[8] Nowak, U. *Classical Spin Models* (John Wiley & Sons Ltd., Chichester, 2007). URN: urn:nbn:de:bsz:352-opus-92390. Cited: pages 2, 28.

[9] Dzyaloshinsky, I. A thermodynamic theory of "weak" ferromagnetism of antiferromagnetics. *Journal of Physics and Chemistry of Solids* **4**, 241–255 (1958). DOI: 10.1016/0022-3697(58)90076-3. Cited: page 3.

[10] Moriya, T. New Mechanism of Anisotropic Superexchange Interaction. *Phys. Rev. Lett.* **4**, 228–230 (1960). DOI: 10.1103/PhysRevLett.4.228. Cited: page 3.

[11] Moriya, T. Anisotropic Superexchange Interaction and Weak Ferromagnetism. *Phys. Rev.* **120**, 91–98 (1960). DOI: 10.1103/PhysRev.120.91. Cited: page 3.

[12] Bruno, P. Tight-binding approach to the orbital magnetic moment and magnetocrystalline anisotropy of transition-metal monolayers. *Phys. Rev. B* **39**, 865–868 (1989). DOI: 10.1103/PhysRevB.39.865. Cited: pages 3, 11, 40, 44.

[13] Bode, M., Heide, M., von Bergmann, K., Ferriani, P., Heinze, S., Bihlmayer, G., Kubetzka, A., Pietzsch, O., Blügel, S. & Wiesendanger, R. Chiral magnetic order at surfaces driven by inversion asymmetry. *Nature* **447**, 190–193 (2007). DOI: 10.1038/nature05802. Cited: pages 3, 4, 8.

[14] Yoneya, M., Kuboki, K. & Hayashi, M. Domain-wall structure of a classical Heisenberg ferromagnet on a Möbius strip. *Phys. Rev. B* **78**, 064419 (2008). DOI: 10.1103/PhysRevB.78.064419. Cited: page 4.

[15] Antal, A., Lazarovits, B., Udvardi, L., Szunyogh, L., Újfalussy, B. & Weinberger, P. First-principles calculations of spin interactions and the magnetic ground states of Cr trimers on Au(111). *Phys. Rev. B* **77**, 174429 (2008). DOI: 10.1103/PhysRevB.77.174429. Cited: pages 4, 9, 11, 12, 31, 44, 48, 49, 51, 55.

[16] Krüger, P., Taguchi, M. & Meza-Aguilar, S. Magnetism of $3d$ transition-metal monolayers on Cu(111) and Ag(111). *Phys. Rev. B* **61**, 15277–15283 (2000). DOI: 10.1103/PhysRevB.61.15277. Cited: page 4.

[17] Kurz, Ph., Bihlmayer, G., Hirai, K. & Blügel, S. Three-Dimensional Spin Structure on a Two-Dimensional Lattice: Mn/Cu(111). *Phys. Rev. Lett.* **86**, 1106–1109 (2001). DOI: 10.1103/PhysRevLett.86.1106. Cited: pages 4, 9.

[18] Jamneala, T., Madhavan, V. & Crommie, M. Kondo Response of a Single Antiferromagnetic Chromium Trimer. *Phys. Rev. Lett.* **87**, 256804 (2001). DOI: 10.1103/PhysRevLett.87.256804. Cited: page 7.

[19] Heinrich, A. J., Gupta, J. A., Lutz, C. P. & Eigler, D. M. Single-Atom Spin-Flip Spectroscopy. *Science* **306**, 466–469 (2004). DOI: 10.1126/science.1101077. Cited: page 7.

[20] Wahl, P., Simon, P., Diekhöner, L., Stepanyuk, V. S., Bruno, P., Schneider, M. A. & Kern, K. Exchange Interaction between Single Magnetic Adatoms. *Phys. Rev. Lett.* **98**, 056601 (2007). DOI: 10.1103/PhysRevLett.98.056601. Cited: page 7.

[21] Néel, N., Kröger, J., Limot, L., Palotás, K., Hofer, W. A. & Berndt, R. Conductance and Kondo Effect in a Controlled Single-Atom Contact. *Phys. Rev. Lett.* **98**, 016801 (2007). DOI: 10.1103/PhysRevLett.98.016801. Cited: page 7.

[22] Calvo, M. R., Fernández-Rossier, J., Palacios, J. J., Jacob, D., Natelson, D. & Untiedt, C. The Kondo effect in ferromagnetic atomic contacts. *Nature (London)* **458**, 1150–1153 (2009). DOI: 10.1038/nature07878. Cited: page 7.

[23] Chopra, H. D. & Hua, S. Z. Ballistic magnetoresistance over 3000% in Ni nanocontacts at room temperature. *Phys. Rev. B* **66**, 020403 (2002). DOI: 10.1103/PhysRevB.66.020403. Cited: page 7.

[24] Viret, M., Berger, S., Gabureac, M., Ott, F., Olligs, D., Petej, I., Gregg, J. F., Fermon, C., Francinet, G. & Goff, G. L. Magnetoresistance through a single nickel atom. *Phys. Rev. B* **66**, 220401 (2002). DOI: 10.1103/PhysRevB.66.220401. Cited: page 7.

[25] Viret, M., Gabureac, M., Ott, F., Fermon, C., Barreteau, C., Autes, G. & Guirado-Lopez, R. Giant anisotropic magneto-resistance in ferromagnetic atomic contacts. *Eur. Phys. J. B* **51**, 1–4 (2006). DOI: 10.1140/epjb/e2006-00201-3. Cited: page 7.

[26] Autès, G., Barreteau, C., Desjonquères, M. C., Spanjaard, D. & Viret, M. Giant orbital moments are responsible for the anisotropic magnetoresistance of atomic contacts. *Europhysics Letters* **83**, 17010 (2008). DOI: 10.1209/0295-5075/83/17010. Cited: pages 7, 34, 38, 39.

[27] Pasupathy, A. N., Bialczak, R. C., Martinek, J., Grose, J. E., Donev, L. A. K., McEuen, P. L. & Ralph, D. C. The Kondo Effect in the Presence of Ferromagnetism. *Science* **306**, 86–89 (2004). DOI: 10.1126/science.1102068. Cited: page 7.

[28] Bloch, F. Zur Theorie des Austauschproblems und der Remanenzerscheinung der Ferromagnetika. *Z. Phys. A* **74**, 295–335 (1932). DOI: 10.1007/BF01337791.
Cited: page 8.

[29] Heide, M. *Magnetic domain walls in ultrathin films: Contribution of the Dzyaloshinsky-Moriya interaction*. Ph.D. thesis, Rheinisch-Westfälische Technische Hochschule Aachen (2006).
Cited: page 8.

[30] Heide, M., Bihlmayer, G. & Blügel, S. Dzyaloshinskii-Moriya interaction accounting for the orientation of magnetic domains in ultrathin films: Fe/W(110). *Phys. Rev. B* **78**, 140403 (2008). DOI: 10.1103/PhysRevB.78.140403. Cited: page 8.

[31] Bruno, P. Geometrically Constrained Magnetic Wall. *Phys. Rev. Lett.* **83**, 2425–2428 (1999). DOI: 10.1103/PhysRevLett.83.2425. Cited: pages 8, 34.

[32] Kazantseva, N., Wieser, R. & Nowak, U. Transition to Linear Domain Walls in Nanoconstrictions. *Phys. Rev. Lett.* **94**, 037206 (2005). DOI: 10.1103/PhysRevLett.94.037206.
Cited: page 8.

[33] Pietzsch, O., Okatov, S., Kubetzka, A., Bode, M., Heinze, S., Lichtenstein, A. & Wiesendanger, R. Spin-Resolved Electronic Structure of Nanoscale Cobalt Islands on Cu(111). *Phys. Rev. Lett.* **96**, 237203 (2006). DOI: 10.1103/PhysRevLett.96.237203. Cited: page 8.

[34] Gao, C. L., Wulfhekel, W. & Kirschner, J. Revealing the 120° Antiferromagnetic Néel Structure in Real Space: One Monolayer Mn on Ag(111). *Phys. Rev. Lett.* **101**, 267205 (2008). DOI: 10.1103/PhysRevLett.101.267205. Cited: pages 8, 9, 47, 48, 52.

[35] Waśniowska, M., Schröder, S., Ferriani, P. & Heinze, S. Real space observation of spin frustration in Cr on a triangular lattice. *Phys. Rev. B* **82**, 012402 (2010). DOI: 10.1103/PhysRevB.82.012402. Cited: page 8.

[36] Palotás, K., Hofer, W. A. & Szunyogh, L. Simulation of spin-polarized scanning tunneling microscopy on complex magnetic surfaces: Case of a Cr monolayer on Ag(111). *Phys. Rev. B* **84**, 174428 (2011). DOI: 10.1103/PhysRevB.84.174428. Cited: page 8.

[37] Uzdin, S., Uzdin, V. & Demangeat, C. Magnetic trimer on non-magnetic substrate: From frustration towards non-collinearity. *Europhysics Letters* **47**, 556 (1999). DOI: 10.1209/epl/i1999-00425-9. Cited: page 8.

[38] Gotsis, H. J., Kioussis, N. & Papaconstantopoulos, D. A. Evolution of magnetism of Cr nanoclusters on Au(111): First-principles electronic structure calculations. *Phys. Rev. B* **73**, 014436 (2006). DOI: 10.1103/PhysRevB.73.014436. Cited: pages 8, 12, 48.

[39] Bergman, A., Nordström, L., Klautau, A. B., Frota-Pessôa, S. & Eriksson, O. A first-principles study of the magnetism and electronic structure of Cr clusters supported on a Au(111) surface. *Journal of Physics: Condensed Matter* **19**, 156226 (2007). DOI: 10.1088/0953-8984/19/15/156226. Cited: pages 8, 9, 12, 48.

[40] Újfalussy, B., Wang, X.-D., Nicholson, D. M. C., Shelton, W. A., Stocks, G. M., Wang, Y. & Gyorffy, B. L. Constrained density functional theory for first principles spin dynamics. *Journal of Applied Physics* **85**, 4824–4826 (1999). DOI: 10.1063/1.370494. Cited: page 9.

[41] Antropov, V. P., Katsnelson, M. I., van Schilfgaarde, M. & Harmon, B. N. *Ab Initio* Spin Dynamics in Magnets. *Phys. Rev. Lett.* **75**, 729–732 (1995). DOI: 10.1103/PhysRevLett.75.729. Cited: page 9.

[42] Stocks, G. M., Eisenbach, M., Újfalussy, B., Lazarovits, B., Szunyogh, L. & Weinberger, P. On calculating the magnetic state of nanostructures. *Progress in Materials Science* **52**, 371–387 (2007). DOI: 10.1016/j.pmatsci.2006.10.015. Cited: pages 9, 12, 48, 52.

[43] Miyashita, S. & Shiba, H. Nature of the Phase Transition of the Two-Dimensional Antiferromagnetic Plane Rotator Model on the Triangular Lattice. *Journal of the Physical Society of Japan* **53**, 1145–1154 (1984). DOI: 10.1143/JPSJ.53.1145. Cited: page 9.

[44] Georgeot, B. & Mila, F. Chirality of Triangular Antiferromagnetic Clusters as a Qubit. *Phys. Rev. Lett.* **104**, 200502 (2010). DOI: 10.1103/PhysRevLett.104.200502. Cited: page 9.

[45] Gambardella, P., Rusponi, S., Veronese, M., Dhesi, S. S., Grazioli, C., Dallmeyer, A., Cabria, I., Zeller, R., Dederichs, P. H., Kern, K., Carbone, C. & Brune, H. Giant magnetic anisotropy of single cobalt atoms and nanoparticles. *Science* **300**, 1130–1133 (2003). DOI: 10.1126/science.1082857. Cited: pages 9, 43.

[46] Ouazi, S., Vlaic, S., Rusponi, S., Moulas, G., Buluschek, P., Halleux, K., Bornemann, S., Mankovsky, S., Minár, J., Staunton, J. B., Ebert, H. & Brune, H. Atomic-scale engineering of magnetic anisotropy of nanostructures through interfaces and interlines. *Nature Communications* **3**, 1313 (2012). DOI: 10.1038/ncomms2316. Cited: page 9.

[47] Hohenberg, P. & Kohn, W. Inhomogeneous Electron Gas. *Phys. Rev.* **136**, B864–B871 (1964). DOI: 10.1103/PhysRev.136.B864. Cited: page 9.

[48] Kohn, W. & Sham, L. J. Self-Consistent Equations Including Exchange and Correlation Effects. *Phys. Rev.* **140**, A1133–A1138 (1965). DOI: 10.1103/PhysRev.140.A1133. Cited: page 9.

[49] Vignale, G. & Rasolt, M. Density-functional theory in strong magnetic fields. *Phys. Rev. Lett.* **59**, 2360–2363 (1987). DOI: 10.1103/PhysRevLett.59.2360. Cited: page 9.

[50] Vignale, G. & Rasolt, M. Erratum: Density-Functional Theory in Strong Magnetic Fields. *Phys. Rev. Lett.* **62**, 115–115 (1989). DOI: 10.1103/PhysRevLett.62.115. Cited: page 9.

[51] Vignale, G. & Rasolt, M. Current- and spin-density-functional theory for inhomogeneous electronic systems in strong magnetic fields. *Phys. Rev. B* **37**, 10685–10696 (1988). DOI: 10.1103/PhysRevB.37.10685. Cited: page 9.

[52] Vignale, G. & Rasolt, M. Erratum: Current- and spin-density-functional theory for inhomogeneous electronic systems in strong magnetic fields. *Phys. Rev. B* **39**, 5475–5475 (1989). DOI: 10.1103/PhysRevB.39.5475.2. Cited: page 9.

[53] Hobbs, D., Kresse, G. & Hafner, J. Fully unconstrained noncollinear magnetism within the projector augmented-wave method. *Phys. Rev. B* **62**, 11556–11570 (2000). DOI: 10.1103/PhysRevB.62.11556. Cited: page 9.

[54] Robles, R. & Nordström, L. Noncollinear magnetism of Cr clusters on Fe surfaces. *Phys. Rev. B* **74**, 094403 (2006). DOI: 10.1103/PhysRevB.74.094403. Cited: page 9.

[55] Bergman, A., Nordström, L., Burlamaqui Klautau, A., Frota-Pessôa, S. & Eriksson, O. Magnetic structures of small Fe, Mn, and Cr clusters supported on Cu(111): Noncollinear first-principles calculations. *Phys. Rev. B* **75**, 224425 (2007). DOI: 10.1103/PhysRevB.75.224425. Cited: page 9.

[56] Yavorsky, B. Y. & Mertig, I. Noncollinear interface magnetism and ballistic transport in Fe/FeO/MgO/Fe tunnel junctions: Ab initio calculations using the KKR method. *Phys. Rev. B* **74**, 174402 (2006). DOI: 10.1103/PhysRevB.74.174402. Cited: page 9.

[57] Minár, J., Bornemann, S., Šipr, O., Polesya, S. & Ebert, H. Magnetic properties of Co clusters deposited on Pt(111). *Applied Physics A* **82**, 139–144 (2006). DOI: 10.1007/s00339-005-3359-1. Cited: page 9.

[58] Újfalussy, B., Lazarovits, B., Szunyogh, L., Stocks, G. M. & Weinberger, P. *Ab initio* spin dynamics applied to nanoparticles: Canted magnetism of a finite Co chain along a Pt(111) surface step edge. *Phys. Rev. B* **70**, 100404 (2004). DOI: 10.1103/PhysRevB.70.100404. Cited: page 9.

[59] Lazarovits, B., Újfalussy, B., Szunyogh, L., Stocks, G. M. & Weinberger, P. *Ab initio* study of canted magnetism of finite atomic chains at surfaces. *Journal of Physics: Condensed Matter* **16**, S5833–S5840 (2004). DOI: 10.1088/0953-8984/16/48/058. Cited: page 9.

[60] Korringa, J. On the calculation of the energy of a Bloch wave in a metal. *Physica* **13**, 392–400 (1947). DOI: 10.1016/0031-8914(47)90013-X. Cited: pages 10, 11.

[61] Kohn, W. & Rostoker, N. Solution of the Schrödinger Equation in Periodic Lattices with an Application to Metallic Lithium. *Phys. Rev.* **94**, 1111–1120 (1954). DOI: 10.1103/PhysRev.94.1111. Cited: pages 10, 11.

[62] Palotás, K. *Ab initio theory of electric transport in nanostructures*. Ph.D. thesis, Technischen Universität Wien (2004). Cited: pages 10, 15.

[63] Faulkner, J. The modern theory of alloys. *Progress in Materials Science* **27**, 1–187 (1982). DOI: 10.1016/0079-6425(82)90005-6. Cited: page 10.

[64] Buruzs, A. *Temperature dependent magnetic properties of thin films and bulk ferromagnets: An implementation of the Disordered Local Moment Scheme*. Ph.D. thesis, Technischen Universität Wien (2008). Cited: pages 10, 15.

[65] Szunyogh, L., Újfalussy, B., Weinberger, P. & Kollár, J. Self-consistent localized KKR scheme for surfaces and interfaces. *Phys. Rev. B* **49**, 2721–2729 (1994). DOI: 10.1103/PhysRevB.49.2721. Cited: pages 10, 11, 23.

[66] Szunyogh, L., Újfalussy, B., Weinberger, P. & Kollár, J. The self-consistent fully relativistic SKKR Green function method: applications to the (100), (110) and (111) surfaces of Au and Pt. *Journal of Physics: Condensed Matter* **6**, 3301 (1994). DOI: 10.1088/0953-8984/6/18/006. Cited: pages 10, 11.

[67] Zeller, R., Dederichs, P. H., Újfalussy, B., Szunyogh, L. & Weinberger, P. Theory and convergence properties of the screened Korringa-Kohn-Rostoker method. *Phys. Rev. B* **52**, 8807–8812 (1995). DOI: 10.1103/PhysRevB.52.8807. Cited: pages 10, 11.

[68] Lazarovits, B., Szunyogh, L. & Weinberger, P. Fully relativistic calculation of magnetic properties of Fe, Co, and Ni adclusters on Ag(100). *Phys. Rev. B* **65**, 104441 (2002). DOI: 10.1103/PhysRevB.65.104441. Cited: pages 10, 11.

[69] Lazarovits, B. *Electronic and magnetic properties of nanostructures*. Ph.D. thesis, Technischen Universität Wien (2003). Cited: pages 10, 11, 15.

[70] Ebert, H., Ködderitzsch, D. & Minár, J. Calculating condensed matter properties using the KKR-Green's function method—recent developments and applications. *Reports on Progress in Physics* **74**, 096501 (2011). DOI: 10.1088/0034-4885/74/9/096501. Cited: page 10.

[71] Halilov, S. V., Eschrig, H., Perlov, A. Y. & Oppeneer, P. M. Adiabatic spin dynamics from spin-density-functional theory: Application to Fe, Co, and Ni. *Phys. Rev. B* **58**, 293–302 (1998). DOI: 10.1103/PhysRevB.58.293. Cited: page 10.

[72] Jansen, H. J. F. Magnetic anisotropy in density-functional theory. *Phys. Rev. B* **59**, 4699–4707 (1999). DOI: 10.1103/PhysRevB.59.4699. Cited: pages 10, 25, 29.

[73] Liechtenstein, A. I., Katsnelson, M. I., Antropov, V. P. & Gubanov, V. A. Local spin density functional approach to the theory of exchange interactions in ferromagnetic metals and alloys. *Journal of Magnetism and Magnetic Materials* **67**, 65–74 (1987). DOI: 10.1016/0304-8853(87)90721-9. Cited: pages 10, 11, 36.

[74] Udvardi, L., Szunyogh, L., Palotás, K. & Weinberger, P. First-principles relativistic study of spin waves in thin magnetic films. *Phys. Rev. B* **68**, 104436 (2003). DOI: 10.1103/PhysRevB.68.104436. Cited: pages 10, 11, 25, 26, 31.

[75] Szunyogh, L., Lazarovits, B., Udvardi, L., Jackson, J. & Nowak, U. Giant magnetic anisotropy of the bulk antiferromagnets IrMn and IrMn$_3$ from first principles. *Phys. Rev. B* **79**, 020403 (2009). DOI: 10.1103/PhysRevB.79.020403. Cited: pages 10, 11, 25, 51, 53.

[76] Szunyogh, L., Udvardi, L., Jackson, J., Nowak, U. & Chantrell, R. Atomistic spin model based on a spin-cluster expansion technique: Application to the IrMn$_3$/Co interface. *Phys. Rev. B* **83**, 024401 (2011). DOI: 10.1103/PhysRevB.83.024401. Cited: pages 10, 11, 25, 30, 53.

[77] Drautz, R. & Fähnle, M. Spin-cluster expansion: Parametrization of the general adiabatic magnetic energy surface with *ab initio* accuracy. *Phys. Rev. B* **69**, 104404 (2004). DOI: 10.1103/PhysRevB.69.104404. Cited: page 10.

[78] Drautz, R. & Fähnle, M. Parametrization of the magnetic energy at the atomic level. *Phys. Rev. B* **72**, 212405 (2005). DOI: 10.1103/PhysRevB.72.212405. Cited: page 10.

[79] Deak, A., Szunyogh, L. & Ujfalussy, B. Thickness-dependent magnetic structure of ultrathin Fe/Ir(001) films: From spin-spiral states toward ferromagnetic order. *Phys. Rev. B* **84**, 224413 (2011). DOI: 10.1103/PhysRevB.84.224413. Cited: pages 10, 44.

[80] Antal, A., Lazarovits, B., Balogh, L., Udvardi, L. & Szunyogh, L. Multiscale studies of complex magnetism of nanostructures based on first principles. *Philosophical Magazine* **88**, 2715–2724 (2008). DOI: 10.1080/14786430802389213. Cited: page 13.

[81] Balogh, L., Lebecki, K. M., Lazarovits, B., Udvardi, L., Szunyogh, L. & Nowak, U. Monte Carlo study on magnetic nanoparticles from first principle. *Journal of Physics: Conference Series* **200**, 072103 (2010). DOI: 10.1088/1742-6596/200/7/072103. Cited: page 13.

[82] Balogh, L., Palotás, K., Udvardi, L., Szunyogh, L. & Nowak, U. Theoretical study of magnetic domain walls through a cobalt nanocontact. *Phys. Rev. B* **86**, 024406 (2012). DOI: 10.1103/PhysRevB.86.024406. Cited: pages 13, 26.

[83] Balogh, L., Udvardi, L. & Szunyogh, L. Magnetic anisotropy and chirality of frustrated Cr nanostructures on Au(111). *Journal of Physics: Condensed Matter* **26**, 436001 (2014). DOI: 10.1088/0953-8984/26/43/436001. Cited: page 13.

[84] Zabloudil, J., Hammerling, R., Szunyogh, L. & Weinberger, P. *Electron Scattering in Solid Matter: A Theoretical and Computational Treatise*. Springer Series in Solid-State Sciences (Springer-Verlag, Berlin, 2005). Cited: pages 15, 25.

[85] Rose, M. E. *Relativistic Electron Theory* (Wiley, New York, 1961). Cited: page 15.

[86] Vosko, S. H., Wilk, L. & Nusair, M. Accurate spin-dependent electron liquid correlation energies for local spin density calculations: a critical analysis. *Canadian Journal of Physics* **58**, 1200–1211 (1980). DOI: 10.1139/p80-159. Cited: pages 16, 29.

[87] Ceperley, D. M. & Alder, B. J. Ground State of the Electron Gas by a Stochastic Method. *Phys. Rev. Lett.* **45**, 566–569 (1980). DOI: 10.1103/PhysRevLett.45.566. Cited: pages 16, 29.

[88] Perdew, J. P. & Zunger, A. Self-interaction correction to density-functional approximations for many-electron systems. *Phys. Rev. B* **23**, 5048–5079 (1981). DOI: 10.1103/PhysRevB.23.5048. Cited: pages 16, 29.

[89] Lloyd, P. Wave propagation through an assembly of spheres: II. The density of single-particle eigenstates. *Proceedings of the Physical Society* **90**, 207 (1967). DOI: 10.1088/0370-1328/90/1/323. Cited: pages 25, 40.

[90] Newman, M. E. J. & Barkema, G. T. *Monte Carlo Methods in Statistical Physics* (Oxford University Press Inc., New York, 1999). Cited: page 28.

[91] Metropolis, N., Rosenbluth, A. W., Rosenbluth, M. N., Teller, A. H. & Teller, E. Equation of State Calculations by Fast Computing Machines. *The Journal of Chemical Physics* **21**, 1087–1092 (1953). DOI: 10.1063/1.1699114. Cited: page 28.

[92] Jubert, P.-O., Allenspach, R. & Bischof, A. Magnetic domain walls in constrained geometries. *Phys. Rev. B* **69**, 220410 (2004). DOI: 10.1103/PhysRevB.69.220410. Cited: page 34.

[93] Pietzsch, O., Kubetzka, A., Bode, M. & Wiesendanger, R. Real-Space Observation of Dipolar Antiferromagnetism in Magnetic Nanowires by Spin-Polarized Scanning Tunneling Spectroscopy. *Phys. Rev. Lett.* **84**, 5212–5215 (2000). DOI: 10.1103/PhysRevLett.84.5212. Cited: page 34.

[94] Thiess, A., Mokrousov, Y. & Heinze, S. Competing magnetic anisotropies in atomic-scale junctions. *Phys. Rev. B* **81**, 054433 (2010). DOI: 10.1103/PhysRevB.81.054433. Cited: pages 34, 43.

[95] Šipr, O., Bornemann, S., Minár, J., Polesya, S., Popescu, V., Šimůnek, A. & Ebert, H. Magnetic moments, exchange coupling, and crossover temperatures of Co clusters on Pt(111) and Au(111). *Journal of Physics: Condensed Matter* **19**, 096203 (2007). DOI: 10.1088/0953-8984/19/9/096203. Cited: page 38.

[96] Błoński, P. & Hafner, J. Density-functional theory of the magnetic anisotropy of nanostructures: an assessment of different approximations. *Journal of Physics: Condensed Matter* **21**, 426001 (2009). DOI: 10.1088/0953-8984/21/42/426001. Cited: page 38.

[97] Lazarovits, B., Szunyogh, L. & Weinberger, P. Magnetic properties of finite Co chains on Pt(111). *Phys. Rev. B* **67**, 024415 (2003). DOI: 10.1103/PhysRevB.67.024415. Cited: page 38.

[98] Lüders, M., Ernst, A., Däne, M., Szotek, Z., Svane, A., Ködderitzsch, D., Hergert, W., Györffy, B. L. & Temmerman, W. M. Self-interaction correction in multiple scattering theory. *Phys. Rev. B* **71**, 205109 (2005). DOI: 10.1103/PhysRevB.71.205109. Cited: page 39.

[99] Kotliar, G., Savrasov, S. Y., Haule, K., Oudovenko, V. S., Parcollet, O. & Marianetti, C. A. Electronic structure calculations with dynamical mean-field theory. *Rev. Mod. Phys.* **78**, 865–951 (2006). DOI: 10.1103/RevModPhys.78.865. Cited: page 39.

[100] Etz, C., Zabloudil, J., Weinberger, P. & Vedmedenko, E. Y. Magnetic properties of single atoms of Fe and Co on Ir(111) and Pt(111). *Phys. Rev. B* **77**, 184425 (2008). DOI: 10.1103/PhysRevB.77.184425. Cited: page 43.

[101] Bornemann, S., Minár, J., Staunton, J. B., Honolka, J., Enders, A., Kern, K. & Ebert, H. Magnetic anisotropy of deposited transition metal clusters. *European Physical Journal D* **45**, 529–534 (2007). DOI: 10.1140/epjd/e2007-00190-9. Cited: page 43.

[102] Boča, R. *A Handbook of Magnetochemical Formulae* (Elsevier, London, 2012). Cited: page 44.

[103] Lounis, S. & Dederichs, P. H. Mapping the magnetic exchange interactions from first principles: Anisotropy anomaly and application to Fe, Ni, and Co. *Phys. Rev. B* **82**, 180404 (2010). DOI: 10.1103/PhysRevB.82.180404. Cited: page 44.

[104] Błoński, P. & Hafner, J. Magneto-structural properties and magnetic anisotropy of small transition-metal clusters: a first-principles study. *Journal of Physics: Condensed Matter* **23**, 136001 (2011). DOI: 10.1088/0953-8984/23/13/136001. Cited: page 55.